Aeroelastic Stability of a 2D Airfoil Section equipped with a Trailing Edge Flap

Bergami, Leonardo

Publication date:
2008

Document Version
Publisher's PDF, also known as Version of record

Risø DTU
National Laboratory
for Sustainable Energy

Risø-R-Report

Aeroservoelastic Stability of a 2D Airfoil Section equipped with a Trailing Edge Flap

Leonardo Bergami

Risø-R-1663(EN)

Risø National Laboratory for Sustainable Energy
Technical University of Denmark
Roskilde, Denmark
November 2008

Author: Leonardo Bergami
Title: Aeroservoelastic Stability of a 2D Airfoil Section equipped with a Trailing Edge Flap
Department: Wind Energy Division

Risø-R-1663(EN)
November 2008

Abstract (max. 2000 char.):

Recent studies conclude that important reduction of the fatigue loads encountered by a wind turbine blade can be achieved using a deformable trailing edge control system. The focus of the current work is to determine the effect of this flap-like system on the aeroelastic stability of a 2D airfoil section. A simulation tool is implemented to predict the flow speed at which a flap equipped section may become unstable, either due to flutter or divergence.

First, the stability limits of the airfoil without flap are determined, and, in the second part of the work, a deformable trailing edge flap is applied. Stability is investigated for the uncontrolled flap, and for three different control algorithms. The three controls are tuned for fatigue load alleviation and they are based on, respectively, measurement of the heave displacement and velocity, measurement of the local angle of attack, measurement of the pressure difference between the two sides of the airfoil. The stability of the aeroservoelastic system in a defined equilibrium state, and for a given flow speed, is then determined by solving an eigenvalue problem.

Results show that the trailing edge control system modifies significantly the stability limits of the section. In the investigated case, increased flutter limits are reported when the elastic flap is left without control, whereas, by applying any of the control algorithms, the flutter velocity is reduced. Nevertheless, only in the heave control case the flutter limit becomes critically close to normal operation flow speeds. Furthermore, a marked dependence of the stability limits on the control gain is also observed and, by tuning the gain parameters, flutter and divergence can be suppressed for flow speed even above the flutter velocity encountered with uncontrolled flap.

Keywords:

Aeroservoelastic Stability, Flutter and Divergence, Deformable Trailing Edge Flap, Active Control Flutter Suppression.

ISSN 0106-2840
ISBN 978-87-550-3711-3

Contract no.:

Group's own reg. no.:

Sponsorship:

Cover :

Pages: 109
Tables: 11
References: 26

Information Service Department
Risø National Laboratory for Sustainable Energy
Technical University of Denmark
P.O.Box 49
DK-4000 Roskilde
Denmark
Telephone +45 46774004
bibl@risoe.dk
Fax +45 46774013
www.risoe.dtu.dk

Contents

Notation

Roman Letter

$\boldsymbol{A}$	Coefficient matrix for linear terms. Eq.(2.27),(5.23)	
A_i	Indicial response constant, Eq.(2.21)	
A_y	Heave flap control, proportional term gain parameter	
B_y	Heave flap control, differential term gain parameter	
b_{hc}	airfoil half-chord length	m
b_i	Indicial response constant, Eq.(2.21)	
Cd	Static drag coefficient	–
Cl	Static lift coefficient	–
Cm	Static pitching moment coefficient	–
Cp	Static pressure difference coefficient	–
c_{dof}	Structural viscous damping, Section 2.1.3	$kg/(ms)$
D_{aed}	Drag force	N/m
$\underline{\boldsymbol{f}}$	Constant terms vector in matrix equations. Eq.(2.27),(5.23)	
GF_{aed}	Generalized forces acting on the flap. Eq.(5.7)	N/m
I_{ea}	Second moment of area, with respect to the Elastic Axis	kgm^2/m
Ims_{fl}	Flap inertial coupling term. Eq.(5.4)	kg/m
Ins_{fl}	Flap inertial coupling term. Eq.(5.3)	kg/m
L_{aed}	Lift Force	N/m
M_{aed}	Pitching Moment	Nm/m
$\boldsymbol{M}$	Coefficient matrix for first order terms. Eq.(2.27),(5.23)	
m_{tot}	Airfoil Section total mass per unit span	kg/m
m_{mod}	Flap modal mass in generalized coordinates. Eq.(5.6)	kgm/m
n_{lag}	Number of terms for indicial response approximation	
r_α	Dimensionless Radius of Gyration, Sect. 2.1.2	–
r_β	Dimensionless 2^{nd} moment of area for plain flap	–
S_α	Moment of static unbalance, Sect. 2.1.2	Nm/m
$t_{1/2}$	Control Time Lag, half reaction time	s
U_0	Free stream flow speed	m/s
U_F	Flow speed at which flutter occur	m/s
u_{fl}	Flap deflection, deformation mode shape	m

w	Equivalent downwash speed at the 3/4 chord	
X_α	Dimensionless Moment of static unbalance, Sect. 2.1.2	–
X_β	Dimensionless position of flap centre of gravity	–
$\underline{\boldsymbol{x}}$	Vector with system state variables. Eq.(2.26),(5.24)	
x	Streamwise (horizontal) coordinate, degree of freedom	m
y	Heave (vertical) coordinate, degree of freedom	m
z_i	Aerodynamic state variables for wake induced time lag	

Greek Letter

α	Pitch (torsion) rotation coordinate, dof; angle of attack	rad
α_{eff}	Equiv. effective (unsteady effects) angle of attack	rad
$\alpha_{3/4}$	Equiv. quasi-steady angle of attack at 3/4 chord. Eq.(2.24)	rad
$\alpha_{lift,0}$	Steady angle of attack corresponding to zero static lift	rad
β	Flap Deflection generalized coordinate.	–
ΔP	Pressure difference between suction and pressure sides	Pa
δ	Logarithmic damping ratio, structure and modes, Eq.(B.1)	–
ε	Chordwise dimensionless coordinate	–
$\varepsilon_{10\%}$	Point at 10% chord distance from the leading edge	–
ε_{cnst}	Point where static C_L/C_P is constant. App. C	–
λ	Complex eigenvalue	
ξ_{dof}	Structural Damping Ratio, Section 2.1.3	–
ρ^{2D}	Density along the chord, for unit span	kg/m^2
ρ	Fluid mass. For air: $\rho = 1.225\ kg/m^3$	kg/m^3
$\boldsymbol{\Phi}$	Matrix collecting the complex eigenvectors	
φ	Indicial function of lift	
$\underline{\boldsymbol{\phi}}$	Complex eigenvector, modal shape	
ω	Frequency, natural-uncoupled or modal.	rad/s

Subscripts

$0, sts$	Related to the steady state used to linearize the system
$circ$	Circulatory
cg	Centre of Gravity
$ctrl$	Output of the whole control system (eventually with time lag)
ea	Elastic Axis
eff	see α_{eff}
fl	Related to the flap structure, and flap deflection dof
hp	Flap 'hinge point', first point with $u_{fl} \neq 0$ (also as superscript)
le	Leading Edge
nc	Non circulatory
nl	Non linear formulation

set	Output of the ideal control algorithm (no time lag)
te	Trailing Edge
x	Related to Streamwise dof
y	Related to Heave dof
α	Related to Pitch-Torsion dof

Chapter 1

Introduction

An important issue in the design of modern wind turbine blades is the fatigue damage related to fluctuations in the aerodynamic forcing, produced, for instance, by wind turbulence, wind shear, tower shadow or yaw misalignment. Larsen [18] investigates the possibility of alleviating fatigue loads by modifying the 'traditional' blade pitching system, and he reaches to the conclusion that by adopting a cyclic blade pitching the flapwise fatigue loads can be reduced up to 15 % with respect to the normal collective pitch, and a reduction up to 28 % would be instead achieved by pitching each blade independently.

Pitching the whole blade, though, may become inadequate as wind turbine blades increase in size and become more flexible, further load reduction would hence require a faster control, able to intervene on the aerodynamic forces locally along the blade span. The aerodynamic forces can be then controlled by changing the geometry of the lifting surface, in this case by deforming parts of the blade airfoil section.

A control based on the same principle is successfully and elegantly 'applied' by some falcon birds, as the kestrel (Figure 1.1), when they are hovering during the hunt. This raptor is in fact able to maintain a still position in the wind stream, by continuously adapting the geometry of its lifting surfaces (wings and tail), so to compensate for turbulences in the incoming flow; changes of geometry in wings and tail are then realized through rapid movements of the feathers, which could be seen as fast controllers acting locally along the 'blade' span. Less 'rural' examples are also found in the aeronautic field: aileron and flaps are well known devices to modify the aerodynamic forces on a wing by changing the airfoil geometry (Figure 1.2).

A similar concept can be applied to control a wind turbine blade by deforming its trailing edge geometry (Figure 1.3). Investigations in this sense have been first carried out on a 2D airfoil section by Basualdo [6], using a panel method, and by Troldborg [24] with a CFD analysis. Troldborg also concludes that an optimal deformation shape should be non linear, giving

Figure 1.1: Variable airfoil geometry in nature: a kestrel is 'hovering'.

Figure 1.2: Variable airfoil geometry in aeronautics: flaps, aileron and deflectors on aircraft wing.

Figure 1.3: Variable airfoil geometry in wind turbine blade: deformable trailing edge geometry. The non linear deflection shape is obtained with piezoelectric laminae.

thus a smooth and continuous deflection of the aft part of the airfoil. The trailing edge flap that is actually investigated is hence different from a 'classic' rigid plain flap with a linear deformation shape, as found on aircrafts, and, instead of rotating around an hinge point, it deforms continuously, according to non linear deflection mode shapes (Figure 1.3).

The load reduction potential achievable with a deformable trailing edge control has been also assessed through simulations of a 2D airfoil section [8] and a full blade [4], using, in both cases, the unsteady aerodynamic model developed by Gaunaa [9] for thin airfoil and potential flow. Later investigations expand the model to take into account also the effects from fluid viscosity [2], as well as that, the interaction with a wind turbine standard control system has been also investigated [3]. In any case, simulations indicate that the load alleviation potential achievable with deformable trailing edge flaps is significant, and the more realistic model [3] reports a reduction in the blade flapwise fatigue loads up to 40 %.

The present study contributes to the investigation of the deformable trailing edge flap control by analysing its effect on the system stability. The focus is on how the relative flow speed, at which aeroelastic instabilities such as flutter and divergence occur, would be modified by the presence of the deformable elastic trailing edge and by the algorithms that control its deflection.

Flutter instabilities in wind turbine applications have been investigated by Lobitz [19], and he concludes that, for an isolated blade of a 1.5 MW turbine, flutter would occur at a rotor speed twice the nominal one. Similar results are also reported in Hansen's [14] stability analysis of the 5 MW NREL reference turbine, Hansen [14, 13] also concludes that similar flutter limits are predicted with full turbine and isolated blade analysis. The predicted flutter limits are hence sufficiently high and do not represent a constraint for current wind turbine blades. Flutter may indeed become problematic if, due to the flap control, the stability limit would lower and drift to flow speeds encountered in normal operation. It is thus important to predict the effects of the trailing edge control system on the stability limits.

The work presents a first simplified approach. Stability is, in fact, analysed through an aeroservoelastic investigation of a representative 2D airfoil section equipped with a trailing edge flap. A similar approach is also reported in the classic flutter studies from Theodorsen and Garrick [22], where stability limits are initially computed using a 2D wing section model, similar results are then obtained from subsequent wind tunnel experiments of full wing flutter.

The report is organized in two parts:
In the **first part**, stability analysis is carried out for an undeformable airfoil section, the flap is not considered and the problem reduces to a classic

aeroelastic stability investigation of a 2D section. Terms of comparison and validation are thus available, furthermore, it is also possible to rapidly investigate how the stability limits vary depending on the input parameters and on the approximations introduced in the model. The results obtained for the undeformable airfoil section also provide a useful term of comparison to later asses the effects of a flap control.

The aeroelastic system is represented through a structural model coupled with an aerodynamic one. The behaviour of the structure is described by a set of differential equations of motion, which represents the rigid motion of the airfoil suspended by linear spring and dampers. The aerodynamic forces acting on the airfoil are computed using an unsteady aerodynamic model [15], and inviscid fluid and fully attached flow are assumed. The complete set of aeroelastic equations is linearised with respect to an assigned steady state, and the stability of the system at the specified state is assessed using an eigenvalue approach. The original set of equations, prior to linearisation, is also solved with a time marching integration, and the resulting time histories are used to validate the stability results from the eigenvalue analysis.

In the **second part** the airfoil section is equipped with a trailing edge flap. As in the previous load reduction investigations, the flap consists in a smooth deformation of the airfoil aft part, described by a non linear deflection shape. The structural model includes an extra degree of freedom for the elastic flap deflection, which is modelled using a generalized coordinates approach applied to the assigned deformation shape. The aerodynamic part is based on Gaunaa's [9] potential flow model, which allows to determine forces and pressure distribution on a thin airfoil undergoing arbitrary motion and deformation. Stability is firstly investigated for the case of an uncontrolled elastic flap, and, afterwards, control models are applied. The control actuator is here represented as an extra elastic term in the flap equation of motion, and it responds to control algorithms based on measurements of the heave displacement and velocity, on the angle of attack and on the pressure difference between the two sides of the airfoil. Control time lag is also included in the model as a first order filter.

Similarly to the undeformable airfoil part, the full set of equations describing the aeroservoelastic system is analysed for stability using an eigenvalue approach. A time marching simulation is also carried out to verify the predicted stability limits.

A stability tool will be implemented to predict the relative flow speeds at which instabilities, as divergence and flutter, are expected to occur for an airfoil section actively controlled by a deformable trailing edge; the effects of the trailing edge control on the section stability will be thereby determined.

Part I

Undeformable airfoil

Chapter 2

Model and method

In this first part, aeroelastic stability is investigated for an airfoil section that is assumed to be undeformable. In other words, the control system and the trailing edge flap, which will be introduced in the second part, are not present here, and the airfoil section can only perform in plane rigid motions.

The assumption simplifies the investigation to a 'classic' aeroelastic stability problem, for which thorough descriptions and solutions can be found in literature [7, 22]. Terms of comparison are thus available to validate the model and its implementation. Furthermore, the undeformable airfoil also allows a rapid sensitivity analysis on the parameters affecting the stability limits. The analysis covers not only the influence of the numerical values assigned to the system characteristic parameters (mass, stiffness, damping, etc.); but also, investigations are carried out to determine in which extend different aspects and assumptions involved in the aeroelastic model may affect the results.

The aeroelastic system represents the behaviour of the airfoil section immersed in fluid, and is described through a structural model coupled with an aerodynamic one. Since the airfoil performs only in plane rigid motion, three degrees of freedom (dof) are sufficient to fully define the dynamic behaviour of the structure: 2 dof are used to describe rigid body translation and 1 for rotation.

The forces that originate from the interaction between the airfoil and the fluid are described by an unsteady aerodynamic model. The model assumes incompressible fluid and fully attached flow, and an approximation for the indicial function of lift is employed.

Stability analysis is carried out in the frequency domain by applying an eigenvalue approach. The results are then verified in the time domain by solving the system of aeroelastic equations with a time marching integration.

The following sections describe the different parts of the aeroelastic model for the undeformable airfoil and the approaches employed to solve the system in the frequency and time domains. The validation of the model

is presented in the following chapter, together with a discussion of the obtained numerical results.

2.1 Structural model

2.1.1 Reference systems

The position of the points on the airfoil section are given according to a local reference system. The reference frame extends along the airfoil chord (Figure 2.1), it has origin at the half chord point and positive direction toward the trailing edge. The coordinates on the system are given in dimensionless form, distances from the origin are in fact normalized with respect to the half chord length b_{hc}; the coordinates for the leading and trailing edge are hence, respectively $\varepsilon_{le} = -1$ and $\varepsilon_{te} = +1$, while the quarter-chord and three-quarter-chord have coordinates $\varepsilon_{1/4} = -0.5$ and $\varepsilon_{3/4} = +0.5$.

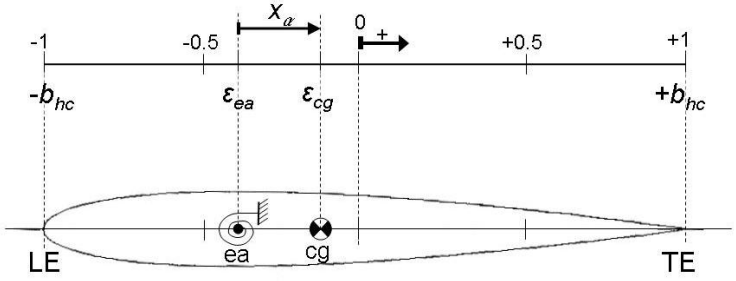

Figure 2.1: Local chord dimensionless coordinate system. The origin is at the half chord point, the point positions are normalized with respect to the half chord length b_{hc}

In this first part of the investigation, the airfoil is considered as rigid, it can not deform and it moves in the plane, the motion is hence fully described by three degrees of freedom, defined according to the global coordinates system represented in Figure 2.2. The streamwise motion is defined with respect to the x axis, which is parallel to the free stream flow direction (assumed constant) and it points aft (toward the te). The heaving motion is defined on the y axis, positive upwards, and a third degree of freedom describes the torsion or pitch rotation of the airfoil as the angle α between the airfoil chord and the x axis. The axis of rotation coincides with the airfoil elastic axis, which passes by the point of coordinate ε_{ea}, that can be thus seen as the section hinge point. A positive torsion-pitch angle corresponds to a clockwise, 'nose up', rotation around this point and, since the free stream flow direction is assumed to be constant, the pitch angle α is also equal to the static angle of attack.

The 2D airfoil section is considered as representative of a transversal section, normal to the span axis, of a wind turbine blade; from this point

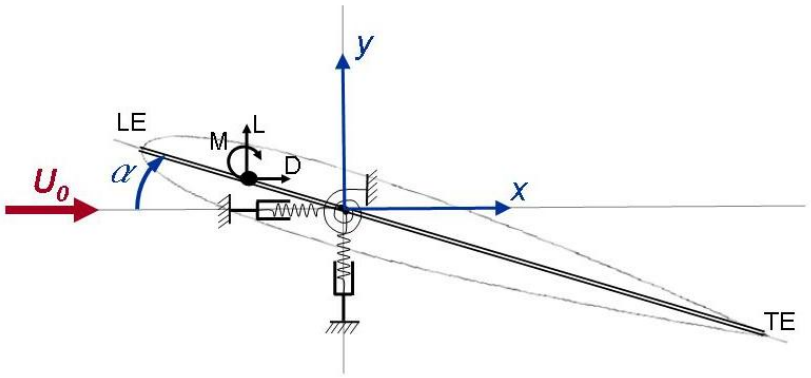

Figure 2.2: Global reference system. The rigid motion of the airfoil section in the plane is defined by three degrees of freedom: x stream wise, y heave, α pitch rotation (positive nose up)

of view, the heave displacement of the section can be roughly related to the flapwise bending of the blade, the streamwise to the edgewise bending and the pitch rotation to the blade torsion.

2.1.2 Dimensionless parameters

In literature [7, 22] the structural characteristics of an airfoil section are often expressed in normalized form by using dimensionless parameters. The parameters that appear more frequently in this work are described in the following lines, their symbols and definitions are similar to the ones given in the quoted references.

- Dimensionless static unbalance x_α. The moment of static unbalance S_α is normalized with respect to the airfoil mass and the half chord length, the parameter is thus equal to the distance between the elastic axis and the centre of gravity, expressed in half chord units. It is positive if the centre of gravity lies aft of the elastic axis.

$$x_\alpha = S_\alpha/(m_{tot} b_{hc}) = \varepsilon_{cg} - \varepsilon_{ea}, \tag{2.1}$$

$$S_\alpha = m_{tot}(\varepsilon_{cg} - \varepsilon_{ea}) b_{hc}. \tag{2.2}$$

- Dimensionless radius of gyration r_α. It is the second moment of area

I_{ea} with respect to the elastic axis, normalized by the mass,

$$r_\alpha = \sqrt{\frac{I_{ea}}{m_{tot} b_{hc}^2}}, \tag{2.3}$$

$$\begin{aligned} I_{ea} &= \int_{le}^{te} \rho^{2D} (\varepsilon - \varepsilon_{ea})^2 b_{hc}^2 \mathrm{d}\varepsilon \\ &= I_{cg} + m_{tot} (\varepsilon_{cg} - \varepsilon_{ea})^2 b_{hc}^2. \end{aligned} \tag{2.4}$$

Where, ρ^{2D} is the density along the chord of the airfoil section, referred to a unit span, it is hence measured in kg/m^2. The total mass of the airfoil section for a unit span, in kg/m, is thus

$$m_{tot} = \int_{-1}^{+1} \rho^{2D} b_{hc} \, \mathrm{d}\varepsilon. \tag{2.5}$$

- Section density ratio. The mass per unit span of the section is divided by the mass of the surrounding fluid,

$$m_{tot}/(\pi \rho b_{hc}^2). \tag{2.6}$$

- Heave-torsion frequency ratio.

$$\omega_y/\omega_\alpha, \tag{2.7}$$

where the frequencies ω refer to the uncoupled natural frequencies in the heave (ω_y) and torsion (ω_α) degrees of freedom:

$$\omega_y = \sqrt{k_y/m_{tot}}, \tag{2.8}$$

$$\omega_\alpha = \sqrt{k_\alpha/I_{ea}}. \tag{2.9}$$

Similarly, the streamwise-torsion frequency ratio is defined as the ratio between the streamwise degree of freedom uncoupled natural frequency ω_x and the torsion one ω_α.

- Reduced wind speed. The wind speed is normalized by the half-chord length and the torsion natural frequency,

$$Red_U = U/(b_{hc}\omega_\alpha). \tag{2.10}$$

2.1.3 Equations of motion

The structure consists of a rigid airfoil section suspended by elastic springs with linear damping and is similar to the model described by Buhl et al. in [8]. The three degrees of freedom that describe the motion of the rigid airfoil

in the plane (Fig.2.2) yield to three equations of motion: two to define the translation in the heave y and streamwise x degrees of freedom, and one for the rotation specified by the pitch-torsion degree of freedom α.

The first two equations of motion are obtained from the balance of inertial, damping, elastic and aerodynamic forces along the horizontal x and the vertical y axes, while the third equation results from the balance of the pitching moments acting on the airfoil. The dynamic of the structure is thus described by a set of three second order differential equations:

$$m_{tot}\ddot{x} - S_\alpha \sin(\alpha)\ddot{\alpha} + c_x\dot{x} + k_x x = D_{aed}, \quad (2.11)$$

$$m_{tot}\ddot{y} - S_\alpha \cos(\alpha)\ddot{\alpha} + c_y\dot{y} + k_y y = L_{aed}, \quad (2.12)$$

$$-S_\alpha \sin(\alpha)\ddot{x} - S_\alpha \cos(\alpha)\ddot{y} + I_{ea}\ddot{\alpha} + c_\alpha\dot{\alpha} + k_\alpha\alpha = M_{aed}. \quad (2.13)$$

Where: m_{tot} is the total mass of the airfoil referred to unit span; S_α is the moment of static unbalance; I_{ea} is the second moment of area with respect to the elastic axis; c_{dof} is the viscous damping coefficient ($c_{dof} = 2\xi_{dof}\omega_{dof}m_{tot}$)and k_{dof} is the stiffness of the linear-elastic springs.

D_{aed}, L_{aed} and M_{aed} are instead, respectively, the drag, the lift and the pitching moment. They represent the interaction between the structure and the fluid and they express the coupling between the structural model and the aerodynamic one, presented in the following section.

2.2 Aerodynamic model

From the interaction between the airfoil and the surrounding fluid, aerodynamic forces are originated and act on the airfoil itself, as a lift L_{aed}, a drag D_{aed} and a pitching moment M_{aed}. An unsteady aerodynamic model defines the forces under the assumptions of 2D incompressible flow, moderate (but arbitrary) movements of the airfoil and fully attached potential flow. The latter restriction limits the validity of the model to small angles of attack where no stall occurs on the airfoil, which is anyway a realistic hypothesis for an airfoil mounted on the outer section of a pitch regulated blade.

The model is implemented following the formulation given by Hansen et al. in [15]. The drag and the moment are related to the unsteady lift. Furthermore, since the expressions for the aerodynamic forces are not linear due to the streamwise degree of freedom x, they are linearised with respect to a specified steady state, prior to stability analysis in the frequency domain.

2.2.1 Lift Force

The total lift on the moving airfoil is split into a *circulatory* contribution and a *non-circulatory* one. The latter, also known as *virtual* or *added mass* contribution, returns the force that would anyway act on the airfoil in motion even if no circulation were produced. The non-circulatory terms arise, in

fact, from the inertial forces of the fluid mass accelerated with the airfoil, consequently, they are not affected by the wake memory effects and they only depend on the actual instantaneous motion of the airfoil [25]. The non-circulatory contribution to the lift is computed as:

$$\begin{aligned} L_{nc} = & \rho b_{hc}^2 \pi (U_0 - \dot{x})\ \dot{\alpha} \\ & - \rho b_{hc}^2 \pi\ \ddot{y} - \rho b_{hc}^3 \pi \varepsilon_{ea}\ \ddot{\alpha}. \end{aligned} \tag{2.14}$$

Where, ρ is the fluid specific weight ($1.225\ kg/m^3$), and U_0 is the undisturbed free-stream flow velocity in the x direction; the flow velocity relative to the airfoil is then equal to the free-stream speed decreased by the $\dot{x}$ component of the airfoil motion: $U_0 - \dot{x}$.

The *circulatory* contribution to the lift takes into account also the unsteady time lag effects caused by the vorticity shed into the wake. In the implemented model, this is achieved by introducing the term α_{eff}, which represents the equivalent effective angle of attack that, if set in steady conditions, would produce a lift force equivalent to the circulatory unsteady-instantaneous one. The circulatory contribution to the lift force is thus computed as

$$L_{circ} = (2\pi)\rho b_{hc}(U_0 - \dot{x})^2(\alpha_{eff} - \alpha_{lift,0}), \tag{2.15}$$

where, 2π is the linear static lift coefficient ($\frac{\partial C_l}{\partial \alpha}$) for a flat plate, and $\alpha_{lift,0}$ is the angle of attack corresponding to a null static lift coefficient, and is 0 for flat plate and not cambered airfoils. The effective angle of attack α_{eff} is then determined by using an approximation for the indicial function of lift, as presented in section 2.2.4.

2.2.2 Drag force

The total drag force is given, as in Hansen et al. [15], by the sum of a static contribution and an induced drag. The former is simply retrieved from the static drag curve of the airfoil at the effective angle of attack α_{eff}, and is null whenever the airfoil is approximated by a thin flat plate and the viscous drag is neglected. The induced drag is instead given by the circulatory lift (2.15) component in the x-direction, this drag component is thus the result of the angular difference between the (unsteady) effective angle of attack and the (steady) geometric one.

$$D_{aed} = D_{static} + \Delta D_{induced}, \tag{2.16}$$

$$D_{static} = \rho b_{hc}(U_0 - \dot{x})^2 C d_{(\alpha_{eff})}, \tag{2.17}$$

$$\Delta D_{induced} = L_{circ}(\alpha - \alpha_{eff}). \tag{2.18}$$

2.2.3 Pitching Moment

The aerodynamic pitching moment is also computed as a sum of non circulatory and circulatory contributions. The non circulatory, or added mass, pitching moment for the airfoil hinged at the elastic axis point, is computed as

$$M_{nc} = -\rho b_{hc}^3 \pi (U_0 - \dot{x})(0.5 - \varepsilon_{ea})\ \dot{\alpha} - \rho b_{hc}^3 \pi \varepsilon_{ea}\ \alpha\ddot{x} - \rho b_{hc}^3 \pi \varepsilon_{ea}\ \ddot{y} - \rho b_{hc}^4 \pi (1/8 + \varepsilon_{ea})\ \ddot{\alpha}. \tag{2.19}$$

The circulatory part originates from the circulatory lift and the drag forces, which are considered acting at the quarter-chord point $\varepsilon = -0.5$, furthermore, in case of cambered airfoil, a term expressing the static moment at the effective angle of attack is also present:

$$M_{circ} = (\varepsilon_{ea} + 0.5)\cos(\alpha)\ L_{circ} + (\varepsilon_{ea} + 0.5)\sin(\alpha)\ D_{aed} + \rho b_{hc}^2 (U_0 - \dot{x}) Cm_{(\alpha_{eff})}. \tag{2.20}$$

For small torsion angles α, the drag contribution to the moment can be neglected.

2.2.4 Unsteady wake effects: indicial function approach

The effective angle of attack α_{eff} is expressed through an *indicial function of lift* φ that models the deficiency in the instantaneous lift, compared to the steady one, and it represents the effects of the vorticity shed into the wake by the airfoil undergoing arbitrary motion. In the case of interest, the arbitrary motion is described as a superposition of step changes in the airfoil angle of attack, the corresponding indicial function φ is referred to as Wagner's indicial function and consists in a Fourier's superposition integral.

This integral can not be represented in a simple analytical form, the indicial function is thus approximated by a series of exponential time-lag terms [15, 9, 25, 7]:

$$\varphi(\tau) \approx 1 - \sum_{i=1}^{n_{lag}} A_i e^{-b_i \tau}, \tag{2.21}$$

where, τ is a dimensionless time variable, $\tau = t/(b_{hc} U_{mean})$, corresponding to the distance, expressed in half-chords, that the airfoil has travelled with respect to the flow. The coefficients A_i and b_i are instead parameters that describe the response of the specific airfoil according to the chosen indicial function approximation, as presented in the following paragraph.

By applying the exponential approximation of the indicial function pre-

sented in Eq. (2.21), the effective angle of attack is then computed as

$$\alpha_{eff} = \alpha_{3/4}\ \varphi_{(0)} + \sum_{i=1}^{n_{lag}} z_i = \alpha_{3/4}\left(1 - \sum_{i=1}^{n_{lag}} A_i\right) + \sum_{i=1}^{n_{lag}} z_i. \tag{2.22}$$

The z_i terms are n_{lag} additional state variables that describe the time lag effects of the wake and they are computed from n_{lag} first order differential equations:

$$\dot{z}_i = -\left(\frac{U_0 - \dot{x}}{b_{hc}} b_i - \frac{\ddot{x}}{U_0 - \dot{x}}\right) z_i + \frac{U_0 - \dot{x}}{b_{hc}} b_i A_i \alpha_{3/4}. \tag{2.23}$$

Here, as in the previous equation (2.22), $\alpha_{3/4}$ is the 'quasi steady' angle of attack, evaluated at the three-quarter chord point:

$$\alpha_{3/4} = \alpha - \frac{\dot{y}}{U_0 - \dot{x}} + \frac{0.5 - \varepsilon_{ea}}{U_0 - \dot{x}} \dot{\alpha}. \tag{2.24}$$

It is worth to notice that due to the streamwise degree of freedom x, also the equations for the time lag variables, as well as the expressions for the lift, the drag and the moment, are not linear in the system state variables. Consequently, to represent the aeroelastic system in a linear formulation, the expressions need to be linearised by means of a Taylor series expansion, the resulting equations are found in Hansen et al. [15] and reported in Appendix A.

Indicial function approximations

The indicial function of lift, approximated to a series of n_{lag} exponential terms, is characterized by n_{lag} couples of coefficients A_i and b_i. Numerical values for the A_i and b_i coefficients have been first calculated by Jones ([17], quoted in [15]) for a two terms approximation of the flat plate response.

A different set of values is computed by Gaunaa [15] and it is based on the simulation of the response of a flat plate undergoing step change of angle of attack, computed by means of a panel code; the A_i,b_i coefficients are then determined seeking the best fitting between the response approximated by the exponential terms series and the actually simulated one. The same method is also applied to simulate the response of an airfoil with finite thickness and compute the coefficients for the series of exponential terms that approximate such response [15, 8]. The number of terms in the series can be arbitrarily chosen, the higher it is, the closer will be the fitting, but also the more differential equations will be introduced in the system to compute the aerodynamic state variables.

As remarked in Hansen et al. [15], the possibility of applying indicial function approximations to the response of non-flat airfoils has not been

formally proved. Nevertheless, the unsteady responses of airfoils with finite thickness computed with the approximated method shows good agreement with results from Navier-Stokes numerical solutions [15].

Table 2.1 reports the coefficients of exponential terms series that approximate the response of a flat plate, with two (Jones) and three (Gaunaa) terms, and also the coefficients computed by Gaunaa [8] for the Risø B1-18 airfoil, which has been employed in the previous aeroelastic studies of a flap equipped section. The corresponding approximated lift indicial functions are plotted in Figure 2.3 versus the dimensionless time.

	Flat Plate		Risø B1-18	
	Jones	*Gaunaa*	*2 terms*	*3 terms*
A_1	0,1650	0,0182	0,2446	0,0821
A_2	0,3350	0,2411	0,3743	0,1429
A_3	–	0,2407	–	0,3939
b_1	0,0455	$3{,}02E-06$	0,0519	0,0199
b_2	0,3000	0,3989	0,3371	0,7817
b_3	–	0,0818	–	0,1453

Table 2.1: Approximated indicial function of lift $\varphi(\tau)$ for the response to a step change in the angle of attack. Coefficients for the terms in the exponential series, for flat plate (Jones [17] and Gaunaa [15]) and Risø B1-18 airfoil (Gaunaa [8]) responses.

It can be observed (Figure 2.3) that the response curves referred to the airfoil with finite thickness are below the flat plate ones, showing a slower response in the airfoil case. Furthermore, the 2 and 3 terms approximations in the flat plate case return similar responses, while the effects of introducing a third term are more evident in the B1-18 airfoil response.

2.3 Aeroelastic system

The aeroelastic behaviour of the airfoil interacting with the surrounding flow is described by the presented equations of motion, together with the expressions for the aerodynamic forces and for the wake time lag variables.

The equations of motion consists in three, one for every degrees of freedom, second order differential equations, that, by variable substitution of the second order derivatives, are reformulated in a set of three plus three first order equations (*state-space formulation*). In addition, the aerodynamic model also introduces in the system n_{lag} time lag variables z_i and the same number of first order equations (2.23).

The complete set of equations describing the aeroelastic system can be written in matrix formulation as

$$\boldsymbol{M}_{nl}\underline{\dot{\boldsymbol{x}}} \;=\; \boldsymbol{A}_{nl}\underline{\boldsymbol{x}} + \underline{\boldsymbol{f}}_{nl}, \tag{2.25}$$

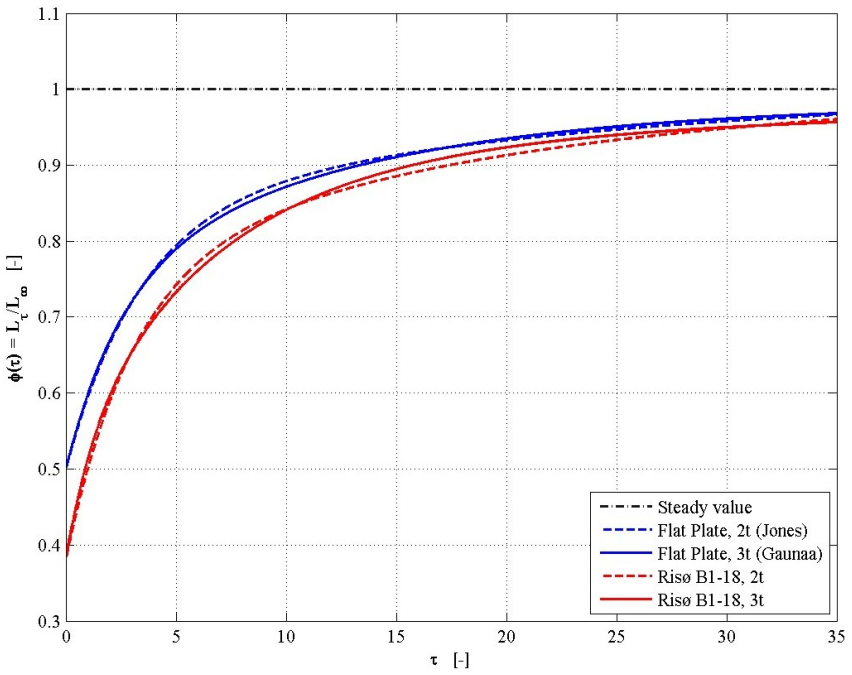

Figure 2.3: Approximated indicial function of lift $\varphi(\tau)$ versus dimensionless time, step responses for a flat plate and a Risø B1-18 airfoil. 2 and 3 terms series approximations.

where, $\underline{\boldsymbol{x}}$ is a vector that collects the state variables of the system in the state-space formulation, and, in case of a three terms approximation of the lift indicial function φ, it may looks like

$$\underline{\boldsymbol{x}} = \left\{ x, y, \alpha, \dot{x}, \dot{y}, \dot{\alpha}, z_1, z_2, z_3 \right\}^T. \tag{2.26}$$

In this formulation, the square matrices $\boldsymbol{M}_{nl}$ and $\boldsymbol{A}_{nl}$ and the force vector $\underline{\boldsymbol{f}}_{nl}$ are also functions of the system state variables contained in $\underline{\boldsymbol{x}}$, as a consequence, the system is non linear. While non linearities can be handled by a time marching solver, the stability analysis carried out in the frequency domain requires the system to be linearized.

2.3.1 Time domain solution

A time domain solution method can be applied to non linear systems, therefore, as just mentioned, the aeroelastic behaviour of the structure is determined in the time domain by solving directly the non linear system of differential equations, as presented in the matrix formulation of Eq.(2.25).

The implemented time marching code solves the system of first order differential equations by means of a time step numerical integration. The integration is carried out using the Matlab built-in function *ode45*, which is based on an explicit Runge-Kutta method of the fourth and fifth order, with a variable time step. The required initial conditions are specified by assigning the values of the system state variables in $\underline{\boldsymbol{x}}$, at time zero. In all the simulations, the initial condition vector $\underline{\boldsymbol{x}}_{t=0}$ is chosen so to represent a steady state (derivatives terms are hence zero) close to the equilibrium one, but not equal.

The results of the time marching solution are, in fact, time histories of the system state variables contained in the vector $\underline{\boldsymbol{x}}_{(t)}$ and their first order time derivatives $\dot{\underline{\boldsymbol{x}}}_{(t)}$. By choosing an initial condition slightly different from the equilibrium one, it is possible to observe how the time histories evolves in time and if the variables tends to their equilibrium value, and thus determine if the system is stable or not.

The stability results obtained for the linearised system in the frequency domain can be hence checked versus the stability observed in the corresponding non linear system, solved in the time domain by the time marching code.

2.3.2 Frequency domain solution

If the primer concern of the aeroelastic investigation is the stability of the system in a defined state, the analysis can be more efficiently carried out in the frequency domain [23, 12, 11]. In fact, the advantage of such approach is that the computationally expensive time step numerical integration that is required to determine the system behaviour in the time domain, can be

skipped. On the other hand, the frequency domain solution, which is based on an eigenvalue problem, only applies to a linear system.

The aeroelastic system (2.25) is thus linearised with respect to a predefined equilibrium steady state by applying a Taylor's series expansion around the same equilibrium state. The obtained linearised equations are reported in Appendix A, where the linearised expressions for the aerodynamic forces are retrieved from Hansen et al. [15]. The equilibrium state, around which the system is linearised, is defined by a state variables vector $\underline{\boldsymbol{x}}_{0,sts}$, the vector describes a steady condition, the derivatives terms are therefore null, and, among the structural degrees of freedom only the pitch angle $\alpha_{0,sts}$ is actually affecting the system proprieties.

The set of linearized equations can be presented in matrix formulation

$$\tilde{\boldsymbol{M}}\dot{\underline{\boldsymbol{x}}} = \tilde{\boldsymbol{A}}\underline{\boldsymbol{x}} + \underline{\boldsymbol{f_0}}. \tag{2.27}$$

The system is then assumed to have a solution in the form

$$\underline{\boldsymbol{x}} = \underline{\boldsymbol{\phi}}\mathrm{e}^{\lambda t}, \tag{2.28}$$

which, substituted into the linearised system matrix equation (2.27), yields to the *generalized eigenvalue* problem:

$$(\tilde{\boldsymbol{A}} - \lambda\tilde{\boldsymbol{M}})\underline{\boldsymbol{\phi}} = \underline{\boldsymbol{0}}. \tag{2.29}$$

The eigenproblem is solved numerically by means of the built-in Matlab function *eig* and it results in a set of complex eigenvalues λ_j and respective eigenvectors $\underline{\boldsymbol{\phi}}_j$. The imaginary part of every eigenvalue j $\mathrm{Im}(\lambda_j)$ is equal to the modal frequency, in rad/s, of mode j and is referred to as *frequency parameter*, while the real part $\mathrm{Re}(\lambda_j)$ is known as *stability parameter* and is related to the logarithmic damping associated to mode j. A negative eigenvalue real part corresponds to a positively damped modal contribution, the modal logarithmic damping is in fact computed as

$$\delta_j = -\frac{\mathrm{Re}(\lambda_j)}{\mathrm{Im}(\lambda_j)}. \tag{2.30}$$

Stability analysis is thus carried out in the frequency domain by verifying that for an assigned steady state of the system and a given wind speed U_0, all the modes are positively damped (stable condition). The flow speed at which any of the modes turns unstable (negatively damped) then corresponds to the stability limit for the specified system.

Mode tracking

The generalized eigenproblem for the linearised system is solved in a series of points, or steps, with increasing wind speed. The solution consists in a

set of eigenvalues λ_j and corresponding eigenvectors $\underline{\phi}_j$, the order given to the modes at every step can be arbitrary, but it is here chosen to ordinate them according to a 'self-similarity' principle applied to the modal shapes. In other words, for successive flow speed steps the modes are numbered so that the shape vectors corresponding to the same mode number are the most similar.

In fact, while the eigenvalues convey information about the modes stability and frequency, the eigenvectors determine the corresponding modal shape. Only the eigenmodes corresponding to a non-negative frequency parameter ($\mathrm{Im}(\lambda_j)$) are retained, and the respective modal vectors are collected in the matrix

$$\boldsymbol{\Phi} = \left\{ \underline{\phi}_1, \underline{\phi}_2, \ldots, \underline{\phi}_n \right\}. \tag{2.31}$$

The similarity of the mode shapes is then determined by means of a *Modal Assurance Criterion* (MAC). The criterion, as defined in [1], produces a number between 0 and 1, and is an index of the degree of similarity between 'test' and 'reference' modal vectors. If two vectors are identical or they are linear combinations of the same vector, a unit MAC value is obtained. The classic expression to compute the MAC value between two vectors [1] is modified to operate directly on the modal shape matrices $\boldsymbol{\Phi}$. The result is also a matrix $\boldsymbol{MAC}_{\boldsymbol{\Phi}}$,

$$\boldsymbol{MAC}_{\boldsymbol{\Phi}} = \frac{\left(\boldsymbol{\Phi}_{Ref}^H \boldsymbol{\Phi}_{Test}\right) \bullet \left(\boldsymbol{\Phi}_{Test}^H \boldsymbol{\Phi}_{Ref}\right)^T}{\mathrm{diag}\left(\boldsymbol{\Phi}_{Ref}^H \boldsymbol{\Phi}_{Ref}\right) \quad \mathrm{diag}\left(\boldsymbol{\Phi}_{Ref}^H \boldsymbol{\Phi}_{Test}\right)^T}. \tag{2.32}$$

The $\bullet$ symbol indicates an element by element product, as well as that, also the quotient given by the fraction should be intended as an element-wise operation. The H superscript is used for the conjugate-transpose operation, the T one for the transpose.

The reference modal shapes matrix $\boldsymbol{\Phi}_{Ref}$ contains the eigenvectors from the previous time step, already ordered. The test matrix $\boldsymbol{\Phi}_{Test}$ collects the modal shapes from the actual step. Every element of the result matrix $\boldsymbol{MAC}_{\boldsymbol{\Phi}i,j}$ gives the correlation between the pair of modal shapes $\underline{\phi}_i$ and $\underline{\phi}_j$, where the former, corresponding to the row number, is the reference modal shape, and the latter is the test one. The n-th column in the ordered modal matrix $\boldsymbol{\Phi}$ is thus assigned to the modal shape vector corresponding to the maximum value (highest similarity) in the n-th row of the $\boldsymbol{MAC}_{\boldsymbol{\Phi}}$ matrix. The reference vector for the very first time step has an arbitrarily chosen order, and in this case a decreasing modal frequency criterion is adopted.

By using the similarity criterion is possible to track and identify the different modes in the full range of investigated wind speed despite the changes of frequencies or degrees of freedom contributions. In this way, a mode of particular interest, as for instance the mode causing flutter, can be traced

back and related to the mode that is more similar to it in no flow conditions.

2.4 Aeroelastic instabilities

The stability of a system is determined in relation to an equilibrium state. If the system, undergoing small perturbations, tends to re-assume the same equilibrium state then is *stable*. If others, or even none, equilibrium points are reached, the system in the specified conditions is *unstable* [23].

From a practical point of view, instability would yield to not ordinary structural deformations that, even though in some cases possibly limited by non linear effects, may result in structural failures or anyway important reduction of the component life time.

Two kind of instabilities can occur in the described aeroelastic system: divergence and flutter. The following paragraphs define their characteristics and how they appear both in the time and frequency domain solutions.

Divergence Divergence is a static phenomenon and it depends on the equilibrium between the aerodynamic pitching moment and the torsion spring restoring moment. In the time marching solution it appears as an exponential growth in the pitch-torsion degree of freedom, with none or damped oscillations in case of pure divergence. In the eigenproblem solution, a divergence instability is instead characterized by one mode with negative modal damping (positive $\mathrm{Re}(\lambda)_{\tilde{j}}$) and, since the phenomenon is static, the respective modal frequency is null ($\mathrm{Im}(\lambda)_{\tilde{j}} = 0$). If the instability is purely given by divergence, all the other modes are positively damped (negative $\mathrm{Re}(\lambda)$).

As mentioned, divergence occur at flow speeds for which the increase in the aerodynamic pitching moment is greater than the respective torsional restoring moment. The divergence limit can be thus computed through an analytical expression that only depends on the torsion spring stiffness k_α and the location of the elastic axis ε_{ea} [7]. The expression reads

$$U_{Div} = \sqrt{\frac{k_\alpha}{(2\pi)\rho b_{hc}^2(0.5+\varepsilon_{ea})}}, \tag{2.33}$$

and, in reduced dimensionless form:

$$\frac{U_{Div}}{b_{hc}\omega_\alpha} = \sqrt{\frac{m_{tot}\ r_\alpha^2}{(2\pi)\rho b_{hc}^2(0.5+\varepsilon_{ea})}}. \tag{2.34}$$

Where, 2π is the linear static lift coefficient ($\frac{\partial C_l}{\partial \alpha}$) for a flat plate; ω_α is the uncoupled natural frequency in the pitch degree of freedom: $\omega_\alpha = \sqrt{k_\alpha / I_{ea}}$. The term r_α is instead the radius of gyration, given by the section moment of inertia I_{ea} normalized with respect to the mass, section 2.1.2.

Flutter Flutter is a more complex dynamic phenomenon that involves the coupling of two, or more, degrees of freedom, typically the heave and the torsion. In the responses obtained by the time marching tool, flutter is characterized by oscillations around the equilibrium value, with an amplitude that would indefinitely increase, unless limited by non linear effects. In the frequency domain, instead, flutter is characterized by at least one mode with a positive eigenvalue real part (negative modal damping) and a positive frequency parameter $\mathrm{Im}(\lambda)$, which is referred to as flutter frequency.

Due to the complexity of the dynamic instability, the limit flow speed at which flutter may start to occur can not be computed by simple analytical equations, nevertheless, Theodorsen [22] proposes an empirical equation to approximate the flutter limit. The validity of the expression is limited to heavy sections and small values of the ratio between the heave and torsion uncoupled natural frequencies (ω_y/ω_α). The empirical equations in dimensional and dimensionless forms read:

$$U_F = \sqrt{\frac{k_\alpha}{\pi\rho b_{hc}^2(1+2\varepsilon_{cg})}}, \tag{2.35}$$

$$\frac{U_F}{b_{hc}\omega_\alpha} = \sqrt{\frac{m_{tot}\ r_\alpha^2}{\pi\rho b_{hc}^2\ (1+2\varepsilon_{cg})}}. \tag{2.36}$$

The empirical approximation for the flutter speed is a function of the torsional stiffness and the position of the centre of gravity, it does not depends on the elastic axis position, which instead determines the divergence limit.

Chapter 3

Undeformable airfoil. Results and discussion

The model described in the previous chapter is now employed to investigate the aeroelastic stability of two different airfoil sections. First, stability curves are computed for the 'typical section' described by Theodorsen and Garrick [22], which consists in a suspended thin flat plate with defined structural characteristics (validation case section). The results are then compared with the ones presented in literature for this same case, and the model and its implementation are thereby validated. The same thin plate section is also employed to verify the sensitivity of the stability limits to variations in the structural parameters and in the formulation of the aerodynamic model.

The second section being investigated (reference case section) is the one that, in the second part of the work, will be 'equipped' with the deformable trailing edge flap control. The section is chosen so to have the same characteristics, both structural and aerodynamic, as the one studied in the previous 2D works concerning the load reduction potential achievable with the trailing edge flap [4, 8].

The flutter limit computed for the undeformable section will thus serve as comparison term in the following investigations of the flap effects. As well as that, an analysis of the influence of the streamwise degree of freedom on the stability limits is also carried out using the same section as input.

3.1 Airfoil section for validation case

The implemented stability tool is validated by solving some of the instability cases that classic literature reports for undeformable airfoil sections. The term of comparison is in fact given by Theodorsen and Garrick's [22] analysis of the 'flexure-torsion' flutter on wing sections, modelled as flat plates.

The same set of structural proprieties is adopted both for validation and for a first sensitivity analysis, and it corresponds to the case identified as

(q) in Theodorsen and Garrick [22], in Graph I-A, and then also reported in Bisplinghoff [7] in Figure 9–5(A). The dimensionless parameters that define the structural proprieties are reported in table 3.1, while the aerodynamic model adopts Jones' coefficients (Table 2.1) in the approximation of the indicial response of a thin flat plate, unless specified otherwise.

Parameter	*Symbol*	*Value*
Elastic axis	ε_{ea}	-0.3
Distance c.g.	X_α	0.2 (0.1)
Rad.Gyrat. sq.	r^2	0.25
Density ratio	$m_{tot}/(\pi\rho b_{hc})$	20
Heave-Tor. ratio	ω_y/ω_α	$0 \rightarrow 1.7$

Table 3.1: Dimensionless structural parameters for the validation case section. The section is employed for validation, by comparison with the results obtained by Theodorsen and Garrick with the same inputs, case (q) in [22], and for a first sensitivity analysis.

3.1.1 Validation results

Stability limits are then computed and plotted as function of a range of heave-torsion frequency ratios ω_y/ω_α (Fig. 3.1). The resulting flutter speeds are found to be in agreement with Theodorsen and Garrick's original results only for low frequency ratios, in fact, as the ratio approaches unit value, the actual curves drift to generally lower speeds.

The mismatch is probably due to numerical inaccuracies in the curves presented in the original work. In fact, according to Zeiler [26], Theodorsen and Garrick's results may be biased by a low numerical accuracy, most likely referable to the scarce computational power available at the time. For the same wing section, Zeiler reports flutter speeds very close to the computed ones, square marks in Fig. 3.1. The results of the present model are also found to be in good agreement with the ones obtained by Gaunaa's [10] reimplementation of the same method described in Theodorsen and Garrick's report.

The model and its implementation are hence validated. Besides that, it is also observed that the streamwise degree of freedom x, included in the present model and not in Zeiler and Gaunaa's computations, does not modify the stability limits computed in this case.

3.1.2 Flutter limits sensitivity

The same airfoil section specified in the validation case (Table 3.1) is now used to asses the sensitivity of the computed flutter limits to variations in the structural inputs and also to determine how different approximation in the

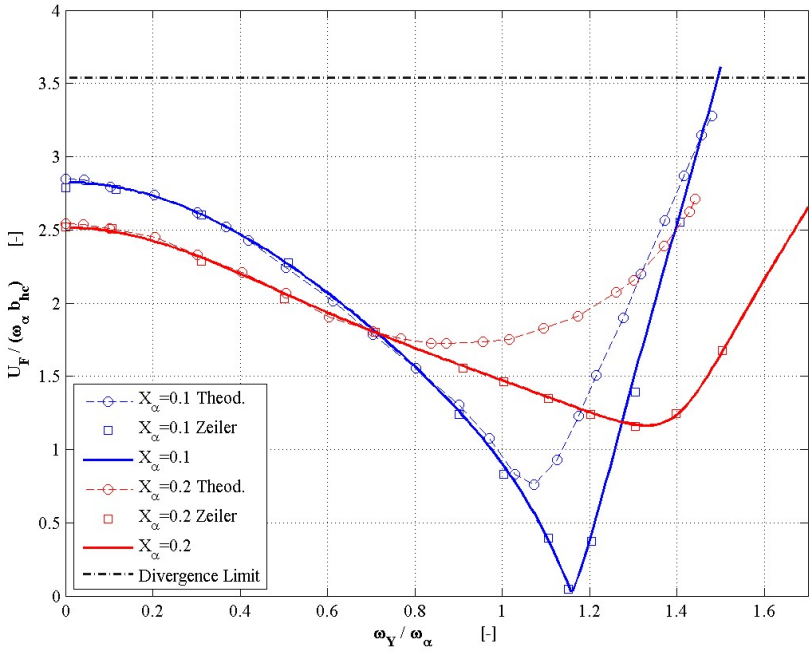

Figure 3.1: Reduced flutter speed limits and divergence limits vs. heave-torsion frequency ratio for the validation case section. Validation of the model by comparison with Theodorsen's results and Zeiler's correction.

aerodynamic model may affect the result. Since the sensitivity to structural inputs is a rather classic issue and is well represented in literature [7, 22], the actual section focuses more on the aerodynamic model influence and only summarizes the effects of structural parameters, referring to Appendix B for a more detailed presentation.

Sensitivity to structural parameters

The effects of the dimensionless parameters that describe the structure are investigated by varying only a single parameter per time, for instance, if the mass ratio is increased, the natural frequencies are constant, and hence the springs stiffness need to be raised. This approach, even though difficult to actuate in practice, is the same followed by Theodorsen and Garrick [22], since it allows to isolate the effects of each parameter.

Flutter curves are computed in the investigated frequency range for different elastic axis position, mass density ratio, radius of gyration and structural damping ratios; plots are reported in Appendix B.

It is observed that, in the range of low heave-torsion frequency ratios, which is the one of more interest for wind turbine blades, the flutter speed depends on the position of the section centre of gravity ε_{cg} and not on the elastic axis location ε_{ea}. As well as that, structural damping has no effect on the stability limits for low heave frequencies, the flutter speed of the blade section is in fact nearly not varied even though strong structural damping is introduced.

Sensitivity to aerodynamic model

The flutter limits reported in the previous plots are all computed using the full unsteady formulation for the aerodynamic model, as described in the previous chapter, section 2.2; Jones' coefficients are employed in the indicial function of lift. Now, different approximations and hypothesis in the aerodynamic modelling are employed, and the sensitivity of the stability limits to this variations is determined. Flutter speeds are computed for a section with the same structural proprieties as defined in the validation case (Table 3.1), the results are then plotted in Figure 3.2.

First, the effects of assuming a thin plate response are assessed, thus the indicial function approximation is changed from the flat plate one (blue curves) to the function tuned to match the response of the Risø B1-18 airfoil (red lines), two (dashed lines) and three terms (full lines) approximations are investigated; the values for the coefficients A_i and b_i of the exponential terms in the response function approximation, are reported in Table 2.1, page 20.

A part from that, a common simplification in the aerodynamic modelling is to assume a 'quasi-steady' response, and thus avoid the computation of

the indicial function φ and set it to a constant unit value; the flutter limits computed according to this hypothesis are represented by the green curves in Figure 3.2. The stability curves reported with dotted lines are instead obtained by neglecting the contribution of the added mass acceleration terms ($\ddot{\alpha}$ and $\ddot{y}$) in the non circulatory lift, eq. (2.14), and moment, eq. (2.19).

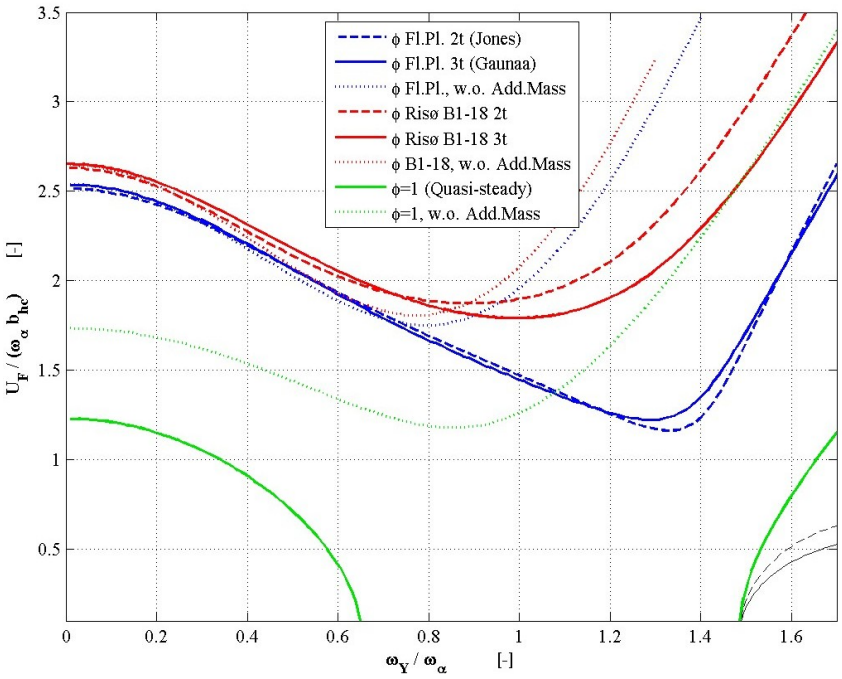

Figure 3.2: Flutter limits for the section defined in the validation case, with $x_\alpha = 0.2$. Sensitivity of the stability curves to approximations of the indicial response function: flat plate (blue) and Risø B1-18 airfoil (red) response, 2 (dashed lines) and 3 (full line) terms approximation. Quasi-steady response assumption (green): $\varphi = 1$. Effects of neglecting acceleration terms in the non circulatory lift and moment (dotted lines).

The stability limits computed by using a two terms approximation of the indicial response function are slightly underestimated (nearly 1% at a frequency ratio of 0.1) in the low frequencies range, for both the flat plate and the non-flat airfoil case. Although, as the frequency ratio increases, the stability limits for the flat plate are still similar for both the 2 and 3 terms approximations, but in the case of airfoil with finite thickness, the 2 terms approximation results in higher flutter speeds (non conservative).

The indicial response function of the flat plate yields to flutter limits (blue lines in Fig.3.2) that are generally lower than the ones based on the Risø B1-18 indicial function approximation (red lines). The flat plate flutter velocity is, for instance, about 5% lower then the one predicted with a tick airfoil response, at a frequency ratio of 0.1. Besides that, in the B1-18 case

a small region of instability is reported for high frequencies and low reduced speeds (marked with thin black lines): the system is unstable for very low wind speeds, but by increasing the speed it turns stable again until the flutter limit is reached. A very low structural damping ($\xi = 5 \cdot 10^{-5}$) is sufficient to cancel out the instability region.

The quasi-steady hypothesis (green line in fig.3.2) leads to a largely underestimated flutter limit (nearly half), which, although conservative, may negatively affect design choices. The acceleration terms contribution to the non circulatory lift and moment is scarcely affecting the flutter limit for low frequencies. Indeed, neglecting the acceleration terms in the higher range of frequencies ratios (dotted lines) produces in all the cases non conservative over estimations of the flutter limit. The contribution to non circulatory lift and moment from the angular velocity terms $U\dot{\alpha}$ is instead essential in the whole range of frequencies. If it is neglected, the stability of the system is strongly decreased and completely biased flutter limits are reported.

It can be thus concluded that an unsteady aerodynamic model is necessary in stability simulations. It is also observed that a flat plate indicial response approximation shows a slightly underestimated flutter speed when compared to simulations based on the response of an airfoil with finite thickness. Furthermore, for low frequency ratios, only small variations in the curves derives from the number of terms used in the indicial function approximation and also from the acceleration terms contribution to non circulatory forces.

In case of airfoil section with structural characteristics different from the investigated ones, the conclusions may be not directly apply from a quantitative point of view, but, still, the same qualitative trends are expected.

3.2 Airfoil section for basic reference case

The validated stability tool is now employed to investigate the stability for the same airfoil section that has been considered in the previous 2D studies [8], where the load reduction potential of the flap equipped section was investigated. The section that is adopted as basic reference case, in fact, has the same structural characteristics specified in Buhl [8] and can be described by the dimensionless parameters given in Table 3.2. The airfoil has a Risø B1-18 profile, hence, the response function in the aerodynamic model is based on a three terms approximation, and the coefficients computed by Gaunaa [8] for the same profile are applied, their values are here reported in Table 2.1. The camber of the profile is initially neglected and only afterwards introduced to determine the effects in relation to the streamwise degree of freedom.

The analysis returns the stability limits for the same section that in the following part, as in the previous studies, will be equipped with the trailing

Parameter	*Symbol*	*Value*	*Unit*
Chord Length	$2b_{hc}$	1	m
Distance Elastic Axis–LE		0.3	m
Distance Center Gravity–LE		0.35	m
Total Mass	m_{tot}	40	kg/m
Moment of Inertia wrt CG	I_{cg}	2	kgm^2
Heave natural frq.	$\omega_y/(2\pi)$	1	Hz
Torsion natural frq.	$\omega_\alpha/(2\pi)$	10	Hz
Stream wise natural frq.	$\omega_x/(2\pi)$	2	Hz
Dimensionless parameters			
Elastic Axis position	ε_{ea}	-0.4	–
Distance CG-EA	X_α	0.1	–
Radius of Gyration squared	r^2	0.2	–
Density Ratio	$m_{tot}/(\pi\rho b_{hc})$	41.58	–
Heave-Torsion frq. ratio	ω_y/ω_α	0.1	–
Stream-Torsion frq. ratio	ω_x/ω_α	0.2	–

Table 3.2: Structural characteristics and dimensionless parameters for the airfoil section used as basic reference computational case. The structural proprieties are the same as in Buhl et al. [8].

edge flap; the results represent hence a term of comparison that will be useful in the later investigation of the effects of the elastic and controlled flap on stability.

Furthermore, the same reference section is also used to determine how the presence of the streamwise x degree of freedom in the model affects the computed stability limits. In case of small influence, would be in fact convenient to neglect the movement of the section in the streamwise direction, and simplify thus the aerodynamic model to linear expressions.

3.2.1 Flutter limits

In the investigation that follows, the camber of the airfoil is neglected, that is to say that for zero angle of attack the aerodynamic forces are null, hence, the equilibrium state that is used to linearise the system is characterized by a zero pitch angle $\alpha_{0,sts} = 0$. Nevertheless, the same results can be extended also to the cambered profile case, since, as presented in the following section, neglecting the airfoil camber does not affect the stability limits, whenever a realistic structural damping in the streamwise x direction is considered.

The heave-torsion frequency ratio of the reference case section, is fixed and is rather small, the flutter limits are hence depending on the position of the centre of gravity and not of the elastic axis; furthermore, since the mass density ratio is rather high, the case is in the range of validity of Theodorsen's empirical equation for the flutter speed (2.36). It is thus chosen to compute

and plot the flutter speed for different centre of gravity positions, the position corresponding to the basic reference case ($\varepsilon_{cg} = 0.3$) is then highlighted by a vertical dashed black line (Fig.3.3). The flutter speeds obtained with flat plate indicial function approximation, quasi-steady assumption, and neglecting the acceleration terms are also reported.

Aerodyn. Model	*B1-18*	*Flat Plate*	*Quasi-steady*	*No Acc.*	*Emp.Eq.*
Flutter Vel.[m/s]	142.2	139.6	111.2	144.3	146.7

Table 3.3: Predicted Flutter velocities with the different aerodynamic model approximations. Reference conditions: $\omega_y/\omega_\alpha = 0.2$, $\varepsilon_{cg} = -0.3$.

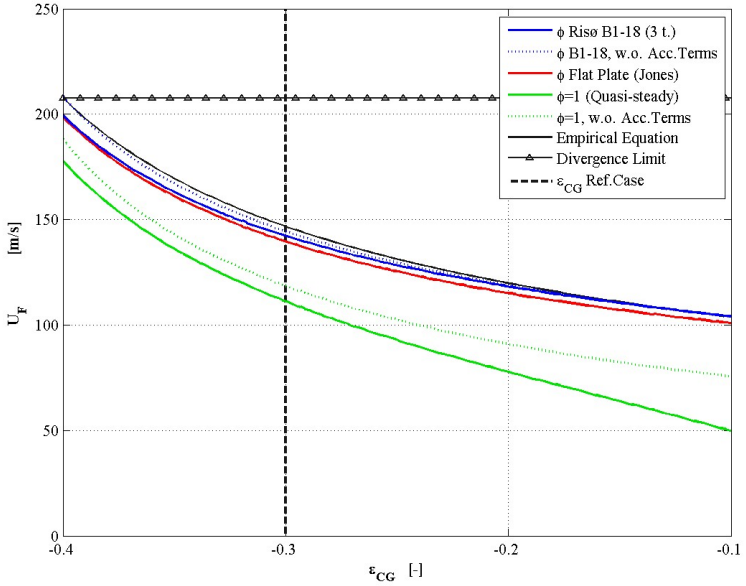

Figure 3.3: Flutter and divergence limits for the airfoil section of the basic reference case, at the vertical dashed black line. The reduced flutter speed is computed for different centre of gravity positions while the torsional stiffness is constant, thus, the torsional frequency varies. Indicial response approximations for Risø B1-18, flat plate and quasi-steady response. Limits computed with Theodorsen's empirical equations are also plotted (black line).

The flutter speed of the undeformable reference section is 142.2 m/s and the empirical equation in spite of its simplicity returns, in this particular case, flutter limits relatively close to the one computed by the stability tool, the overestimation is only about 5 % (Table 3.3).

Besides, as also observed in the section used for validation, the limit computed with a flat plate response is slightly underestimated (nearly 1.8%), while the quasi-steady response assumption (green line in Fig.3.3) would yield to a much lower flutter speed, 22% less in this case. The effect of

neglecting the acceleration terms in the non circulatory forces and moment (dotted lines) is again a small overestimation (0.7%) in the flutter speed (Table 3.3).

It can be then generally observed that the sensitivity to the aerodynamic model for the actual reference airfoil section is lower than the one reported in the previous validation case, probably due to an higher density ratio, nevertheless, still the same qualitative trends are observed.

3.2.2 Influence of the streamwise dof

The streamwise x degree of freedom (dof) seems to have a scarce influence on the stability of the airfoil section, and, at the same time, introduces non linearities in the aerodynamic model. It is thus interesting to investigate in which conditions the movement in the streamwise direction could be neglected so to obtain a simpler formulation, without affecting the accuracy of the computed stability limits.

Influence for non-cambered airfoil

A non-cambered airfoil is symmetric and has no lift or pitching moment acting on it when the angle of attack is zero; consequently, one equilibrium state corresponds to a null pitch angle, and this condition is applied in the steady state with respect to which the system is linearised: $\alpha_{0,sts} = 0$. A flat plate can be considered as a particular kind of non-cambered airfoil, and, in the stability computations carried out for the validation section (see 3.1.1), it is observed that the streamwise degree of freedom, included in the actual model but not in the ones used as reference, does not modifies the stability limits.

The analysis in the reference section case yields to the same conclusion: if the camber of the profile is neglected, the flutter limits are not affected by the streamwise degree of freedom. Furthermore, it is also observed that the mode related to this degree of freedom does not influence the dynamic of the other modes involved in the system.

In fact, by plotting the modal frequencies as function of the wind speed for the reference case structure (Fig. 3.4), it is observed that the mode related to the x dof maintains a constant frequency, which is equal to the uncoupled natural one, in all the range of wind speeds. On the contrary, the other two modes show the 'classic flutter' trend: they start from a value close to the respective natural frequencies, then, as the wind speed increases they show coupling effects and the frequencies get closer, up to a point just before the flutter limit; the flow speed at which flutter occur is marked by the vertical dashed line, Figure 3.4.

Similar behaviour is observed in the modal damping (Fig.3.5): once again the value for the second mode, related to the x dof, is constant in all the

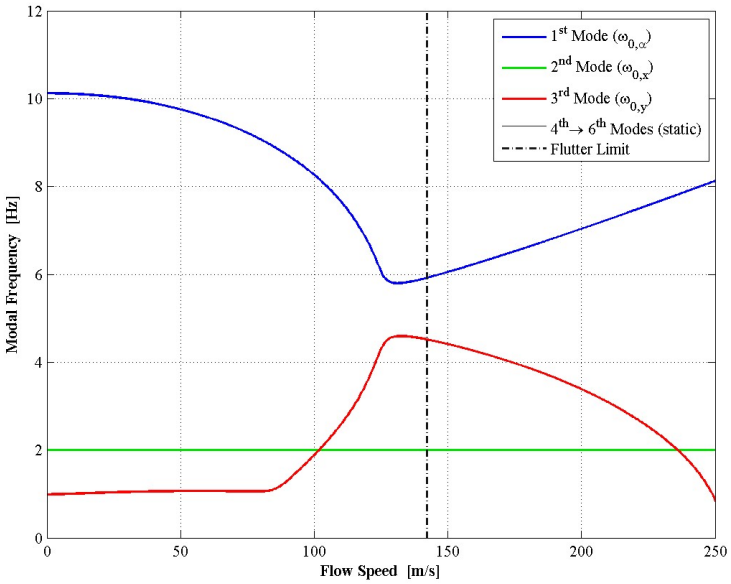

Figure 3.4: Modal frequencies vs. wind speed. Reference case structure, Risø B1-18 indicial response function, neglected camber. Flutter limit: 142.2 m/s, marked by dash-and-dot black line. The streamwise x degree of freedom do not show any coupling effects and influence on the other modes.

range. The third mode, which at zero wind speed is related to the heave dof, is the one responsible for flutter, in fact, at a wind speed of 142.2 m/s it turns unstable. A further comment on the same plot concerns the 'static modes', which are represented by the black full lines. One of them turn unstable at a wind speed of 207 m/s, and this corresponds to the divergence limit; also, the static modes have a null frequency parameter, so the definition of logarithmic damping does not apply, hence, the reported figures are simply the opposites of the eigenvalues real parts, that is to say that a unitary frequency is arbitrarily assigned to the static modes only for plotting purposes.

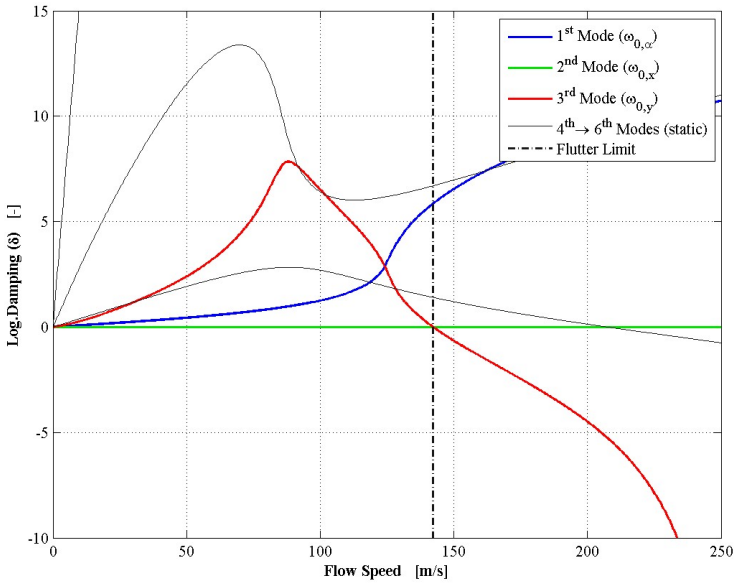

Figure 3.5: Modal damping vs. wind speed. Reference case structure, Risø B1-18 indicial response function, neglected camber. The streamwise x degree of freedom do not show any coupling effects and influence on the other modes. Flutter is given by the mode related to the heave degree of freedom (red line), that turns unstable at a wind speed of 142.2 m/s, dash-and-dot black line.

Finally, it can be concluded that, in case of non-cambered airfoil, the streamwise degree of freedom do not influence the dynamic of the other modes and hence it does not have any consequences on the stability limits. A confirm is also given by the analysis of the mode shapes, in fact, the mode with frequency corresponding to the x one (green lines in Fig.3.4 and 3.5) presents a modal shape with contribution from only the x dof, which is then null and constant in all the other modal shapes.

Influence for cambered airfoil

The camber of the airfoil profile is now taken into consideration and static coefficients different from zero are assigned to lift, drag and moment. The reference case is again given by a Risø B1-18 airfoil and the coefficients are retrieved from the airfoil static curves at zero angle of attack, Table 3.4; the same values are here maintained also when the system is linearized at a different pitch-torsion angle.

Parameter	*Symbol*	*Value*
Angle of Null Lift	$\alpha_{lift,0}$	-3.512
Lift Curve lin.coeff.	$\partial C_l/\partial\alpha$	2π
Drag Coeff. at 0^o	Cd_0	0.0074
Drag Curve lin.coeff.	$\partial C_d/\partial\alpha$	0
Moment Coeff. at 0^o	Cm_0	-0.112
Moment Curve lin.coeff.	$\partial C_d/\partial\alpha$	0

Table 3.4: Static aerodynamic coefficients for the cambered profile. From the static curves of Risø B1-18 airfoil. The linear coefficients are all computed at 0^o angle of attack.

For non-cambered airfoils it is shown in the previous section that the streamwise degree of freedom x and the corresponding mode are not affecting the stability of the system. In the cambered profile case, instead, the mode related to the x dof may become unstable and cause flutter for wind speeds that are below the limits previously computed; the flutter speed is hence now depending also on the x natural frequency, Figure 3.6. The mode related to the streamwise degree of freedom also shows stability regions: at certain frequency ratios, it turns unstable (dotted lines), but then at higher flow speeds it becomes stable again (circled line), so the system is also stable until flutter occurs in the other modes (black line). It is then observed that the mode related to the x dof, when unstable, has a modal damping that, although negative, is rather small. As a consequence, by applying a minor structural damping ($0.5 \sim 1\%$ logarithmic damping) in the streamwise dof, the mode is ensured stability.

The wind speed at which the other modes turn unstable is still equal to the non-cambered case, and is not influenced either by the streamwise frequency, either by the camber characteristics (Fig. 3.6).

In a non-cambered airfoil the stability limits are not depending on the steady state pitch angle $\alpha_{0,sts}$, with respect to which the system is linearized; but this is not the case when static coefficients different from zero are used to model the profile camber. In fact, the wind speed at which the mode related to the streamwise degree of freedom turns unstable, varies depending on the assigned steady state angle. Figure 3.7 reports the flutter speed as function of the steady state angle, again, a small structural damping suppresses the

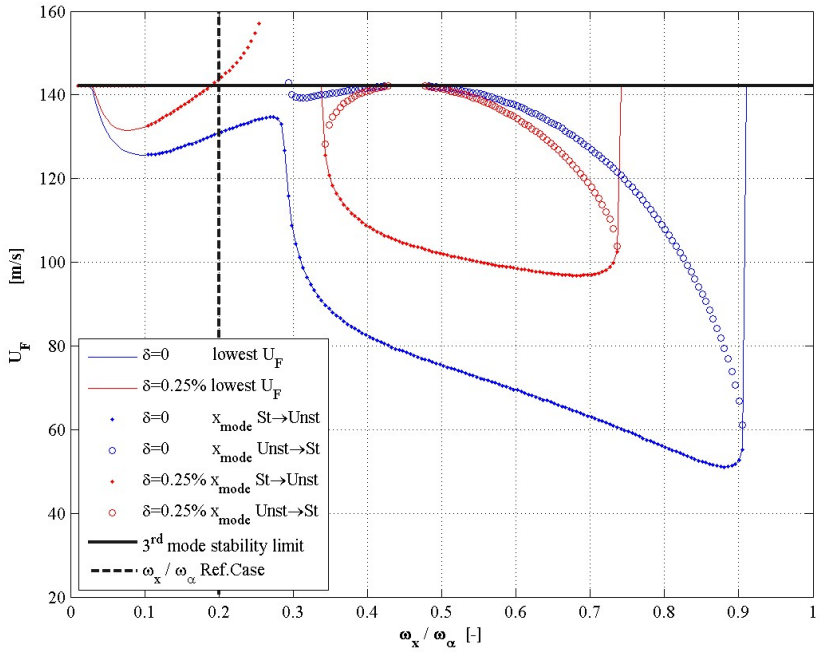

Figure 3.6: Flutter speed vs. streamwise-torsion frequency ratio, Risø B1-18 response and camber characteristics, null steady state pitch angle, reference case structural proprieties. The mode related to the streamwise degree of freedom can cause instabilities at lower wind speed than the other modes, but a small structural damping in the x dof is sufficient to suppress this instability. The wind speed at which one of the other modes turns unstable (black line) is not influenced either by the x frequency, either by the camber characteristics.

instability related to the x degree of freedom, and the stability limit reported for the other modes is not depending on the angle of pitch used to linearise the system.

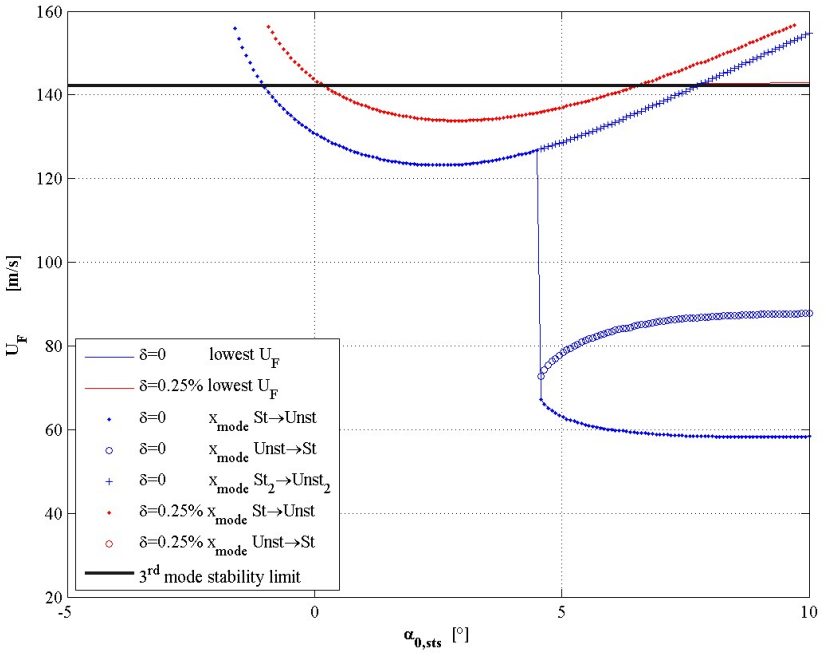

Figure 3.7: Flutter speed vs. steady state pitch angle $\alpha_{0,sts}$, Risø B1-18 response and camber characteristics, reference case structural proprieties. The mode related to the streamwise degree of freedom can cause instabilities at lower wind speed than the other modes, and the flutter speed depends on the steady state angle used to linearized the system. Again a small structural damping in the x dof is sufficient to suppress this instability. The wind speed at which one of the other modes turns unstable (black line) is not influenced by the steady state angle.

It can be hence concluded that, in a stability analysis, the movement of the section in the streamwise direction can be neglected in case of non-cambered airfoil profiles. Besides that, the same assumption can be also extended to cambered profile, where the effects of the streamwise degree of freedom on the stability limits are still negligible if a realistic structural damping applies in the same degree of freedom. Furthermore, it is also observed that, once the movements of the section in the streamwise direction are disregarded in the model, the stability limits are not any more depending either on the camber proprieties either on the steady state angle that is used to linearise the system.

Chapter 4

Undeformable airfoil. Summary of findings

A model to determine the aeroelastic stability of a 2D undeformable airfoil section is implemented, and is then validated by solving Theodorsen and Garrick's [22] problem for flexure-torsion flutter of a 2D wing section. The obtained stability curves are in good agreement with the results reported by more recent solutions of the same problem [26], whereas the original figures from Theodorsen and Garrick are found to be biased, probably due to errors related to the scarce computational power available at that time. The stability limits computed with the implemented eigenvalue linear approach are also in good agreement with the ones found by applying a non linear time marching solution.

Two different kind of airfoil sections have been investigated for stability, the first one describes a flat plate, which is also used in the validation case, while the second one consists in the same airfoil section on which the flap control will be afterwards applied. The numerical results are found to be very depending on the structural proprieties of the particular section, but some qualitative conclusions, presented in the following lines, can probably hold for a wider range of cases.

In both cases is in fact observed that the vorticity shed into the wake has a stabilizing effect that can not be neglected; the quasi-steady approximation of the indicial function of lift to unit is hence not applicable in stability analysis, since it would yield to greatly underestimated flutter limits. Furthermore, flutter limits different from the flat plate ones are obtained if the indicial function is tuned so to match the response of an airfoil with finite thickness. In this case, flutter would occur at slightly higher flow speeds, even though, in the investigated cases, the differences are rather small (less than 5 %). Concerning instead the non circulatory aerodynamic forces, the acceleration terms ($\ddot{\alpha}$ and $\ddot{y}$) contributions are found to have scarce influence, on the contrary, the stabilizing effect introduced by the pitch ratio

term $U\dot{\alpha}$ is of major importance.

The streamwise degree of freedom x is found to have no influence on the stability limits computed for non-cambered profiles, furthermore, even when the camber is taken into consideration, the effects are small and becomes negligible if a realistic structural damping is applied to that degree of freedom. Neglecting movements of the airfoil in the streamwise direction can be hence considered a valid assumption in this stability analysis, yielding thus a simplified linear formulation in the aerodynamic model.

To conclude, the analysis of the undeformable airfoil section produces a convenient background for the following investigation of the deformable trailing edge case, both in means of numerical results to use as comparison, and as background for the approximation of negligible movements in the streamwise degree of freedom.

Part II

Flap equipped airfoil

Chapter 5

Model and method

In this second part of the work, a trailing edge flap is applied on the 2D airfoil section. The flap allows to rapidly modify the aerodynamic forces acting on the airfoil, and it can be controlled so to reduce the blade fatigue loads [4, 8]. The focus of the current investigation is to assess how the presence of the controlled flap may affect the stability limits of the airfoil section.

As mentioned in the introduction, the flap is not intended as a classic plain flap that rigidly rotates around its hinge point, but, on the contrary, is represented by a continuous and smooth deformation of the airfoil trailing edge part, specified through a non linear deflection shape.

To asses the stability of the flap equipped airfoil an aero-servo-elastic model is implemented. The model comprises structural ('elastic'), aerodynamic ('aero') and control ('servo') parts, all interacting and coupled among them. The structural behaviour is described by three equations of motion, one for each degree of freedom (dof) of the structure. The first degree of freedom is simply a rigid translation in the heave direction, while the second is a rigid body rotation around the elastic axes that gives the airfoil angle of pitch. The deformation of the airfoil aft part induced by the flap deflection is represented by the third degree of freedom, using a mode shape added to the camberline. The movements in the streamwise direction are neglected, since, as concluded in the undeformable airfoil analysis, their influence on stability is of scarce importance.

The aerodynamic part determines the forces that originates from the interaction of the airfoil with the flow, Gaunaa's [9] potential flow model for the aerodynamic forces on a thin airfoil undergoing arbitrary motion and deformation is employed. Concerning the control part, the actuator is modelled as an extra elastic term in the flap equation of motion, and the desired flap deflection is determined according to different control algorithms.

An eigenvalue approach is then used to investigate the stability of the system, and, since the equations are now linear in the system state variables,

the analysis applies directly to the full aeroservoelastic system of equations, represented in a state-space matrix formulation. The same system is then also solved with a time marching integration, so to verify the results obtained in the eigen-analysis. A further validation of the model for the uncontrolled elastic flap is obtained by comparison with analogous cases reported in literature.

In the following sections each part of the model is presented, while the numerical results are reported and discussed in the following chapter.

5.1 Structural model

5.1.1 Reference system

The local reference system is the same described in the rigid undeformable airfoil case (section 2.1.1) it extends along the chord and is normalized with respect to half chord length b_{hc}, thus its dimensionless coordinates ε ranges from -1 at the leading edge to $+1$ at the trailing edge. The deformable part of the airfoil extends from a point that, in analogy to the 'classic' plain flap case, is referred to as *hinge point* and has the dimensionless coordinate ε_{fl}^{hp}. As in the previous studies [8], the flap length is 10% of the chord, the hinge is hence located in the point $\varepsilon_{fl}^{hp} = 0.8$.

The motion and deflection of the flap equipped airfoil are described by three degrees of freedom (Figure 5.1): y for the rigid body translation in the heave direction, α for the rigid rotation that describes the airfoil pitch-torsion and β to represent the flap deflection. As concluded in the rigid undeformable airfoil analysis, chapter 4, the streamwise degree of freedom x has a scarce influence on the stability of the system and is therefore neglected in this investigation. The heave coordinate y is positive upwards, and both the pitch α and flap β coordinates are considered positive in clockwise direction, resulting in positive motions when the airfoil pitches nose up and the flap deflects downward.

The deflection of the trailing edge flap is described by means of a deformation mode shape u_{fl}, which defines the shape of the flap by describing the position of the deformed airfoil camberline when a unit deflection coordinate β is assumed. The mode shape is thus only function of the chordwise position ε. In this investigations, as in Buhl et al. [8], the flap extends for a length of 10 % of the chord and its mode shape is the one that Troldborg's [24] CFD investigations returns as optimal.

The deflection shape u_{fl} (blue line in Figure 5.2) is curved, giving a smooth trailing edge deformation, which yields to better aerodynamic performances when compared to a 'classic' rigid and linear flap. The mode shape is then scaled so that the coordinate β corresponds, for small deflection, to the angle between the undeformed camberline and the line connecting the deformed trailing edge position to the hinge point (red line in Figure

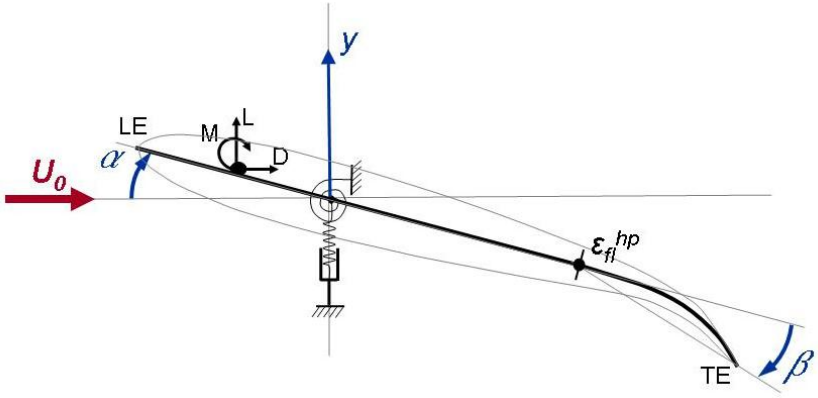

Figure 5.1: Global reference system used to define the airfoil motion. Degrees of freedom: heaving y positive upwards, pitching α positive nose up, flap deflection β positive flap downwards.

5.2), a unit value of the β coordinate corresponds to an angle of 1 degree.

5.1.2 Equations of motion

The equations of motion for rigid body translation in the heave coordinate and rotation are similar to the ones used in the undeformable airfoil model, section 2.1.3, with the addition of the inertial terms linked to the flap deflection. In the assumption of small pitch angle α, using the same notation as Gaunaa's [9], they read:

$$m_{tot}\ddot{y} - S_\alpha\ddot{\alpha} + b_{hc}Ins_{fl}\,\ddot{\beta} + c_y\dot{y} + k_y y = L_{aed}, \quad (5.1)$$

$$-S_\alpha\ddot{y} + I_{ea}\ddot{\alpha} + (\varepsilon_{ea}b_{hc}^2 Ins_{fl} - b_{hc}^2 Ims_{fl})\,\ddot{\beta} + c_\alpha\dot{\alpha} + k_\alpha\alpha = M_{aed}. \quad (5.2)$$

Where most of the terms are the same as defined in the undeformable airfoil part, with the exception of Ins_{fl} and Ims_{fl}, which give the inertial couplings of the flap deflection. The two terms describe in fact the virtual work done by the inertial forces generated by unit acceleration in, respectively, the heave and the pitch degrees of freedom; the displacement for the virtual work is given by the deflection mode shape. The terms are hence computed as chordwise integral functions of the deflection shape u_{fl}, the unit-span mass distribution ρ^{2D} and the chord dimensionless coordinate ε [9]:

$$Ins_{fl} = \int_{-1}^{1} u_{fl}\,\rho^{2D}\,\mathrm{d}\varepsilon, \quad (5.3)$$

$$Ims_{fl} = \int_{-1}^{1} u_{fl}\,\rho^{2D}\,\varepsilon\,\mathrm{d}\varepsilon. \quad (5.4)$$

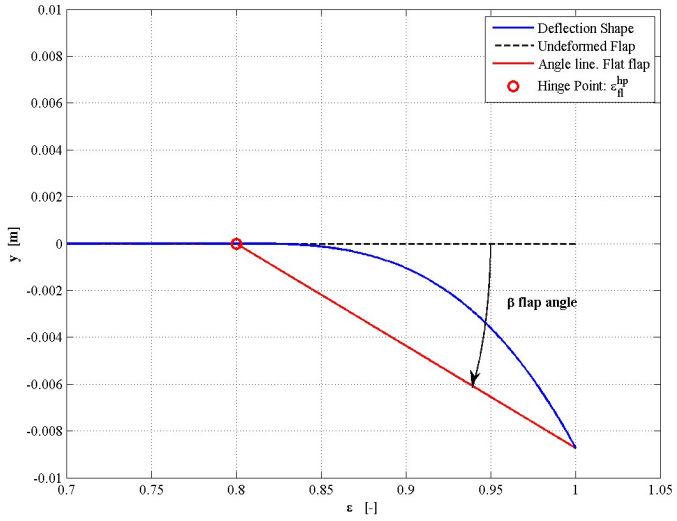

Figure 5.2: Flap Deflection mode shape u_{fl}. The trailing edge deformation is smooth, $\beta = 1$ results in 1° angle between the trailing edge-hinge point line and the undeformed camberline. The plot shows camberline deflection corresponding to $\beta = 5°$.

Since they are constant, as far as the deflection mode shape or the mass distribution are not modified, they can be computed only once before the simulation and stored.

The deformation induced by the flap is modelled by using the preassigned deflection mode shape, and the respective equation of motion is thus defined following a generalized coordinates approach, according to which the equilibrium between inertial, elastic, damping and aerodynamic forces is found in terms of virtual works, where the displacement is given by the deflection mode shape.

The action of the controller on the flap is instead modelled as an extra elastic term in the equation of motion, so that the elastic force is proportional to the difference between the flap actual deflection β and the deflection required by the control actuator β_{ctrl}. In other words, if no external (aerodynamic) forces are acting on the flap, the controller elastic term modifies the flap equilibrium position from no deflection to a deflection equal to β_{ctrl}.

Finally, the equation of motion for the elastic controlled flap, undergoing inertial, damping and aerodynamic forces is:

$$b_{hc} Ins_{fl}\, \ddot{y} + (\varepsilon_{ea} b_{hc}^2 Ins_{fl} - b_{hc}^2 Ims_{fl})\, \ddot{\alpha} + m_{mod}\, \ddot{\beta} + c_{fl}\, \dot{\beta} + k_{fl}\, (\beta - \beta_{ctrl}) \;=\; GF_{aed}, \tag{5.5}$$

where, m_{mod} is the modal mass of the flap deflection mode shape, and it is

computed from the chordwise integral:

$$m_{mod} = \int_{-1}^{1} u_{fl} \rho^{2D} u_{fl} \, \mathrm{d}\varepsilon. \tag{5.6}$$

The stiffness of the flap is given by the natural frequency ω_{fl} of the deflection mode shape: $k_{fl} = m_{mod} \, \omega_{fl}^2$; while the viscous damping coefficient is computed as $c_{fl} = 2 m_{mod} \omega_{fl} \xi_{fl}$.

The effect of the aerodynamic forces on the flap is given in terms of the generalized force GF_{aed}, which corresponds to the virtual work done by a force originated from the pressure difference between the suction and pressure sides of the airfoil, displaced according to the deflection shape, everything integrated along the chord:

$$GF_{aed} = \int_{-1}^{1} u_{fl} \Delta P \, \mathrm{d}\varepsilon. \tag{5.7}$$

The structural behaviour of the airfoil is now fully described by the three second order differential equations of motion: equation (5.1) for the heave degree of freedom, eq. (5.2) for the pitch and eq. (5.5) for the trailing edge flap deformation. The terms related to the aerodynamic effects L_{aed}, M_{aed}, GF_{aed} and the control actuator β_{ctrl} will be defined in the following sections.

5.2 Aerodynamic model

The model used to describe the unsteady aerodynamic behaviour of the flap equipped airfoil, developed by Gaunaa [9], allows to compute the aerodynamic forces and their distribution for a 2D airfoil undergoing arbitrary motion and deformation of the camberline. Furthermore, the model has a linear state-space formulation that makes it computationally efficient and suitable for stability analysis.

Two main assumptions underlie the formulation: thin airfoil and potential flow. The former assumption implies that the airfoil is represented by its camberline, that is to say, that the thickness is neglected and the airfoil position, motion and deformation are only given by the camberline points. Furthermore, the validity of the model is limited to potential flow condition: the airfoil interacts with an incompressible and inviscid fluid, and the flow is fully attached. Flow separation and stall are not included in the model and hence the validity range is restricted to small flap deflections and angles of attack, which is anyway a realistic condition for an airfoil mounted on a pitch regulated turbine. In addition, in the present investigation, the airfoil camberline is assumed to move only in the heave direction since the streamwise x degree of freedom is neglected.

Under this assumptions, the pressure difference between the suction and

pressure sides of the airfoil is determined from the velocity potential field and aerodynamic forces and pitching moment are then found by integrating the pressure differences along the chord. The process involves integral of functions of the deflection mode shape and its slope, the integrals are rather complex but, since the deflection shape is not time dependent, they can be computed once with numerical methods and then stored.

As in the undeformable airfoil case, section 2.2, the aerodynamic forces can be split into a non-circulatory and a circulatory contribution. The non circulatory forces depend on the added mass terms, and hence only on the instantaneous motion of the airfoil. On the contrary, wake memory effects are involved in the circulatory contributions, and they are modelled by the term w_{eff}.

The term w_{eff} represents in fact an equivalent effective downwash speed at the three-quarter chord that takes into account the time lag effects caused by the vorticity shed into the wake. Similarly to the effective angle of attack for the undeformable airfoil model (2.2.4), it is computed using an indicial response function approximation; the expression for w_{eff} involves the quasi-steady equivalent downwash speed $w_{3/4}$ and a number n_{lag} of additional aerodynamic state variables, which are determined from n_{lag} first order differential equations added to the system.

The indicial response function, used in this part of the investigation, is the three terms ($n_{lag} = 3$) one, that is tuned to match the step response of the Risø B1-18 airfoil (section 2.2.4), the corresponding numerical values for the A_i and b_i coefficients are given in Buhl et al. [8], and also reported here in table 2.1, page 20.

A more detailed description of the aerodynamic model is given in Gaunaa's report [9], and, by adapting the model to the present investigation case, the expressions for the unsteady lift force L_{aed}, the pitching moment M_{aed} and the flap deflection generalized forces GF_{aed} simplifies to:

$$\begin{aligned} L_{aed} = {} & \rho b_{hc}^2 \pi U_0 \ \dot{\alpha} + \rho b_{hc}^2 \frac{1}{\pi} U_0 F_{dydx,LE} \ \dot{\beta} \\ & - \rho b_{hc}^2 \pi \ \ddot{y} - \rho b_{hc}^3 \pi \varepsilon_{ea} \ \ddot{\alpha} + \rho b_{hc}^2 \frac{1}{\pi} F_{y,LE} \ \ddot{\beta} \\ & + 2\rho b_{hc} \pi U_0 \ w_{eff}, \end{aligned} \tag{5.8}$$

$$\begin{aligned} M_{aed} = {} & \rho b_{hc}^2 U_0^2 \left(\frac{1}{\pi} F_{dydx,LE} + \frac{1}{2} H_{dydx} \right) \ \beta \\ & + \rho b_{hc}^3 \pi U_0 (0.5 - \varepsilon_{ea}) \ \dot{\alpha} \\ & + \rho b_{hc}^2 U_0 \left(-\frac{b_{hc}}{\pi} G_{dydx,LE} + \frac{b_{hc}}{\pi} \varepsilon_{ea} F_{dydx,LE} + \frac{1}{\pi} F_{y,LE} + \frac{1}{2} H_y \right) \ \dot{\beta} \\ & - \rho b_{hc}^3 \pi \varepsilon_{ea} \ \ddot{y} - \rho b_{hc}^4 \pi \left(1/8 + \varepsilon_{ea}^2 \right) \ \ddot{\alpha} - \rho b_{hc}^3 \frac{1}{\pi} (G_{y,LE} - \varepsilon_{ea} F_{y,LE}) \ \ddot{\beta} \\ & + 2\rho b_{hc}^2 \pi U_0 (0.5 + \varepsilon_{ea}) \ w_{eff}, \end{aligned} \tag{5.9}$$

$$
\begin{aligned}
GF_{aed} = {} & \rho b_{hc} \frac{1}{\pi} U_0^2 (PI_8 - H_{dydx} PI_7)\ \beta \\
& + \rho b_{hc}^2 U_0 (2PI_1 - PI_6)\ \dot{\alpha} + \rho b_{hc} \frac{1}{\pi} U_0 (b_{hc} PI_3 - H_y PI_7 + PI_9)\ \dot{\beta} \\
& - 2\rho b_{hc}^2 PI_1\ \ddot{y} + \rho b_{hc}^3 (-2\varepsilon_{ea} PI_1 + PI_4)\ \ddot{\alpha} + \rho b_{hc}^2 \frac{1}{\pi} PI_2\ \ddot{\beta} \\
& - 2\rho b_{hc} U_0 PI_5\ w_{eff}.
\end{aligned} \tag{5.10}
$$

Where the PI_n, $F_{...}$, $f_{...}$, $G_{...}$, $H_{...}$ terms are the integrals of the deflection mode shape functions that have been computed in numerical way and stored, their expressions are also given in [9].

The effective equivalent downwash speed w_{eff} that takes into account the unsteady wake effects is computed using an indicial response function approximation (section 2.2.4), and in case of a three terms approximation, it reads

$$
w_{eff} = w_{3/4}(1 - A_1 - A_2 - A_3)\ + z_1 + z_2 + z_3. \tag{5.11}
$$

Where $w_{3/4}$ is the quasi-steady equivalent downwash speed at the three quarter chord point,

$$
\begin{aligned}
w_{3/4} = {} & U_0\ \alpha - \frac{1}{2\pi} U_0 H_{dydx}\ \beta \\
& - \ \dot{y} + b_{hc}(0.5 - \varepsilon_{ea})\ \dot{\alpha} - \frac{1}{2\pi} H_y\ \dot{\beta}.
\end{aligned} \tag{5.12}
$$

The z_i terms are additional aerodynamic state variables that represent the time lag effects of the vorticity shed in to the wake (section 2.2.4), and they are obtained from three first order differential equations, which are added to the system:

$$
\dot{z}_i = -\frac{1}{b_{hc}} U_0 b_i\ z_i + \frac{1}{b_{hc}} U_0 b_i A_i\ w_{3/4}. \tag{5.13}
$$

The A_i and b_i terms in equations (5.11) and (5.13) are the coefficients that defines the indicial response function and for the considered case of the Risø B1-18 airfoil profile.

The aerodynamic model determines also the pressure difference between suction and pressure sides of the airfoil for a specified point ε_p along the chord, the difference is then used as input for one of the flap control algorithms.

The pressure difference in an arbitrary point ε_p is determined as

$$\begin{aligned}\Delta P(\varepsilon_p) = &-\rho\frac{1}{\pi}U_0^2\left(\frac{\varepsilon_p}{\sqrt{1-\varepsilon_p^2}}H_{dydx} - \partial f_{dydx,\varepsilon_p}\right)\ \beta \\ &+ \rho b_{hc}U_0\left(2\sqrt{1-\varepsilon_p^2} + \frac{(2\varepsilon_p+1)(1-\varepsilon_p)}{\sqrt{1-\varepsilon_p^2}}\right)\ \dot{\alpha} \\ &+ \rho\frac{1}{\pi}U_0\left(b_{hc}f_{dydx,\varepsilon_p} - \frac{\varepsilon_p}{\sqrt{1-\varepsilon_p^2}}H_y + \partial f_{y,\varepsilon_p}\right)\ \dot{\beta} \\ &- 2\rho b_{hc}\sqrt{1-\varepsilon_p^2}\ \ddot{y} + \rho b_{hc}^2\sqrt{1-\varepsilon_p^2}\,(-2\varepsilon_{ea}+\varepsilon_p)\ \ddot{\alpha} + \rho b_{hc}\frac{1}{\pi}f_{y,\varepsilon_p}\ \ddot{\beta} \\ &- 2\rho U_0\frac{\varepsilon_p - 1}{\sqrt{1-\varepsilon_p^2}}\ w_{eff}. \end{aligned} \tag{5.14}$$

where the integral functions $f_{\ldots,\varepsilon_p}$ are also evaluated in the point of interest ε_p; their expressions are given in Gaunaa [9].

The aerodynamic model yields to a set of expressions that are all linear in the system state variables it is thus possible to cast the equations of motion, coupled with the aerodynamic expressions, in a linear state-space formulation.

5.3 Control system model

The control system can be described as a logic block, where the input is a set of measurements that describe the state of the aeroelastic system. The output of the control system is an angle β_{ctrl} (Figure 5.3) that, by changing the deflection of the flap actuator, modifies the condition of the same aeroelastic system, so that a different state is reached, resulting in new measurements and thus a new control output, and so on.

The full control system block can be then ideally split in two smaller operation blocks (Figure 5.3), the first one contains the *control algorithm*, the second, the *time lag* part. The control algorithm is a function that relates the inputs from the aeroelastic system to the deflection angle β_{set} that is expected to produce the desired changes in the system. Whereas, the second block describes all the time lag that may affect the control system, from the acquisition of the sensor inputs to the elaboration of the output. In mathematical terms, the time lag corresponds to a function that transforms the desired β_{set} to the deflection angle β_{ctrl} that actually controls the flap actuator.

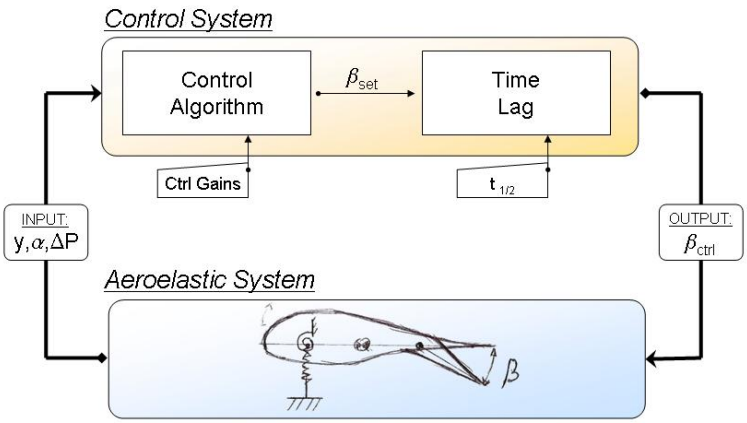

Figure 5.3: Control system logic 'blocks'. The *input* to the control system is a set of variables describing the state of the aeroelastic system. The input is first processed by the *control algorithm* block that returns the desired flap deflection β_{set}, the second *time lag* block models the delay in the control. The control system *output* is the deflection angle β_{ctrl}, that actuates the flap in the aeroelastic system.

5.3.1 Control algorithms

In the previous studies, two controls algorithms were found to be particularly effective in achieving good level of load reduction [8]. The first one is a proportional differential control, based on measurements of the heave displacement y and its time derivative $\dot{y}$, while the second one is proportional to the local angle of attack α. Both controls are implemented in the current model and their gain values, at basic reference conditions, are equal to the ones that in Buhl [8] return the higher load alleviation, for a turbulent wind flow with a total relative speed close to 60 m/s.

In addition, a third control strategy is introduced, and it employs as input measurements of the pressure difference between the suction and the pressure side of the airfoil. Two different location for the pressure tap sensors are investigated, and control gains are assigned with a simple Ziegler-Nichols' tuning.

Heave displacement control algorithm

The y control algorithm describes a proportional differential control and, as in [8], the relation between the measured input and the angle output, can be expressed by the function,

$$\beta_{set} = A_y y + B_y \dot{y} - A_y y_I. \tag{5.15}$$

The terms A_y and B_y are, respectively, the proportional and differential gain parameters, in the baseline reference case they have the values, reported in

table 5.1, that in Buhl et al. [8] return the highest load alleviation.

The term y_I is the heave displacement running mean, computed by integration over a ΔT window. Since the current analysis is focused on stability, the variations of the aeroelastic state can be assumed to be fast and, thus, on a much smaller time scale than the amplitude ΔT of the integration window. As a consequence, the integral terms can be considered constant, and thus neglected in stability analysis. The function that expresses the control algorithm is hence linear in y and $\dot{y}$.

Angle of attack control algorithm

The control algorithm based on measurement of the local angle of attack is implemented by considering that, in steady state condition, the flap deflection should compensate for changes in the angle of attack, so to maintain constant the lift coefficient C_L. In fact, in steady condition, for inviscid incompressible flow, the variations on the lift depends only on the angle of attack α and the flap deflection β, Eq.(5.8), the variations in the dimensionless steady lift coefficient C_L, can be hence computed as

$$\Delta C_L = 2\pi \cdot \alpha - H_{dydx} \cdot \beta. \tag{5.16}$$

Where, 2π is the linear static lift coefficient for a flat plate $\frac{\partial C_L}{\partial \alpha}$. Similarly, the term $-H_{dydx}$ is the analogous slope for the static lift curve versus flap deflection, $\frac{\partial C_L}{\partial \beta}$ and is given by integrals of the deflection shape along the section chord, as presented in [9].

The output of the control algorithm is then the flap deflection that compensates for the measured variation in the angle of attack, yielding to

$$\beta_{set} = A_\alpha \frac{2\pi}{H_{dydx}} \alpha - A_\alpha \frac{2\pi}{H_{dydx}} \alpha_I + A_\alpha \beta_I. \tag{5.17}$$

As already mentioned, all the integral terms, denoted by the subscript $_I$, are assumed to be constant, the equation is hence a linear function of the angle of attack, here equal to the torsional pitch angle α. The control gain factor A_α, in the baseline reference case is equal to one (Table 5.1), so to completely compensate for the variations in the steady case.

Pressure difference control algorithm

The main interest in investigating a controller based on measurements of the pressure difference between the sides of the airfoil, lies in the fact that this kind of system would be able to operate with more simple sensor set-ups. In fact, the input to the controller can be provided by pressure taps embedded in the airfoil, without requiring more complex devices as leading edge Pitot's tubes for the angle of attack or optical measurements to assess the heave

displacement.

To reduce the lift fluctuations, the control strategy consists in operating the flap so to maintain a constant pressure difference in the measurement point. In analogy to the α control, the algorithm is developed assuming a steady state aerodynamic, in fact, in this condition, the equation for the pressure difference along the airfoil (5.14) reduces to a more simple function of the angle of attack α, the deflection angle β, the dimensionless chord position ε and the wind speed U_0. The pressure difference can be then normalized by the flow dynamic pressure, yielding to the dimensionless coefficient C_P, which, in steady condition, can be expressed as a linear combination of α and β, and the terms $\frac{\partial C_P}{\partial \alpha}$ $\frac{\partial C_P}{\partial \beta}$, which are both non linear functions of the chordwise position ε:

$$\begin{aligned} C_P = \frac{\Delta P}{0.5\rho U_0^2} = \\ = \left.\frac{\partial C_P}{\partial \alpha}\right|_\varepsilon \cdot \alpha + \left.\frac{\partial C_P}{\partial \beta}\right|_\varepsilon \cdot \beta = \\ = -4\frac{\varepsilon - 1}{\sqrt{1-\varepsilon^2}} \cdot \alpha + \frac{2}{\pi}\left(\partial f_{dydx} - \frac{H_{dydx}}{\sqrt{1-\varepsilon^2}}\right) \cdot \beta. \end{aligned} \tag{5.18}$$

The term ∂f_{dydx} is also function of ε and represents a derivative along the chord of an integral function of the deflection shape, as in Gaunaa [9].

The control algorithm is then obtained by imposing the condition that the flap deflection compensates the unbalance between the actual pressure difference ΔP and the desired equilibrium one ΔP^{eq}, resulting in the equation

$$\begin{aligned} \frac{\Delta P - \Delta P^{eq}}{0.5\rho U_0^2} = -A_{\Delta p} \left.\frac{\partial C_P}{\partial \beta}\right|_\varepsilon (\beta_{set} - \beta^{eq}) \Longrightarrow \\ \beta_{set} = -A_{\Delta p} \frac{1}{\partial C_P/\partial \beta \cdot (0.5\rho U_0^2)} \cdot \Delta P + (\ldots)^{eq}. \end{aligned} \tag{5.19}$$

As in the previous algorithms, all the terms that refer to an equilibrium state $(\ldots)^{eq}$ are computed by moving mean integrals, and, within the assumption of fast variations compared to the integration window, they can be considered constant, and hence without any effect on the stability. As a consequence, since the pressure difference (5.14) is a linear function of the aeroelastic state variables, the control algorithm is also linear.

A part from that, the pressure difference measured by the sensors is normalized with respect to the dynamic pressure, consequently, also the wind speed U_0 should be known, and it can be considered as a factor that variates the control gain. An additional gain factor $A_{\Delta P}$ is also introduced to better tune the response of the algorithm, and, as described in the following paragraph, its value is assigned by applying a simple Ziegler-Nichols'

method.

The control tries to reduce the fluctuations in the pressure difference measured at one specific point, the relation that links the static pressure difference to the static lift force is then different depending on where, along the chord, the measurements are taken. In the actual investigation, two points are taken into consideration as possible locations for the pressure taps and a different pressure control algorithm is defined in each of the two points.

The first point ε_{cnst} is characterized by the fact that, in steady conditions, the ratio between lift coefficients C_L and pressure coefficient $C_P\varepsilon_{cnst}$ is constant for every angle of attack α and flap β, when evaluated in this point. For the considered airfoil section and flap deformation shape, the point is located near to the half chord $\varepsilon_{cnst} = -0.029$, Appendix C reports the steady state investigation that justifies the point specific location.

The second point ($\varepsilon_{10\%}$) is located at 10% chord distance from the leading edge and its position is simply the results of a trial and error procedure. In fact, the unsteady pressure distribution is investigated for the airfoil undergoing assigned oscillations, it is thus found that the ratio between the unsteady lift and the pressure coefficient measured in proximity of the 10% point, even though not constant, shows less violent oscillations than in other locations. Consequently, while the ε_{cnst} position appears as optimal according to a static analysis, the $\varepsilon_{10\%}$ location actually seems more convenient when dynamic effects are taken into account.[1]

Ziegler-Nichols tuning The gain factors used in the y and α control algorithms are the ones that, in Buhl et al. [8], corresponds to an optimal load alleviation efficiency. In the case of the pressure control, at the time writing an optimal gain for load reduction is not yet available, and the gain factors are hence tuned with a simple Ziegler-Nichols method for proportional controller [20].

The method is implemented by using a time marching solution of the aero-servo-elastic system, the structure of the airfoil is the baseline reference one, as it will be defined in the following chapter (Table 6.2, page 64), and the flow speed is set to 60 m/s, in analogy with [8]. Simulations are carried out for each of the two pressure control algorithms, the gain factor $A_{\Delta P}$ are progressively increased until they reach their critical values A^{cr} for which the system starts to be unstable. The obtained critical gain factors are: 0.26 for pressure taps located at $\varepsilon_{10\%}$, and 1.12 for ε_{cnst}. According to the Ziegler-Nichols method, the gain assigned to the control algorithm are half the critical ones, yielding, in the two cases, to $A_{\Delta P}\varepsilon_{10\%} = 0.13$ and

[1] The load alleviation potential achievable by controlling the flap with pressure difference measurements is a very recent issue, which requires deeper investigation. A study in this sense is currently being carried out by Andersen [5].

$A_{\Delta P}\varepsilon_{cnst} = 0.56$. The gain factors corresponding to the baseline reference case of each control algorithm are all collected in Table 5.1.

Type of Control	*Gain Symbol*	*Gain factor*
y, prop. term	A_y	-500
y, deriv. term	B_y	-25
α, prop.	A_α	1
ΔP, at $\varepsilon_{10\%}$	$A_{\Delta P}^{\varepsilon,10\%}$	0.13
ΔP, at ε_{cnst}	$A_{\Delta P}^{\varepsilon,cnst}$	0.56

Table 5.1: Gain factors corresponding to the baseline reference case for each control algorithm. The y and α gains corresponds to the highest load reduction in Buhl et al. [8]. The ΔP gains are obtained by Ziegler-Nichols tuning.

5.3.2 Time lag

The time lag part of the control system models the delay that affects all the control operation, from the sensors to the actuator. In fact, if time delay is considered in the model and a step change occurs in the measured states, the control output β_{ctrl} does not react immediately to the change, but it lags behind the new value β_{set}, corresponding to the new state, and it converges to β_{set} only as the time goes to infinity. In mathematical terms the control delay is represented by a function that relates the output of the control algorithm β_{set} to the variable β_{ctrl} that controls the flap actuator.

In the ideal condition of a control system without any time lag, the response of the control output to steps in the input is immediate, and hence the delay function simply reduces to the equation

$$\beta_{ctrl} = \beta_{set}. \tag{5.20}$$

As a consequence, the linear expressions for β_{set} defined for each control algorithm (Section 5.3.1) can be directly substituted in the elastic term of the flap equation of motion (5.5), resulting again in a linear combination of aeroelastic state variables.

If the system is instead affected by control delay, the time lag is modelled as a first order filter, as in Gaunaa [10], the delay function is then a first order differential equation :

$$\dot{\beta}_{ctrl} = \frac{\ln(0.5)}{t_{1/2}}\beta_{ctrl} - \frac{\ln(0.5)}{t_{1/2}}\beta_{set}, \tag{5.21}$$

where $t_{1/2}$, reaction half time, represents the control lag in terms of the time required by the control output β_{ctrl} to reach half of its final value β_{set}. Besides, this formulation can not model the null time lag condition, since that would cause equation (5.21) to become infinitely stiff.

The time lag differential equation (5.21) is an extra equation added to the aeroservoelastic system, and, as well as that, its variable β_{ctrl} is also included in the vector of the system state variables and is then inserted in the elastic term of the flap equation of motion (5.5). As in the case without lag, β_{set} is simply a linear combination of state variables as given by the control algorithms, hence the time lag differential equation (5.21) is also linear.

5.4 Aeroservoelastic system

As mentioned in the previous sections, all the equations describing the aeroservoelastic system are linear in the system variables. The full set of equation can be hence written in matrix form as

$$\boldsymbol{M^*}\underline{\ddot{\boldsymbol{x}}}^* \; + \; \boldsymbol{C^*}\underline{\dot{\boldsymbol{x}}}^* \; + \; \boldsymbol{K^*}\underline{\boldsymbol{x}}^* = \underline{\boldsymbol{f_0}}^*, \tag{5.22}$$

and, by introducing a variable substitution for the second order derivatives of the structural variables, the set of equations can be then directly represented in a linear state-space formulation as a first order matrix equation:

$$\boldsymbol{M}\underline{\dot{\boldsymbol{x}}} = \boldsymbol{A}\underline{\boldsymbol{x}} + \underline{\boldsymbol{f_0}}. \tag{5.23}$$

Where the vector $\underline{\boldsymbol{x}}$ collects all the aerodynamic, control and structural variables; in a general case of three terms indicial response approximation and controller with time lag, the system would involve 10 first order differential equations: 3 for variable substitution, 3 equations of motion, 3 aerodynamic state equations and 1 for the control time lag model; the system variables vector could be hence organized as

$$\underline{\boldsymbol{x}} = \left\{\dot{y}, \dot{\alpha}, \dot{\beta}, y, \alpha, \beta, z_1, z_2, z_3, \beta_{ctrl}\right\}. \tag{5.24}$$

5.4.1 Time and frequency domain solutions

As in the rigid undeformable airfoil part (section 2.3.1), the system of equations is solved in the time domain by applying a numerical time marching integration based on the ordinary differential equation solver *ode45*, in Matlab. Initial conditions are assigned so to represent a steady state close to the equilibrium one, and the resulting time histories for the system variables $\underline{\boldsymbol{x}}_{(t)}$ indicate if the state of the system is stable or not, so to verify the solution obtained with the eigenvalue approach.

The stability analysis is carried out also in the frequency domain, as presented in the undeformable airfoil case, section 2.3.2. In this case, though, the system of equations is already linear, the generalized eigenvalue problem

can be hence formulated directly from eq.(5.23),

$$(\boldsymbol{A} - \lambda \boldsymbol{M})\ \underline{\boldsymbol{\phi}} = \underline{\mathbf{0}}. \tag{5.25}$$

The resulting eigenvalues λ convey information about the frequency of the system mode ($\mathrm{Im}(\lambda)$) and their stability ($\mathrm{Re}(\lambda)$), the analysis is then carried out in the same way that was presented for the undeformable airfoil (Section 2.3.2).

5.5 Static aeroelasticity: control reversal

The presence of the trailing edge flap on an elastically supported airfoil may give rise to a static aeroelastic phenomenon known as *control reversal* [7]. In fact, a deflection of the flap, for instance downward, originates not only a change in lift, normally an increase, but also a nose down pitching moment that decreases the angle of attack. The pitching moment increases with the square of the wind speed while the counteracting elastic torque from the spring of stiffness k_α is constant. Thus, as the wind speed increases, the gain in lift given by the flap downward deflection becomes lower due to the simultaneous decrease in the angle of attack (loss of control efficiency). For a flow speed equal to the reversal one, the flap has no effects on the lift, since every variation would be counterbalanced by an equivalent change in the angle of attack; if the wind speed is then higher, the flap effect is *reversed*: a downward deflection now decreases the lift.

The control reversal is a static phenomenon that only depends on the equilibrium between the flap and the structure pitching moments, the *reversal speed* can be hence predicted analytically, as

$$U_{Rev} = \sqrt{\frac{-\frac{\partial C_L}{\partial \beta} k_\alpha}{2\rho b_{hc}^2 (2\pi) \frac{\partial C_M}{\partial \beta}}}. \tag{5.26}$$

Where $\partial C_L/\partial\beta$ is the change in the static lift coefficient due to a unit change in the flap deflection coordinate β and $\partial C_M/\partial\beta$ is the analogous change in the static pitching moment. Their values can be computed from the lift (5.8) and moment (5.9) equations, simplified by assuming steady state conditions:

$$\begin{aligned} \frac{\partial C_L}{\partial \beta} &= -H_{dydx}, \\ \frac{\partial C_M}{\partial \beta} &= \frac{1}{2\pi} F_{dydx,LE} + \frac{1}{4} H_{dydx}. \end{aligned} \tag{5.27}$$

For the basic reference airfoil section, with a curved 10% chord flap and a

torsional frequency of 10 Hz the reversal speed is found to be

$$U_{Rev} = 95.5 \quad m/s.$$

Chapter 6

Flap equipped airfoil. Results and discussion

A tool to investigate the aeroservoelastic stability of an airfoil section with flap is implemented according to the model described in the previous chapter. At first, the control part of the model is not considered and the tool is validated by comparison with a reimplementation of the case presented by Theodorsen and Garrick [22] for a three degrees of freedom flutter of a wing section with aileron. The verification of the full controlled case is instead carried out against time marching solutions.

The stability effects of the flap are then assessed for a baseline reference airfoil section with the same structural proprieties considered in the previous studies on the flap load alleviation potential [8]. Stability limits are first investigated for an uncontrolled elastic flap in the baseline reference case, and effects of different flap characteristics, as stiffness and mass distribution, are assessed. Then the control algorithms are also applied and stability limits for the same baseline airfoil section are computed, first without any time delay in the control, and then considering also the control time lag.

6.1 Model validation

The model and its implementation are validated, for uncontrolled elastic flap, against Gaunaa's [10] reimplementation of the flutter problem presented by Theodorsen and Garrick [22] for a three degrees of freedom (dof) system. The system consists of a flat rigid plate that translates in the heave direction (y dof) and rotates around the elastic axis (α dof), and of a flat rigid flap that rotates around its hinge point (β dof). The flap is hinged to the aft part of the plate and linear springs constrain the movements in all the three degrees of freedom.

In order to model the flat flap rotation, the deflection mode shape is

specified by a linear function of the chordwise position:

$$u_{fl} = \begin{cases} -\left(\varepsilon - \varepsilon_{fl}^{hp}\right) & \text{if } \varepsilon > \varepsilon_{fl}^{hp}, \\ 0 & \text{otherwise.} \end{cases} \tag{6.1}$$

where, ε is the dimensionless chordwise coordinate and ε_{fl}^{hp} is the coordinate of the point where the flap is hinged. In the validation case $\varepsilon_{fl}^{hp} = 0.6$, which corresponds to a flap lenght of 20% of the chord.

The terms Ims_{fl} (5.4), Ins_{fl} (5.3), and m_{mod} (5.6), evaluated according to the flat flap deformation shape (6.1), return relations that link the structural terms used in the actual model to the inputs that in Theodorsen's formulation specify the structural characteristics of the flap. The modal mass is equal, in fact, to the second moment of area of the flap around its hinge point:

$$m_{mod} = I_{fl,hp} = m_{tot} b_{hc}^2 \, r_\beta^2, \tag{6.2}$$

where r_β^2 refers to the notation used in Theodorsen and Garrick's report [22] and is a dimensionless parameter for the flap second moment of area, normalized with respect to the total airfoil mass. The terms coupling the flap rotation to the airfoil heave and pitch are instead computed as

$$\begin{aligned} Ins_{fl} &= -m_{flap}(\varepsilon_{fl}^{cg} - \varepsilon_{fl}^{hp}) = -m_{tot} X_\beta, \\ Ims_{fl} &= -\frac{1}{b_{hc}^2}\left(I_{fl,hp} - Ins_{fl}\varepsilon_{fl}^{hp} b_{hc}\right). \end{aligned} \tag{6.3}$$

Where, ε_{fl}^{cg} is the position of the centre of gravity of only the flap part, measured from the half chord point; and X_β is the respective dimensionless parameter in Theodorsen's notation. The inputs used in the validation case are specified in Table 6.1.

Parameter	*Symbol*	*Value*
Elastic axis	ε_{ea}	-0.4
Distance c.g.	X_α	0.2
Rad.Gyrat. sq.	r^2	0.25
Density ratio	$m_{tot}/(\pi\rho b_{hc})$	4
Heave-Tor. ratio	ω_y/ω_α	0.2
Flap Hinge pt.	ε_{fl}^{hp}	0.6
Flap Rad.Gyr.	r_{fl}^2	0.0012
Flap c.g.-Hinge dist.	X_β	0
Flap-Tor. ratio	$\omega_{fl}/\omega_\alpha$	$0 \rightarrow 2$

Table 6.1: Dimensionless structural inputs for the validation computations. Flat rigid flap and flat plate airfoil. Comparison with 'three degrees of freedom' flutter case in Theodorsen and Garrick, Figure 8 in [22].

Theodorsen and Garrick's flutter computation refers to a flat plate airfoil, the indicial response function used in the model is hence tuned accordingly. Two approximations for the flat plate response are used, the first one is based on the 'classic' two terms expansion by Jones, while the second one is a three terms approximation by Gaunaa; the numerical values for the respective exponential series coefficients are here reported in Table 2.1, section 2.2.4.

The flutter speed, normalized with respect to the half chord and the torsional frequency, is computed for a range of flap-torsion frequency ratios from zero up to two (Figure 6.1). The results obtained with the two and three terms indicial function approximations are close to each other, but far from the flutter limits reported by Theodorsen and Garrick (black line with stars, in Figure 6.1). The cause, as in the undeformable airfoil part, probably lies in a scarce numerical accuracy in the original computations.

In fact, a reimplementation by Gaunaa[10] of the same method described in Theodorsen's paper yields to flutter speeds (black lines with circles) in very good agreement with the ones found with the actual model. It is also observed that the three terms indicial function approximation (red line) seems slightly more precise than the one based on Jones's two terms coefficients (blue line).

To conclude, the actual model of a suspended airfoil equipped with an elastic not controlled flap is validated by comparing the results with Gaunaa's reimplementation of Theodorsen and Garrick's method. The control part is instead validated afterwards against the results obtained with time marching simulations.

6.2 Baseline reference airfoil section

The structural proprieties of the airfoil section are the same used in the previous investigations on the flap load reduction potential, as described in Buhl et al. [8]. In order to define the structure, the characteristics of both the airfoil section and the flap part should be specified.

The structure of the airfoil section is completely described by seven parameters, already introduced in the undeformable airfoil investigation (section 3.2), their values in the baseline reference case match the ones from Buhl [8], and they are here reported in Table 6.2.

The flap part of the structure is described by the natural frequency associated to the deflection shape, which is five time the torsional one in the baseline reference. But also, due to the generalized coordinates formulation, the mass distribution per unit span (ρ^{2D} in kg/m^2) needs to be specified along all the flap: in the baseline case, it decreases linearly from the hinge point to the trailing edge, as reported in Figure 6.2, the same distribution is adopted in Buhl et al. [8].

Furthermore, the baseline section corresponds to an airfoil with a Risø

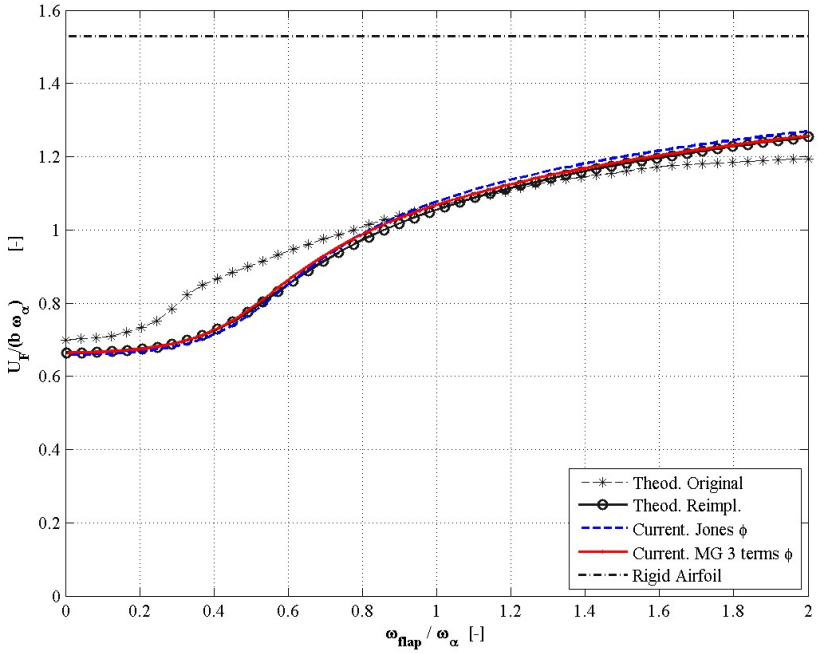

Figure 6.1: Model validation. Reduced flutter speed vs. flap-torsion frequency ratio. Comparison with Theodorsen and Garrick's method [22], original results (black line with stars) and Gaunaa's[10] reimplementation (black line with circles). Flat rigid flap and flat plate airfoil, indicial response function approximations: 2 terms Jones' (dashed blue line) and 3 terms Gaunaa's (full red line).

Parameter	*Symbol*	*Value*	*Unit*
Chord Length	$2b_{hc}$	1	m
Distance Elastic Axis–LE		0.3	m
Distance Center Gravity–LE		0.35	m
Total Mass	m_{tot}	40	kg/m
Moment of Inertia wrt CG	I_{cg}	2	kgm^2
Heave natural frq.	$\omega_y/(2\pi)$	1	Hz
Torsion natural frq.	$\omega_\alpha/(2\pi)$	10	Hz
Flap Mass	m_{flap}	1.62	kg/m
Flap natural frq.	$\omega_{flap}/(2\pi)$	50	Hz

Table 6.2: Structural characteristics and dimensionless parameters for airfoil and flap system corresponding to baseline reference case, as in Buhl et al. [8].

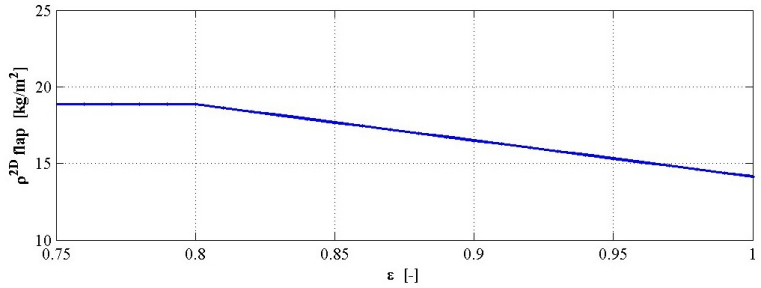

Figure 6.2: Flap unit-span mass distribution, baseline reference. The unit span density decreases linearly from 18.85 kg/m^2 at the hinge point, to 14 kg/m^2 at the trailing edge. Total flap mass 1.62 kg/m.

B1-18 profile. Consequently, as in the latter cases of the undeformable airfoil investigation (section 3.2), the indicial response function is approximated with a three terms exponential series and the corresponding coefficients are the ones computed by Gaunaa [8], and here reported in Table 2.1.

6.3 Uncontrolled flap

A stability analysis is first carried out for the baseline reference airfoil, equipped with elastic flap and without any control applied. The flap is now described by the assigned non linear deflection shape (section 5.1.1), it deforms under the action of aerodynamic and inertial forces, and the control actuator term β_{ctrl} in the flap equation of motion (5.5) is constant and equal to zero, the flap elastic reaction forces are hence null in the undeflected position. Flutter curves are first computed for the baseline case and the sensitivity to the number of integration points used to discretize the deflection shape along the chord is assessed, afterwards, the effects of different flap mass distributions are also investigated.

The flutter limits are computed for a range of different flap stiffness and plotted against flap-torsion frequency ratios (Figure 6.3), the stability limit computed for the undeformable airfoil with the previous model (section 3.2) is also reported (dash-dotted black line).

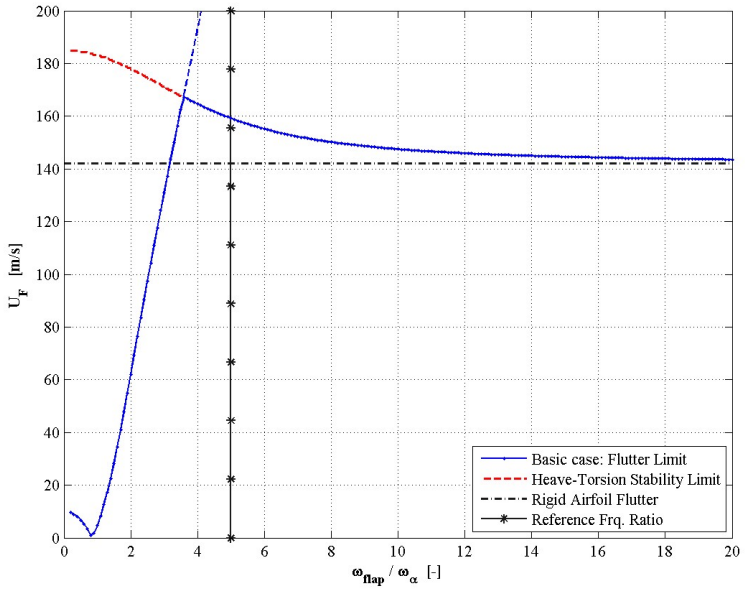

Figure 6.3: Flutter limit vs. flap-torsion frequency ratio. Baseline reference structure. A reasonably stiff flap increases the flutter limit, a flutter speed of 159.2 m/s is reported at the baseline reference frequency ratio, vertical starred black line. The curve converges, for increasing flap stiffness, to the rigid undeformable airfoil flutter velocity 142.2 m/s.

It is observed (Figure 6.3) that, by adding an elastic flap to the airfoil section, the stability limits are modified and they vary depending on the stiffness of the mounted flap. Generally, a twofold effect is obtained, if the flap is sufficiently stiff, the stability limit is increased, compared to the undeformable airfoil; for instance, in the baseline case frequency ratio ($\omega_{flap}/\omega_\alpha = 5$), the flutter speed increases nearly 12 %, from 142.2 m/s in the undeformable airfoil case to 159.2 m/s. The flap stabilizing effect is then reduced as its stiffness increases, and the flutter speed approaches, from above, the undeformable airfoil stability limit of 142.2 m/s, which ideally corresponds to an airfoil equipped with an infinitely stiff flap.

On the other hand, if the flap is too soft, even though the stabilizing effect on the heaving and torsion modes is still present (red dashed line in Figure 6.3), flutter is reported for wind speeds below the rigid airfoil one; in this cases, is the mode related to the flap that causes the system to become unstable.

6.3.1 Sensitivity to number of integration points

The aerodynamic model contains coefficients given by integrals of functions of the deflection shape along the airfoil chord. Since the integration is performed in numerical way and the functions are generally not linear, the results depend on the number of point used to discretize the deflection shape along the chord. It is observed that also the stability limits are sensitive to the number of points used in the numerical integration (Figure 6.4).

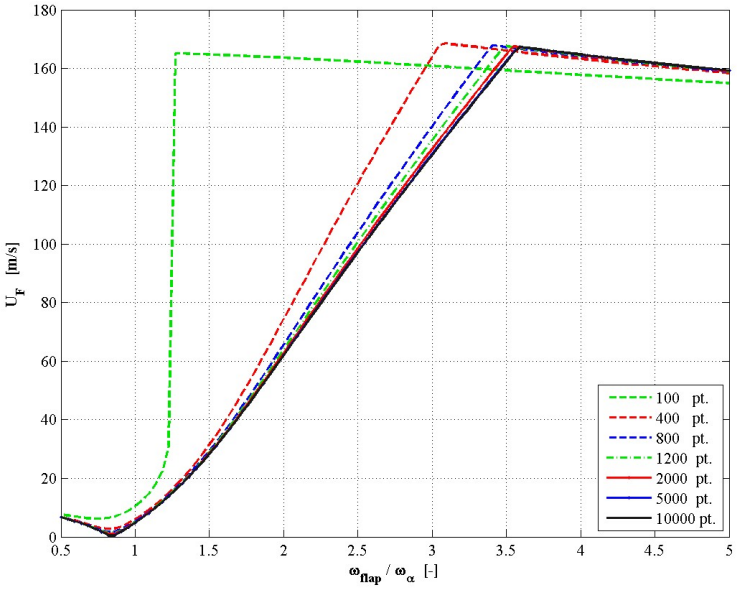

Figure 6.4: Flutter limit vs. flap-torsion frequency ratio. Effects of the number of point used to discretize the deflection shape for numerical integrations. In the actual case, the results obtained with 2000 points is considered sufficiently accurate.

By increasing the number of evaluation points, the resulting stability curves become closer and the difference among them converges to zero. In the actual case, a sufficient accuracy is reached for a number of discretization points equal or greater than 2000. If the number of points is too low, overestimated flutter limit may be reported (dashed green line in Figure 6.4), it is also observed that the curves are more sensitive to the number of integration points in that range of low frequencies ratios where the flap mode is responsible for instability.

6.3.2 Sensitivity to flap mass

In this section the effects of the flap mass distribution on the system stability are investigated. In order to take into account the influence of the flap mass on the airfoil undeformed part of the structure, as, for instance, variations in

the centre of gravity position or in the rotational inertia parameter, a mass distribution shape needs to be assigned not only to the flap but also to the whole airfoil, along the full chord length.

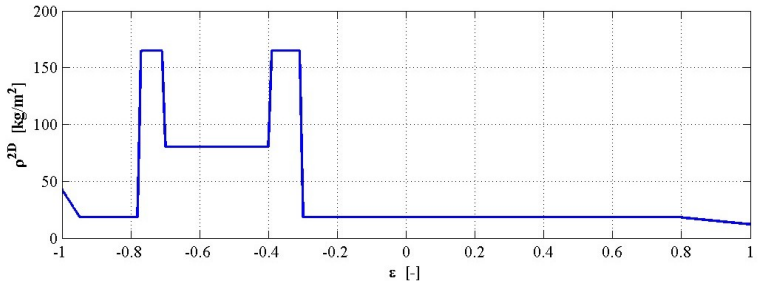

Figure 6.5: *Case 0.* Airfoil unit span mass distribution shape. Compared to the reference case, the same total mass and CG position are maintained, the second moment of area is increased and the flap mass is reduced.

The mass distribution adopted as basic case in this investigations is named as *case 0* and its shape along the chord is reported in Figure 6.2. The total mass of the reference case airfoil (40 kg/m) is maintained, as well as that, the centre of gravity is positioned in the same point and the natural frequencies are unchanged. Table 6.3 reports the structural parameters computed accordingly to the *case 0* mass distribution.

It is observed that the second moment of area is slightly higher than the reference case one (Table 6.2 and 6.3), as a consequence, since the torsional natural frequency is kept constant, also the torsional stiffness is increased. The higher stiffness results in generally increased flutter limits, in fact, the *case 0* undeformable airfoil flutter speed is 150 m/s, nearly 8 m/s higher than in the baseline reference case. As well as that, the reduced flap mass yields to an increased stability of the flap related mode, as it will be better observed in the following paragraphs.

Parameter	*Symbol*	*Value*	*Unit*
Distance Center Gravity–LE		0.35	m
Total Mass	m_{tot}	40	kg/m
Moment of Inertia wrt CG	I_{cg}	2.31	kgm^2
Flap Mass	m_{flap}	1.5	kg/m
Heave natural frq.	$\omega_y/(2\pi)$	1	Hz
Torsion natural frq.	$\omega_\alpha/(2\pi)$	10	Hz
Flap natural frq.	$\omega_{flap}/(2\pi)$	50	Hz

Table 6.3: *Case 0.* Structural characteristics as computed from the assumed mass distribution. In comparison to the baseline reference, the total mass and CG position are unchanged, while the second moment of area is increased and the flap mass is reduced.

Flap centre of gravity

At first, the total mass of the flap part is kept constant, but its distribution is varied, still assuming a linear variation of the 2D mass distribution, from the flap hinge point to the trailing edge. The effects can be represented in analogy to a conventional flat rigid flap as a variation of the dimensionless distance between the flap hinge point and the centre of gravity of the isolated flap (ε_{CG}^{flap}). Table 6.4 describes the investigated cases in terms of unit span density at hinge and trailing edge points and the respective flap centre of gravity positions and modal masses.

	ρ_{hinge}^{2D} $[kg/m^2]$	ρ_{TE}^{2D} $[kg/m^2]$	*Flap Mass* $[kg/m]$	ε_{CG}^{flap} *[–]*	*Modal Mass* $[kg \cdot m]$
Case 0.	18	12	1.5	0.093	$5.4 \cdot 10^{-7}$
Case 1. Aft CG_{flap}	12	18	1.5	0.107	$7.4 \cdot 10^{-7}$
Case 2. Fore CG_{flap}	26.7	3.3	1.5	0.074	$2.7 \cdot 10^{-7}$
Case 3. Aft CG_{flap}	3.3	26.7	1.5	0.126	$1.0 \cdot 10^{-6}$
Case 0. Mass x 2	36	24	3	0.093	$1.1 \cdot 10^{-6}$
Case 0. Mass / 2	9	6	0.75	0.093	$2.7 \cdot 10^{-7}$

Table 6.4: Sensitivity to flap mass variations. Flap mass distribution characteristics for the investigated cases.

As already mentioned, due to the increased torsional stiffness, the flutter curves are generally higher than the reference case one, besides, the lighter flap results in a more stable flap mode, so that the low stability range of frequencies does not extend over a ratio of 1.2 (Figure 6.6). Furthermore, it is also observed that the flap mode is unstable only in a region of low wind speed, for higher speeds it turns stable again (dotted lines in Figure 6.6) until flutter occurs in the heaving or torsion modes.

Concerning the effects of the flap mass distribution, it can be generally concluded that, similarly to the behaviour observed for the undeformed airfoil, the more aft is the flap centre of gravity, the less stable is the mode related to the flap degree of freedom. For instance, *case 3* (dashed red line, Figure 6.6), where more weight is located closer to the trailing edge than to the hinge point, is unstable for frequencies up to nearly six time the torsional one. It is also observed that, since the flap mass is not changed and is relatively light compared to the full airfoil, the effects of the flap mass on the dynamics of the rest of the airfoil are negligible, in fact, for increasing frequency ratios, all the three cases converge to the same rigid airfoil value.

Flap mass scaling

The flap total mass is now varied by scaling the *case 0* distribution by a factor of two and by half; the position of the flap center of gravity is

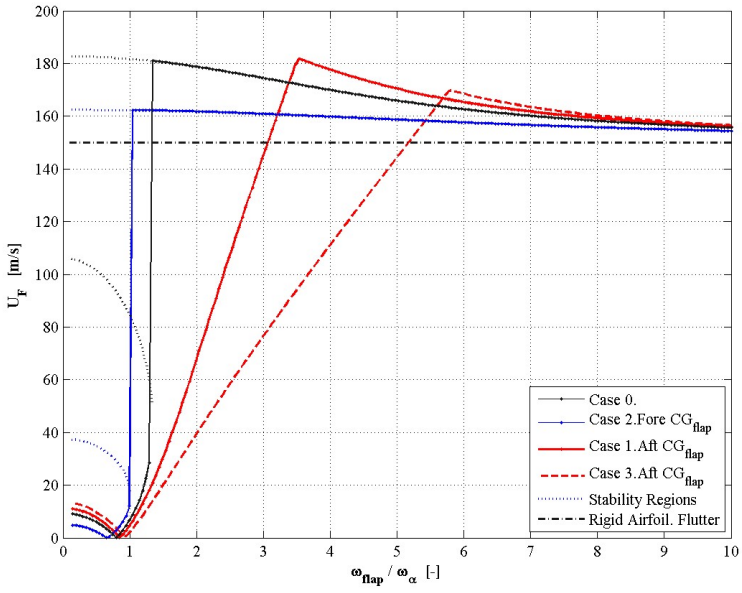

Figure 6.6: Flap mass effects. Constant flap mass, different positions of the flap center of gravity. Mass distributions corresponding to flap with aft center of gravity have a less stable flap mode. All the cases converge to the same rigid airfoil flutter speed (150 m/s).

unchanged and its mass is respectively double and half the previous cases one, Table 6.3.

Concerning the variations induced by the flap mass on the undeformed part of the airfoil structure, two approaches are adopted. The first one (full lines in Figure 6.7) neglects the effects of the flap on the overall mass distribution, so that the undeformed airfoil is described by the same structural parameters as used in *case 0* (total mass m_{tot}, center of gravity position X_α, second moment of area I_{cg}). The second approach, more realistic, takes into account how the flap mass affects the structural proprieties of the rest of the airfoil (dashed lines in Figure 6.7), hence, the airfoil structural parameters are now computed from the modified mass distribution. For instance, if the flap mass is increased, the whole airfoil center of gravity moves aft and the second moment of area increases.

As a consequence, by increasing the flap stiffness, the flutter limits computed using the first approach all converge to the same undeformable airfoil flutter speed (black dash-dotted line), which is the same as in *case 0*, whereas, different limits are obtained if the second approach is adopted (red and blue dashed-dotted lines). A lighter flap, and hence a centre of gravity closer to the leading edge, results in a more stable section: the flutter limit for the rigid case is increased up to 160 m/s. On the contrary when the weight of the flap is doubled, the rigid airfoil flutter speed is reduced to nearly 135 m/s, as effect of the modified mass distribution.

Furthermore, it is observed that the heavier flap (blue lines in Figure 6.7) has a much larger region of instability, which extends up to a frequency ratio of 7.2, and the stability curve translates even lower, if the effects on the airfoil are taken into consideration. The lighter flap has instead a smaller low stability region, but the stabilizing effects on the heave and torsion modes are also slightly reduced; on the other hand, the whole curve arises if the airfoil structural parameters are computed according to the modified mass distribution.

6.3.3 Uncontrolled flap. Summary

To conclude, an elastic flap modifies the aeroelastic stability limits of an airfoil section even if no control is applied. In the considered cases, flutter limit are increased by a reasonably stiff flap, and stability is generally enhanced by a light flap with a centre of gravity close to its hinge point. On the contrary, soft flap, with heavy masses and aft centre of gravity are found to reduce the flutter speed, in some cases even considerably below the undeformable airfoil one.

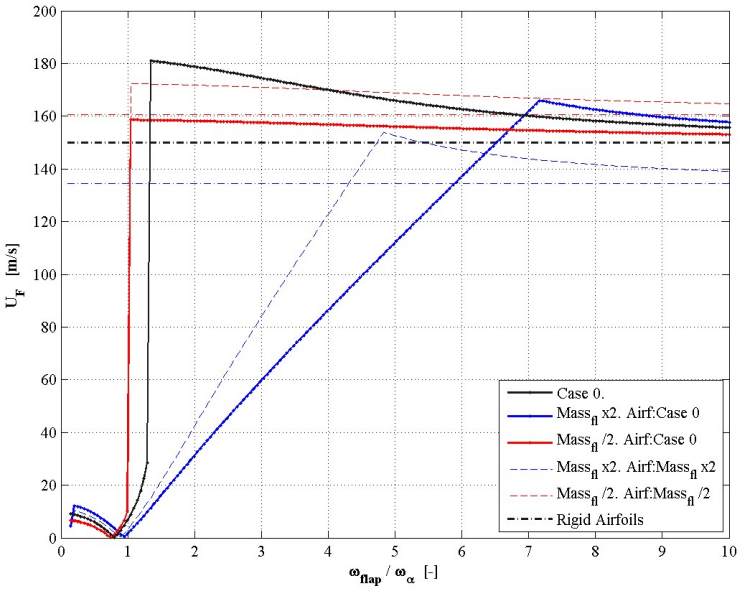

Figure 6.7: Flap mass effects. The flap mass is doubled (blue lines) and scaled to half (red lines), stability limits are computed both neglecting (full lines) and considering (dashed lines) the effects on the airfoil structure.

6.4 Controlled flap

The flow speeds at which aerodynamic instability occur may vary not only due to the flap structure, but also depending on the flap control. This factor of influence is now assessed in the baseline reference case and with the flap controlled according to the algorithms previously described (section 5.3).

The function of the trailing edge flap is to alleviate the loads during normal turbine operation, consequently, the control gain in the present investigations are the ones tuned to give optimal load reduction for a wind speed of 60 m/s. The gain factors are kept constant all over the wind speed range, and no factor scheduling applies; besides, as mentioned in section 5.3, the gain for heave and angle of attack controls are actually the results of a thorough optimization process, carried out in the previous studies [4, 8], whereas, the gain factor for the pressure difference control are assigned with a simple Ziegler-Nichols' tuning.

Stability limits are first computed assuming a null control delay, and afterwards, since the control time lag was found to be a factor of considerable importance in the load alleviation studies, the effects of introducing a control delay are also investigated. The stability tool that includes control and time delay models is validated against the results obtained with time marching simulations.

6.4.1 Control algorithms

The flutter speeds obtained with a controlled flap are plotted (Figure 6.8) versus the flap torsion frequencies ratios for different control algorithm cases, the uncontrolled flap flutter curve is also reported (black full line). The structural characteristics corresponds to the baseline reference case, and so do the control gain parameters, tuned for load alleviation at 60 m/s, a null control time lag is also assumed.

It is observed that the stability curves present similar qualitative trends for all the control algorithms, and they also resembles the uncontrolled case one: in a range of low frequency ratios, the flap related mode provokes flutter and here the critical speed increases almost linearly with the frequency ratio, until instability occur in the heaving or torsion related modes (frequency ratio above 3.5 in the not controlled case).

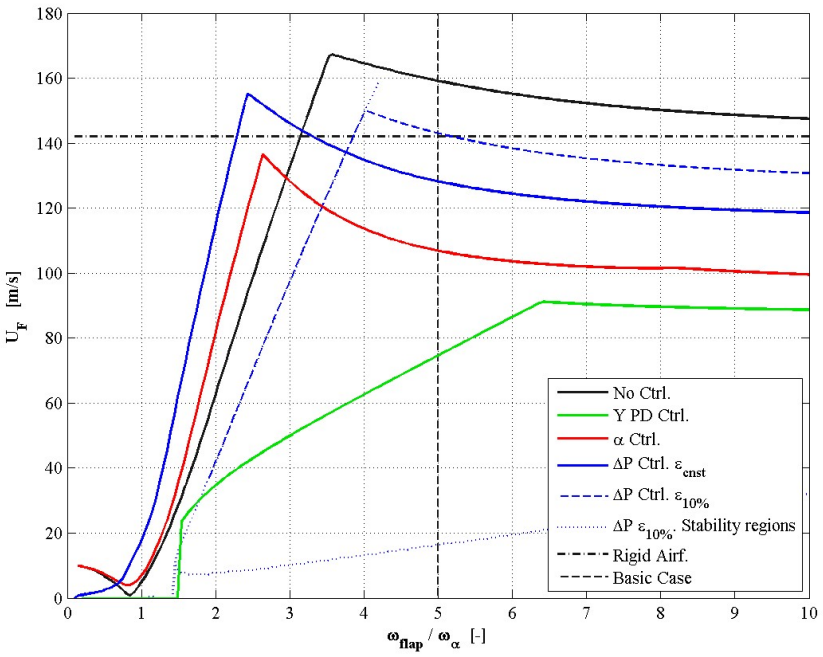

Figure 6.8: Controlled flap stability limits. Flutter speed vs. flap-torsion frequency ratios for the different control algorithms. Null time lag is assumed, the control gain parameters are the baseline reference ones, as well as the structural parameters. The baseline reference frequency ratio is highlighted by the dashed black line.

From a quantitative point of view, instead, all the cases return flutter limits lower than the uncontrolled flap one at the baseline frequency ratio, and different variations are then reported depending on the algorithm used to control the flap. The pressure difference control ΔP seems to be the more stable and, especially in the case of taps located at the 10 % chord,

Type of Control	y, $\dot{y}$	α	$\Delta P\varepsilon_{cnst}$	$\Delta P\varepsilon_{10\%}$	*No Ctrl.*	*No Flap*
Flutter limit [m/s]	74.9	106.8	128.1	143.1	159.3	142.2

Table 6.5: Flutter flow speed at reference condition $\omega_{flap}/\omega_\alpha = 5$. Flap controlled by the presented algorithms, tuned for load alleviation at 60 m/s, null control time lag. The flutter limit computed without control acting on the flap and the limit for the airfoil without flap (undeformed airfoil) are also reported as comparison.

shows only a moderate reduction of the flutter speed (Table 6.5). Lower flutter limits are reported with the angle of attack α control algorithm, but the stability threshold is still above the range of wind speed encountered in normal wind turbine operation. The control based on heave displacement and velocity appears instead as the less stable, and, in the baseline reference case, flutter is reported to occur at a wind speed nearly half the one of the airfoil without flap; the flap control would hence yield to critically low stability limits and the airfoil might encounter flutter even at normal operation flow speeds.

As second note, the slopes of the stability also differ depending on the control algorithm, for instance, stiffer flaps than the reference one, would return slightly lower flutter speeds in almost all the control cases, with the only exception of the heave control, where the stability curve maintain a positive slope up to a frequency ratio of 6.2. A part from that, for low frequency ratios, all the curves show an almost linear trend, and the α and the ΔP (at the ε_{cnst} point) ones have a rather steep slope, so that, for very soft flaps, the flutter limit is increased with respect to the not controlled case. The y controlled section has instead a milder slope and is completely unstable for very soft flaps. The control based on pressure measurements at the 10 % chord is the one that gives the higher stability limit for frequency ratios greater than four, but also, the same control strategy is unstable in a range of low flow speeds, from zero to the dotted line in Figure 6.8.

6.4.2 Control time lag

In the previous studies [8, 4], the control time lag was found to be a major factor affecting the load alleviation potential of a controlled trailing edge flap and it was clearly outlined that, as the time lag increase the achieved load reduction decreases. The influence of the control delay on the stability limits is instead not straightforward. In fact, although it can be concluded that the flow speed at which instability occurs is actually modified by the presence of control delay, the effects are found to be rather dissimilar in each of the considered control strategies (Figure 6.9). Besides that, the results would probably vary depending on how the time lag is implemented in the model.

Figure 6.9 reports, for the different control algorithms, the flutter speeds

computed and plotted as function of the control time lag, expressed as reaction half time $t_{1/2}$. The structural proprieties and the gain parameters are the baseline reference one.

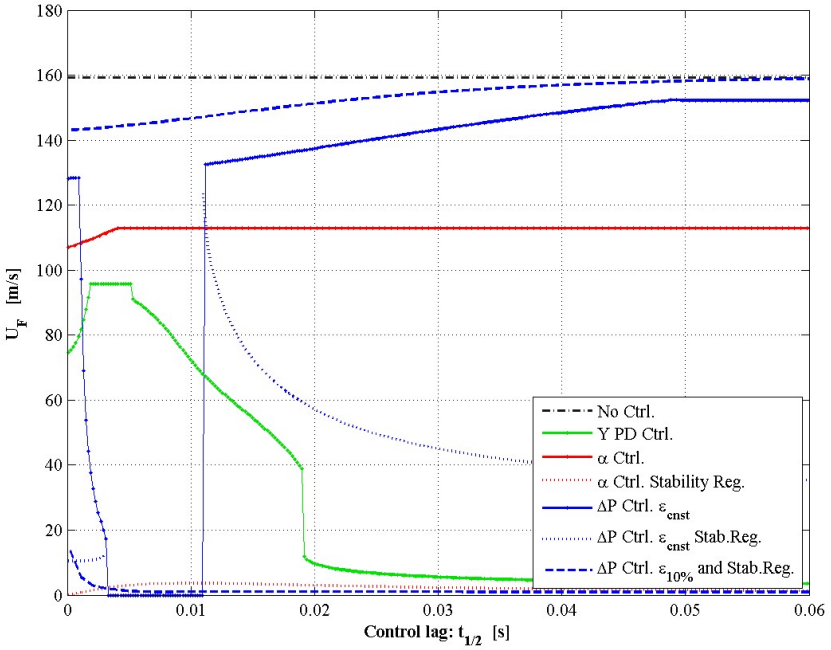

Figure 6.9: Flap stability limits as function of the control time lag, the flutter speed is plotted versus the control reaction half time. The control gains and the structural parameters are at reference condition, $\omega_{flap}/\omega_\alpha = 5$.

The flutter limit for the angle of attack α control increases slightly for small time lags, and then, for $t_{1/2}$ longer than 30 ms, is completely unaffected by further increase of the control lag. The pressure difference control also gives an increase in the stability limit as the time lag arises, but only for the case of pressure tap located at the 10 % chord (dashed blue line in Figure 6.9). Whereas, in the ε_{cnst} pressure control case (full blue line), the flutter speed drops as a small time lag is introduced, and the system is completely unstable in the range of reaction half time from 3 to 11 ms. For longer time delays, stability is again achieved, but only within a range of wind speeds, which become broader as the reaction time increases (from dotted to full blue lines).

The stability curve of the y controlled case presents a peculiar trend. For very small time lags the stability limit is increased up to the reversal speed (green line 'plateau' at 95.5 m/s), but then, if larger control delays are simulated, the flutter speeds reduces and, when the reaction half time of 20 ms is passed, it drops below 10 m/s.

The flutter limits are now computed as function of the flap frequency and for different time lags (0, 5 and 20 ms half reaction times, Figure 6.10). The obtained results are somehow a combination of the curves reported in the two previous plots (Figures 6.8 and 6.9). In fact, in the α and $\Delta P\varepsilon_{10\%}$ cases, the control delay increases the flutter limit, and hence, curves higher than the one obtained without control delay are reported for almost all the investigated frequency ratios (Figure 6.10.b and .d). Instead, the section controlled with pressure taps located at ε_{cnst} (Figure 6.10.c) is unstable in the whole range of ratios for the small time lag case ($t_{1/2} = 0.005\ s$), while for larger time lags a stability region appears for frequency ratios greater than 3. The y-controlled flap still presents a 'plateau' at the reversal speed if the small time lag is considered (red line), while for the larger control delays flutter is reported for wind speeds close to 10 m/s.

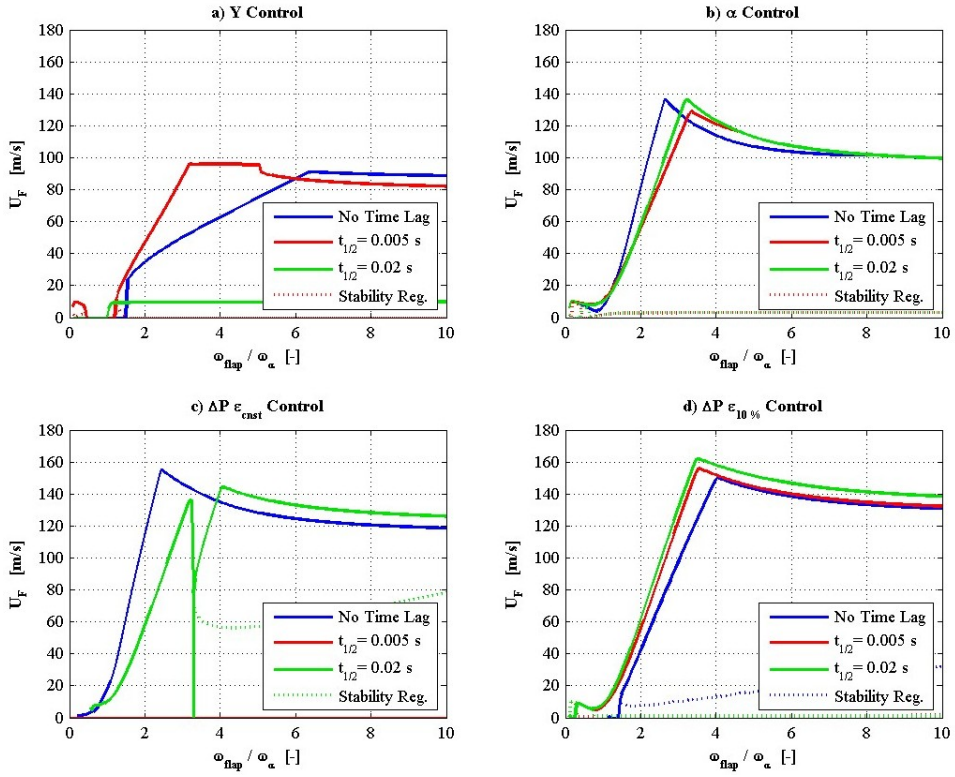

Figure 6.10: Stability limits vs. flap-torsion frequency ratio considering control time lag. Control half time $t_{1/2} = 0.005\ s$ (red lines) and $t_{1/2} = 0.02\ s$ (green lines). The control gains and the other structural parameters are at reference conditions, the stability limits computed without time lag are reported with blue lines.

6.4.3 Controlled flap. Summary

The trailing edge flap modifies the stability limits of the airfoil section, and the effects depend not only on the structural proprieties of the flap, but also on the control algorithm used to actuate it.

Lower flutter limit than the one computed for the uncontrolled elastic flap, are reported with any of the considered control algorithm, all tuned for load alleviation at 60 m/s. The flutter limits are anyway above the flow speeds encountered in normal operation for the controls based on angle of attack or pressure measurements, the latter being the more stable. Whereas, critically low stability limits are reported for the heave control. In this case, the flow speed at which flutter is expected to occur could be raised to a safer range either by intervening on the structure (stiffer and lighter flap, fore centre of gravity, etc.), or by reducing the control gain magnitude.

It is thus observed that all the controlled flap cases show lower flutter limit than the uncontrolled one, which in turn is higher than the undeformable airfoil case. Consequently, whenever the flow speed approaches a critical limit, a convenient way to avoid, or at least postpone, the rise of instability would be to exclude the control of the flap, if this can be done without reducing its stiffness.

The control time delay has an influence on the stability limits, but the effects are different in each of the investigated control algorithms, and a common trend among them is hardly recognizable.

As well as that, the stability limits depend also, in a marked and not trivial fashion, on the structure characteristics; therefore, the results, and perhaps even some of the conclusions, may not apply to different airfoil sections. Each specific case could be anyway investigated separately by applying the presented stability tool.

Chapter 7

Gain tuning for stability enhance

The analysis of the stability limits of an airfoil section with a movable trailing edge highlights how the critical flow speed at which flutter arises depends on the algorithms employed to control the flap, but also on the gain parameters used in the controllers.

It is thus possible to increase the flutter speeds reported in the investigated cases by tuning the gain parameters, the control would in this case aim to enhance stability, and not primarily to alleviate the fatigue loads. From a practical point of view, a wind turbine blade would reach flow speeds above the computed stability limits only in extraordinary conditions, with the exception of the heave control case. Therefore, the gain tuning that appear more convenient would consist in simply turning all the gain parameters to zero whenever not ordinary flow speeds are encountered, due for instance to rotor overspeeding, and raise thus the limits to the uncontrolled flap flutter velocity.

The present chapter investigates anyway the potentiality of a slightly more elaborated gain tuning to control the flap as to raise the stability limits, eventually even above the not controlled case one. The stability tool is hence applied to determine, for increasing flow speeds, the gain parameters range that would maintain the system stable. The method is applied to the baseline reference structure, and the presented algorithms are considered with a null control delay. Results are then verified against the time marching solution.

7.1 Gain tuning method

So far the stability of the system has been assessed by computing the damping of the modes as function of the wind speed, the point then, where at least one of the mode becomes negatively damped sets the stability limit.

In the tuning approach, instead, the wind speed is fixed and the damping of the mode is evaluated as function of the controller gain.

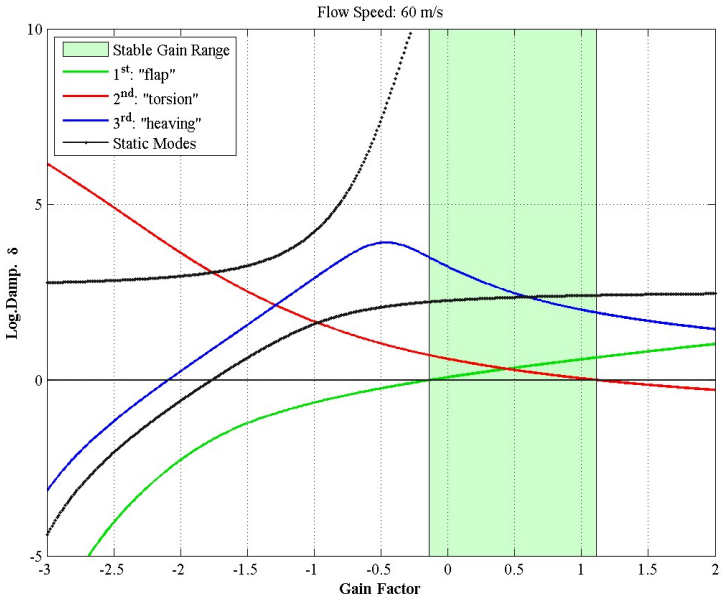

Figure 7.1: Modal damping plotted as function of the controller gain factor. $\Delta P_{\varepsilon,cnst}$ control at 60 m/s, baseline reference condition structure. Stable gain factor range from -0.14 to 1.12, the upper limit match the critical gain found in the time marching tuning.

Figure 7.1 reports, for example, the modal damping plotted versus the gain factor for the $\Delta P\varepsilon_{cnst}$ control, at the same wind speed (60 m/s) that was used in the time marching tuning, Section 5.3.1. The interval on the abscissa where *all* the modes, both dynamic and static, are positively damped indicates in which range the gain factor should be maintained to achieve a stable equilibrium at the investigated wind speed, the same procedure can be then repeated for different wind speed conditions. In the reported example (Figure 7.1), the stable range extends from a gain factor -0.14 to 1.12, and the upper limit corresponds to the critical gain that was found with the time marching tool during the Ziegler-Nichols control tuning.

It may be interesting to consider the sign of the gain parameters from a physical point of view. In this sense, a negative gain factor (positive in the y proportional control) would correspond, for wind speed that are below the control reversal one (95.5 m/s), to a controller that, although eventually stable, operates contrary to the desired way, and *increases* the fluctuations of the lift steady component, yielding thus, most likely, to increased fatigue loads on the structure. The same undesired effect is obtained for wind speed above the reversal limit if the signs of the gain factors are not inverted. Thus,

the gain factors that have been specified in the reference baseline cases correspond to a flap control that 'alleviate loads' only for wind speeds below 95 m/s, for higher speeds, which are anyway not likely to be encountered during normal operation of a wind turbine, the control would actually 'aggravate' the steady lift fluctuations, and thus probably also the fatigue loads.

7.2 Heave control

The gain tuning method is applied to the control algorithm that takes as input measurements of the heave coordinate y and its velocity $\dot{y}$. The control algorithm, tuned for load alleviation at 60 m/s, involves both the proportional and differential terms. For simplicity reasons, though, the gain parameters related to the two terms are, for now, investigated separately: during the gain analysis of the proportional term (Figure 7.2, top), the derivative term gain is set to zero, and the other way around when the differential term is considered (Figure 7.2, bottom). The combined effects of both the gain parameters are later investigated for two selected flow speeds.

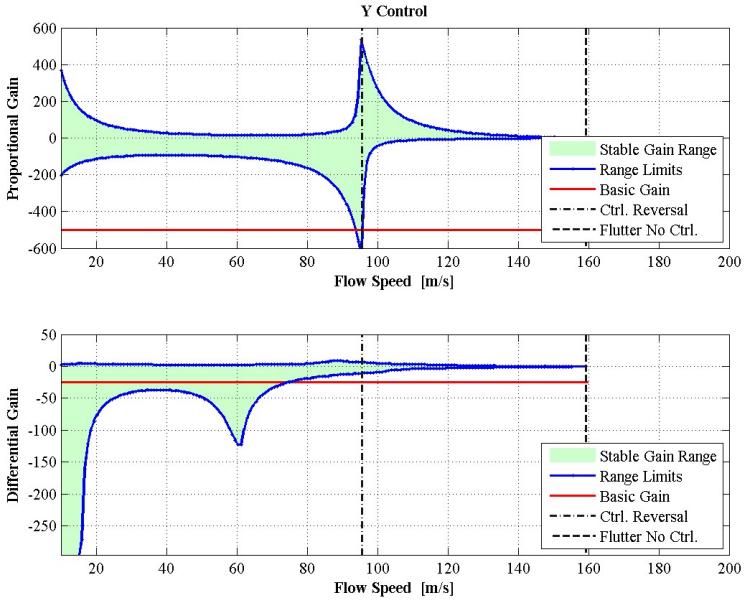

Figure 7.2: Gain tuning for heave control. Top: stability range of *proportional* gain factor vs flow speed, differential gain set to 0. Bottom: stability range for *differential* gain factor, proportional gain set to 0. Reference case structure, null time lag.

The value assigned in the baseline case to the gain for the differential term ($B_y = -25$) exits the stability region at a flow speed (74.9 m/s) that corresponds to the reported flutter velocity (Figure 7.2, bottom), the stability limit seems hence related to the differential gain. It is also observed

that with only proportional control, the gain assigned in the baseline case ($A_y = -500$) would be out of the stable region for nearly every flow speed (Figure 7.2, top).

The stability range of the proportional gain parameter (Figure 7.2, top) extends almost exclusively in the negative semi-plane for wind speeds below the reversal one, whereas a positive gain is required to maintain stability for flow speed above the reversal one. The control algorithm proportional to the heave displacement is the only case, among the investigated ones, where reversal have consequence on the stability of the section. The increase in magnitude of the stable gain values close to the reversal condition, as though close to a vertical asymptote, can be related to the control effectiveness. In fact, at reversal wind speed the lift, and hence the y displacement, are not affected by the flap, the control effectiveness is equal to zero, thus large gain value can be assigned without loss of stability.

The range of stable gains, for both the proportional and differential control, narrows around zero as the wind speed is increased. The flutter limit of the y controlled section can be thus increased by gradually tuning to zero the gain parameters, but, in any case, the flutter velocity of the not controlled section (159.3 m/s) is not exceeded. It is also observed that for a wind speed of 60 m/s the section controlled by only the proportional term is unstable for gain factors less than -100, which is relatively close to the critical value (-70) that was found by Buhl et al. [8] during the time marching study of the same 2D section undergoing a step change in the incoming wind.

The combined effect of the proportional and differential terms is now investigated by fixing the flow speed, the range of proportional gain for which the system is stable is then determined as function of the differential gain (Figure 7.3).

The plot on the left (Figure 7.3) refers to a flow speed slightly above the flutter limit reported for the baseline reference tuning. As previously observed, the flutter limit seems to be related to the differential gain, in fact, the value assigned to the differential gain at the reference case ($B_y = -25$) corresponds to a line outside the stable region, regardless the value of the proportional gain. The flutter limit can be increased only by reducing, in magnitude, the differential gain, and, in this case, the stability limit could be raised up to 90 m/s (Figure 7.3, right plot) with the same proportional gain as in the baseline case ($A_y = -500$). To further increase the flutter limit, also the proportional gain should be reduced.

A part from that, as also observed in previous studies [4, 8], by introducing the differential term, the control is more stable. In fact, by 'increasing'[1] the differential gain, the stability range expands and a larger proportional

[1] In the sense of increasing the magnitude, and maintain the appropriate sign. In this case, since the gain is negative (below reversal speed), the values are actually decreased, they move to the left on the plot abscissa.

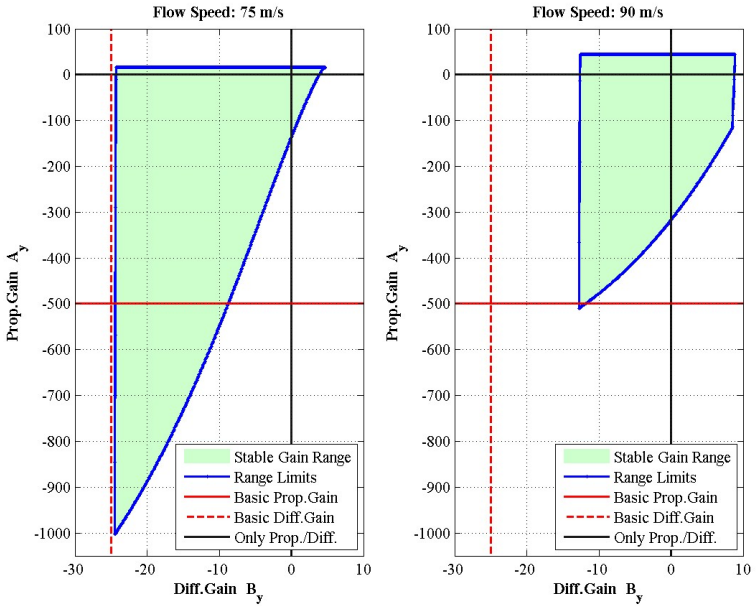

Figure 7.3: Heave control, combined effects of the differential and the proportional gain values. The proportional gain for which the system is stable are computed as function of the differential gain. Fixed flow speed: left, 75 m/s; right, 90 m/s. Reference case structure, null time lag.

gain can be applied.

To conclude, a control based on the heave measurements can not exceed the flutter speed of the uncontrolled case. Furthermore, it is also observed that the differential term is necessary to apply large proportional gains, but, on the other hand, the flutter limit reported in the reference case can be increased only if the differential gain is reduced.

7.3 Angle of attack control

The relation between gain parameter and stability is now investigated for the control algorithm based on angle of attack measurements. The baseline reference case has a control gain equal to one, represented by the horizontal red line in Figure 7.4. The line exits the stable region at a flow speed of nearly 107 m/s, which in fact corresponds to the flutter limit reported in the baseline case (Table 6.5).

In similar way, the line corresponding to a null gain crosses the stability bound at a wind speed of 159.3 m/s, uncontrolled flap flutter velocity, but, contrary to the y case, the stable region now extends even beyond this limit, if negative gains are applied. In fact, by tuning the gain parameter to values inside the stable range (green area in Figure 7.4), stability can be maintained for flow speeds up to 219.2 m/s.

For stable gain parameters, all the modes of the system, both dynamic and static, are positively damped, up to the new limit (219.2 m/s). Hence, the controlled airfoil is stable for flow speeds, not only, above the uncontrolled flap flutter velocity (159.3 m/s), but also, higher than the undeformable airfoil divergence limit (207 m/s); even a static instability phenomenon appears thus to be influenced by the control, and the new stability limit is also confirmed by the implemented time marching tool.

The achieved stability enhance would probably be lower if more realistic conditions, as control time lag or limited flap deflections, were considered. It is anyway possible to conclude that with an active control of the flap and opportune gain parameters, flutter can be suppressed for flow speeds even above the uncontrolled flap flutter velocity.

7.4 Pressure difference controls

The control algorithms based on pressure measurements are now applied. In case of pressure taps located at ε_{cnst} point (Figure 7.5), the baseline gain factor (0.56), results in a flutter speed of 128 m/s, which, in Figure 7.5, corresponds to the point where the red line exits the stable region.

As in the angle of attack case, the stability bound crosses the zero gain horizontal line at the uncontrolled flap flutter speed (159.3 m/s), and for negative gain the stability region extends even further. Thus, with pressure

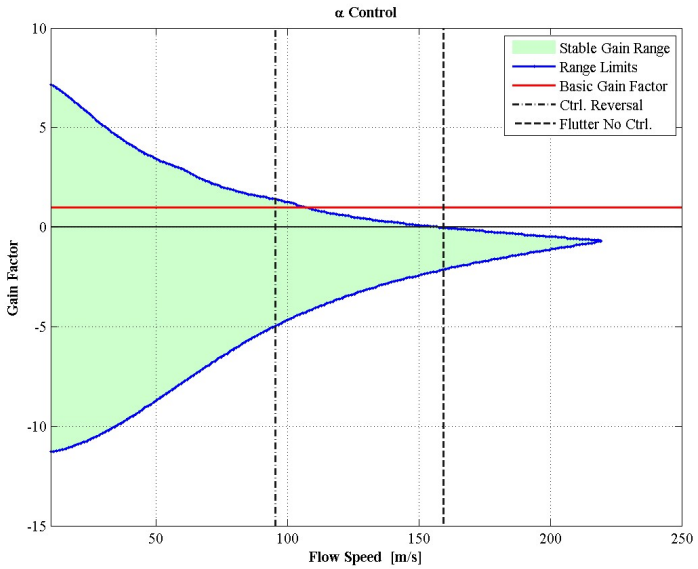

Figure 7.4: Gain tuning for angle of attack control. The red line indicates the gain factor used in the reference case (1.0), the dashed vertical black line marks the flutter limit for the non controlled case. Flutter speed can be extended up to 219.2 m/s, negative gain are required above the uncontrolled flap flutter speed. Reference case structure is considered, null time lag.

difference measurements at ε_{cnst} is possible to control the flap to supress flutter above the uncontrolled case limit; flow speed up to 183 m/s are reported in the investigated case, nearly 15 % higher of what would be obtained by simply excluding the control.

The pressure control based on measurement at the 10% chord appear again as more stable. In fact, by tuning the gain, the stability limit for the investigated case can be extended even above 250 m/s (Figure 7.6). As in the angle of attack case, by actively controlling the flap is possible to rise the stability limit even beyond the divergence speed.

In both the pressure control cases, as well as with the angle of attack control, no particular changes are reported at control reversal speed, furthermore, at a flow speed of 60 m/s the upper limits of the stable gain ranges (1.12 and 0.25) match in both cases the critical gain factors that were found with the time marching tool, during the Ziegler-Nichols' control tuning (Section 5.3.1).

7.5 Gain tuning for stability enhance. Summary

The gain parameters used in the flap control algorithms can alter the stability of the whole section, and the flutter limits reported in the reference

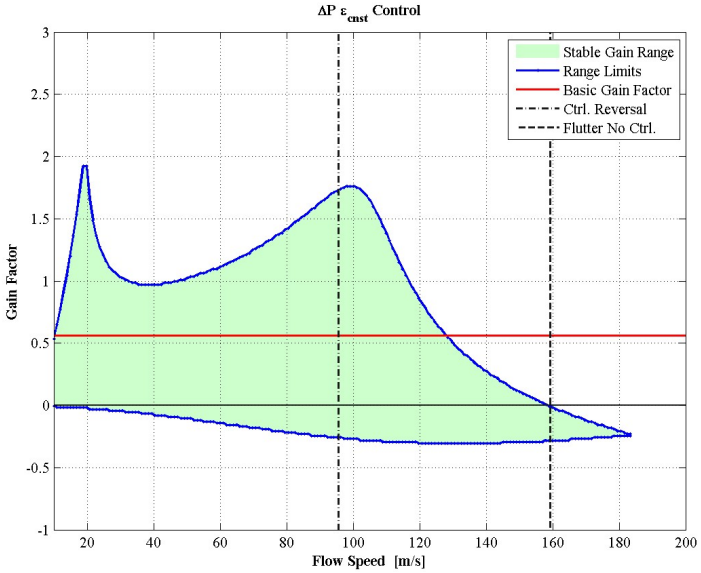

Figure 7.5: Gain tuning for pressure difference control, pressure tap at ε_{cnst}. The red line indicates the gain factor used in the reference case (0.56), the dashed vertical black line marks the flutter limit for the uncontrolled case. Flutter speed can be extended up to 183.4 m/s. Reference case structure is considered, null time lag.

cases can be extended by properly tuning the parameters.

For the heave control, the gain parameters are tuned by simply reducing their magnitude, and the stable region is extended up to the uncontrolled flap flutter velocity, but not further. Whereas, in all the other investigated cases, by actively controlling the flap is possible to suppress flutter and extend the stability limit beyond the uncontrolled flap one, and, with angle of attack or pressure difference (at $\varepsilon_{10\%}$) controls, even beyond the undeformable airfoil divergence velocity.

The stability enhance would be probably lower than the reported ones if more realistic assumptions were included in the model (as for instance, control time lag and limited flap deflection), but still it would be possible to actively control the flap to suppress instabilities above the uncontrolled flap flutter velocity.

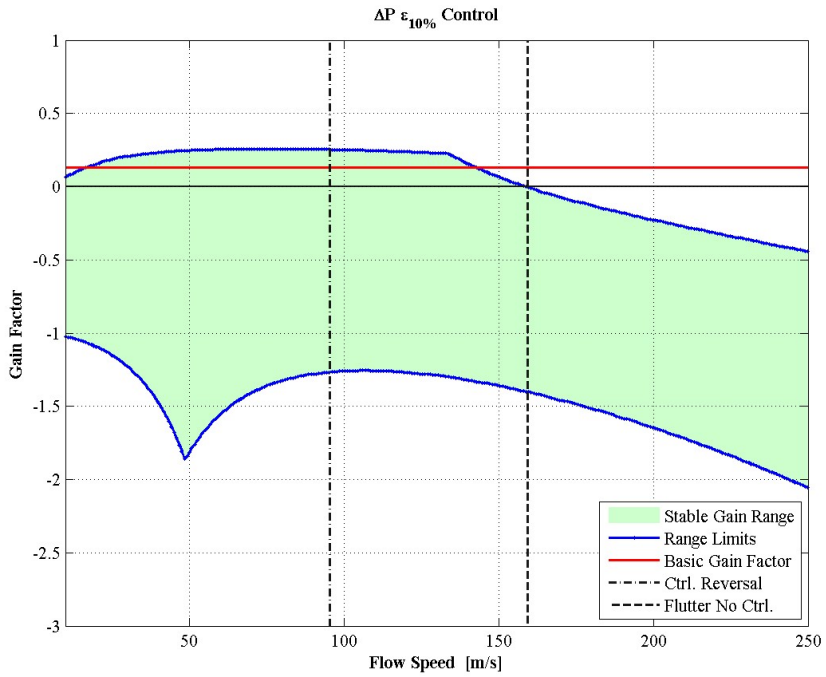

Figure 7.6: Gain tuning for pressure difference control, pressure tap at 10 % chord. The red line indicates the gain factor used in the reference case (0.13), the dashed vertical black line marks the flutter limit for the uncontrolled case. Flutter is suppressed by the control, the section is stable for flow speeds above 250 m/s with gain factors within the specified range. Reference case structure is considered, null time lag.

Chapter 8

Conclusion and future work

A tool to investigate the aeroservoelastic stability of a 2D airfoil section equipped with a trailing edge flap has been implemented and validated. It is thereby observed that the presence of the flap control significantly changes the flow speed at which instabilities such as flutter and divergence occur.

The stability limits are modified by an elastic flap, even without active control: heavy and soft flaps cause the flutter speed to drop, while sufficiently stiff flaps yield to higher flutter limits than in the undeformable trailing edge case. The structure considered in the previous studies on load alleviation potential [4, 8] presents the latter behaviour: the airfoil section equipped with the uncontrolled elastic flap is in fact stable for flow speeds above the undeformable airfoil stability limit.

However, when the control algorithms, which were tuned for fatigue load alleviation at 60 m/s (reference gain parameters), are applied, lower flutter limits are reported and the stability diminution vary considerably depending on the control system. Among the investigated cases, the pressure difference controls show the highest stability limits, and, between them, the control with sensor taps at 10 % chord ($\Delta P_{\varepsilon,10\%}$) appear as more stable. As well as that, the stability limits resulting from the angle of attack control are also not excessively low.

On the contrary, the flap control based on heave measurements returns a flutter speed that, in the reference case, is nearly half the undeformable airfoil one, thus causing the stability limit to drift critically close to flow speeds encountered on wind turbine blades in normal operation. The flutter limit, in this case, could be enhanced either by acting on the structure, for instance by increasing the flap stiffness, or by reducing the control gains.

A marked dependence of the stability limits on the gain parameters is actually observed for all the controls, and, by acting on the gains, stability can be maintained for flow speeds higher than the limits reported in the previous reference cases. In fact, by tuning all gain parameters to zero, the stability limits would be raised to the uncontrolled flap one, and flutter

would be thereby avoided in most of the cases likely to be encountered in practice. Less simple gain scheduling would also allow to suppress flutter at flow speeds even above the stability limit of the uncontrolled flap, at least for the investigated pressure difference and angle of attack controls.

In previous studies [4, 8], control time delay was clearly identified as a limiting factor in the load alleviation potential. In the present stability analysis, instead, the role of the control delay is not straightforward: it actually affects the stability limits, but is not possible to outline a more specific conclusion, since the observed effects vary for each specific case.

As mentioned in the introduction, the present work considered a 2D airfoil section, which undoubtedly is a rough approximation of a full 3D system, hence, the exact stability limits, as would be encountered on a full turbine, can not be predicted by the presented stability tool. Nevertheless, literature reports cases where the results obtained with simple 2D models were then found to be quite representative of more complex 3D phenomena, as, for instance, in Theodorsen and Garrick's stability investigations [22, 21], or in the previous studies concerning the load alleviation potential of the flap control [4].

Therefore, the conclusions outlined with the current stability tool probably hold also for more complex and realistic cases, and the obtained results can be anyway considered as a preliminary investigation and term of comparison for later development of more refined models.

To conclude, a trailing edge control has a significant influence on the stability of the airfoil section, and large and non-trivial variations of the stability limits are reported, depending both on the section structural characteristics and on the control properties. A simulation tool, as presented here, is hence needed to determine, for each specific case, whether or not the deformable trailing edge control will yield to a critical reduction of the flow speed at which instability may occur.

Future work

The idea of applying trailing edge flaps on wind turbine blades is relatively recent, the amount of unresolved issues is hence considerable. Concerning the problems related to stability, the presented aeroservoelastic stability tool should be refined and extended so to handle more complex and realistic cases: 3D structural model should be included, as well as the interaction with other control systems installed on a wind turbine. The aerodynamic model can be also refined to take into account the effects of viscosity in the fluid [2], and 3D finite span geometry.

Different implementations of the control and the time lag models could be also investigated, as well as that, interesting results could be obtained from simulations of the flap actuators that are likely to be employed in full

scale applications, as, for instance, piezoelectric plates, pneumatic trailing edges, rubber membranes.

Finally, significant contributions could come from experimental investigations and validation of the flutter limits predicted by the stability models.

Acknowledgements

Academic acknowledgements

Since this report is the result of the work carried out during my M.Sc. thesis project, I would like to thank my thesis supervisor, Mac, for help and guidance throughout the all project and for being always available for explanations, suggestion and patient corrections.

I also express my gratitude to Thomas, for his essential help in many aspects of the project, and to Peter, for many interesting inputs and 'lively' explanations. And finally, many thanks to everybody in the Aeroelastic design program for being always helpful and ready to answer the more disparate questions.

'Extra-academic' acknowledgements

I will take advantage of the last lines to overstep a bit the academical-scientific sphere and extend my acknowledgements to persons who, in different ways, also had a significant role in this latest years of education.

Thus, in first place, special thanks to my 'two ladies': my little sister Giulia and my mamma Stefania! Among too many reasons, because they always welcomed me with a smile whenever I came back, but especially because they have always forced a smile also every time I was leaving.

A lot of persons are then 'responsible' for the very nice time I had in this two years. I thank all of you, and since listing all the names would require a fourth appendix, I here quote only few (nearly randomly coupled), as representatives of all. Thanks to Kostas and Joachim, Ioanna and Efren, Espe and Ivan, Iorgos and Guille, and many many others. But also thanks to the friends far away, but never distant, to Marione and the great characters from Lega Navale and CVC.

Finally, to conclude from where the thesis started, I would like to extend my gratitude to the persons mentioned in the previous section also to the 'extra-academic' sphere: thanks to the all aeroelastic design group, for the lunch breaks, the cakes, the foosball games; thanks for the hygeeligt atmosphere and the wonderful human environment.

Bibliography

[1] Randall J. Allemang. The modal assurance criterion - twenty years of use and abuse. *Sound and Vibration*, 37(8):14–23, 2003.

[2] P.B. Andersen, M. Gaunaa, C. Bak, and M.H. Hansen. A dynamic stall model for airfoils with deformable trailing edges. *Journal of Physics: Conference Series*, 75(1):012028–1–10, 2007.

[3] P.B. Andersen, L.C. Henriksen, M. Gaunaa, C. Bak, and T. Buhl. Integrating deformable trailing edge geometry in modern mega-watt wind turbine controllers. In *Scientific proceedings. 2008 European Wind Energy Conference and Exhibition, Brussels (BE)*, pages 15–21, 2008.

[4] Peter B. Andersen. Load alleviation on wind turbine blades using variable airfoil geometry (2D and 3D study). Master's thesis, Technical University of Denmark. Department of Mechanical Engineering, 2005.

[5] Peter B. Andersen. Load reduction using pressure difference on airfoil for control of trailing edge flaps. Unpublished. Abstract submitted for European Wind Energy Conference, Marseille, 2009.

[6] Santiago Basualdo. Load alleviation on wind turbines using variable airfoil geometry (a two-dimensional analysis). Master's thesis, Technical University of Denmark. Department of Mechanical Engineering, 2004.

[7] Raymond L. Bisplinshoff, Holt Ashley, and Robert L. Halfman. *Aeroelasticity*. Dover Pubblications, Inc, 1996.

[8] T. Buhl, M. Gaunaa, and C. Bak. Potential load reduction using airfoils with variable trailing edge geometry. *Transactions of the ASME. Journal of Solar Energy Engineering*, 127(4):503–16, 2005.

[9] Mac Gaunaa. Unsteady 2D potential-flow forces on a thin variable geometry airfoil undergoing arbitrary motion. Technical Report 1478, Risø National Laboratory, Roskilde (DK), 2006.

[10] Mac Gaunaa. Investigation of stability issues for an adaptive trailing edge system. Presentation at Wind Turbine Blade Workshop, May 12-14, 2008, Albuquerque, USA., 2008.

[11] M.H. Hansen. Improved modal dynamics of wind turbines to avoid stall-induced vibrations. *Wind Energy*, 6(2):179–195, 2003.

[12] M.H. Hansen. Aeroelastic stability analysis of wind turbines using an eigenvalue approach. *Wind Energy*, 7(2):133–143, 2004.

[13] M.H. Hansen. Stability analysis of three-bladed turbines using an eigenvalue approach. *Collection of ASME Wind Energy Symposium Technical Papers AIAA Aerospace Sciences Meeting and Exhibit*, pages 192–202, 2004.

[14] M.H. Hansen. Aeroelastic instability problems for wind turbines. *Wind Energy*, 10(6):551–577, 2007.

[15] Morten Hartvig Hansen, Mac Gaunaa, and Helge Aagaard Madsen. A beddoes-leishman type dynamic stall model in state-space and indicial formulations. Technical Report 1354, Risø National Laboratory, Roskilde (DK), 2004.

[16] Daniel J. Inman. *Engineering Vibration*. Prentice-Hall, 1994.

[17] R.T. Jones. Unsteady lift of wing of finite aspect ratio. Technical report, National Advisory Committee for Aeronautics (United States Advisory Committee for Aeronautics), 1940.

[18] T.J. Larsen, H.A. Madsen, and K. Thomsen. Active load reduction using individual pitch, based on local blade flow measurements. *Wind Energy*, 8(1):67–80, 2005.

[19] Don W. Lobitz. Aeroelastic stability predictions for a mw-sized blade. *Wind Energy*, 7(3):211–224, 2004.

[20] Katsuhiko Ogata. *Modern Control Engineering*. Prentice-Hall, 1997.

[21] T. Theodorsen. General theory of aerodynamic instability and mechanism of flutter. Technical report, 1935.

[22] T. Theodorsen and I.E. Garrick. Mechanism of flutter, theoretical and experimental investigation of flutter problem (report no. 685). Technical report, National Advisory Committee for Aeronautics (United States Advisory Committee for Aeronautics), 1940.

[23] Jon Juel Thomsen. *Vibrations and Stability*. McGRAW-HILL, 1997.

[24] Niels Troldborg. Computational study of the Risø B1-18 airfoil equipped with actively controlled trailing edge flaps. Master's thesis, Technical University of Denmark. Department of Mechanical Engineering, 2004.

[25] T. von Karman and W.R. Sears. Airfoil theory for non-uniform motion. *Journal of Aeronautical Sciences*, 5(10):379–390, 1938.

[26] Thomas A. Zeiler. Results of theodorsen and garrick revisited. *Journal of Aircraft*, 37(5):918–920, 2000.

List of Figures

List of Tables

Appendix A

Undeformable airfoil. Linearized equations

The aeroelastic system is described by a set of non linear differential equations, but the eigenvalue approach that is used to investigate the stability of the system requires indeed a linear formulation of the system equations. The expressions given in the main body of the text (chapter 2) are hence linearized by using a Taylor's series expansion with respect to a specified equilibrium steady state, which is characterized by the steady state pitch angle $\alpha_{0,sts}$. The equations presented here to determine the linearized aerodynamic forces are retrieved from Hansen's work [15], where a thorough description of the approach is also given.

The set of differential equations that describes the aeroelastic system, chapter 2, in the general non linear formulation is:

$$m_{tot}\ddot{x} - S_\alpha \sin(\alpha)\ddot{\alpha} + c_x\dot{x} + k_x x = D_{static} + \Delta D_{ind}, \quad \text{(A.1)}$$

$$m_{tot}\ddot{y} - S_\alpha \cos(\alpha)\ddot{\alpha} + c_y\dot{y} + k_y y = L_{nc} + L_{circ}, \quad \text{(A.2)}$$

$$-S_\alpha \sin(\alpha)\ddot{x} - S_\alpha \cos(\alpha)\ddot{y} + I_{ea}\ddot{\alpha} + c_\alpha\dot{\alpha} + k_\alpha\alpha = M_{nc} + M_{circ}. \quad \text{(A.3)}$$

Where, the left hand sides of the equations represent the inertial, damping and elastic forces acting on the structure, and the right hand sides the aerodynamic forces.

A.1 Structural equations

The structural equations are linearised by simply substituting the steady state pitch-torsion angle $\alpha_{0,sts}$ in the trigonometric terms, so that the equa-

tions left hand sides read

$$m_{tot}\ddot{x} - S_\alpha \sin(\alpha_{0,sts})\ddot{\alpha} + c_x\dot{x} + k_x x, \tag{A.4}$$

$$m_{tot}\ddot{y} - S_\alpha \cos(\alpha_{0,sts})\ddot{\alpha} + c_y\dot{y} + k_y y, \tag{A.5}$$

$$- S_\alpha \sin(\alpha_{0,sts})\ddot{x} - S_\alpha \cos(\alpha_{0,sts})\ddot{y} + I_{ea}\ddot{\alpha} + c_\alpha\dot{\alpha} + k_\alpha\alpha. \tag{A.6}$$

A.2 Aerodynamic equations

A.2.1 Effective angle of attack

The expressions for the aerodynamic equations, in order to take into account the effect of the vorticity shed into the wake, contain terms that depend on the effective angle of attack α_{eff}. The expression for α_{eff} is also linearised by applying a Taylor expansion, and the linear term α^1_{eff}, as in Hansen [15], is:

$$\alpha^1_{eff} = \alpha^1_{3/4}\varphi_0 + \sum_{i=1}^{n_{lag}} z^1_i \tag{A.7}$$

All the terms identified by the superscript ^{1} are first order (linear) terms from Taylor's series expansion; hence, z^1_i are the linear terms of the wake time lag variables and they result from the respective first order differential equations; in linearised form

$$\begin{aligned}\dot{z}^1_i = & -\frac{U_0}{b_{hc}} b_i \cdot z^1_i \; + \; \frac{A_i}{U_0}\alpha_{0,sts}\cdot\ddot{x} \\ & - \frac{U_0}{b_{hc}} b_i A_i \cdot \alpha \; - \; \frac{U_0}{b_{hc}} b_i A_i \cdot \alpha_{0,sts} \\ & - \frac{1}{b_{hc}} b_i A_i \cdot \dot{y} \; + \; (0.5 - \varepsilon_{ea}) b_i A_i \cdot \dot{\alpha}.\end{aligned} \tag{A.8}$$

A_i and b_i indicate the coefficients of the exponential terms series that approximates the indicial response function (section 2.2.4), the numerical values assigned in the investigated cases are reported in Table 2.1, on page 20.

In equation (A.7), $\alpha^1_{3/4}$ is the linear term of the Taylor's expansion for the equivalent quasi-steady angle of attack at 3/4 chord:

$$\alpha^1_{3/4} = \alpha - \alpha_{0,sts} - \frac{1}{U_0}\dot{y} + \frac{(0.5 - \varepsilon_{ea}) b_{hc}}{U_0}\dot{\alpha}, \tag{A.9}$$

and $\alpha_{0,sts}$ is the pitch angle that characterizes the steady state with respect to which the system is linearised.

The term φ_0 instead refers to the approximated indicial response func-

tion, at time zero, it can be hence computed as

$$\varphi_0 = 1 - \sum_{i=1}^{n_{lag}} A_i. \tag{A.10}$$

A.2.2 Lift force

The state, with respect to which the system is linearised, is a static state, that is to say that all the derivatives terms are null; the linearised expression for the non circulatory contribution to the lift force is hence simply

$$L_{nc} = \pi\rho b_{hc}^2 U_0 \cdot \dot{\alpha} - \pi\rho b_{hc}^2 \cdot \ddot{y} - \pi\rho b_{hc}^3 \varepsilon_{ea} \cdot \ddot{\alpha}. \tag{A.11}$$

The circulatory part of the lift is instead split in two contributions: a first one from the steady state ($L^{lin}_{C_L^0}$) and a second one from the linear terms of the Taylor's expansion ($L^{lin}_{\alpha^1_{eff}}$),

$$L^{lin}_{circ} = \; L^{lin}_{C_L^0} + L^{lin}_{\alpha^1_{eff}}. \tag{A.12}$$

The two terms are then computed as:

$$\begin{aligned} L^{lin}_{C_L^0} \;=\; & + (2\pi)\rho b_{hc}(\alpha_{0,sts} - \alpha_{lift,0})U_0^2 \\ & + (2\pi)\rho b_{hc}(\alpha_{0,sts} - \alpha_{lift,0})(-2U_0) \cdot \dot{x}, \end{aligned} \tag{A.13}$$

$$\begin{aligned} L^{lin}_{\alpha^1_{eff}} \;=\; & + (2\pi)\rho b_{hc} U_0^2 \cdot \sum_{i=1}^{n_{lag}} z_i^1 \;+\; (2\pi)\rho b_{hc} U_0^2 \varphi_0 \cdot \alpha \\ & - (2\pi)\rho b_{hc} U_0 \varphi_0 \cdot \dot{y} \quad + \; (2\pi)\rho b_{hc}^2 U_0 \varphi_0 (0.5 - \varepsilon_{ea}) \cdot \dot{\alpha} \\ & - (2\pi)\rho b_{hc} U_0^2 \varphi_0 \alpha_{0,sts}. \end{aligned} \tag{A.14}$$

Where 2π is the linear static lift coefficient $\partial C_l / \partial \alpha$.

A.2.3 Drag Force

The linearised expression for the drag force is also split in a steady state contribution and an induced one:

$$D^{lin}_{aed} = D^{lin}_{stat} + D^{lin}_{ind}. \tag{A.15}$$

The steady state part is computed as

$$D^{lin}_{stat} = \; + \rho b_{hc} C d_0 U_0^2 \;+\; \rho b_{hc} C d_0 (-2U_0) \cdot \dot{x}, \tag{A.16}$$

where Cd_0 is the static drag coefficient, retrieved from the airfoil drag curve at the steady state angle of attack $\alpha_{0,sts}$.

The linearised induced drag is then computed as

$$\begin{aligned} D_{ind}^{lin} = &+(Cd_{lin} - Cl_0)\rho b_{hc} U_0^2 \varphi_0 \ \alpha - (Cd_{lin} - Cl_0)\rho b_{hc} U_0^2 \varphi_0 \ \alpha_{0,sts} \\ &- (Cd_{lin} - Cl_0)\rho b_{hc} U_0 \varphi_0 \ \dot{y} + (Cd_{lin} - Cl_0)\rho b_{hc} U_0 \varphi_0 (0.5 - \varepsilon_{ea}) b_{hc} \ \dot{\alpha} \\ &+ (Cd_{lin} - Cl_0)\rho b_{hc} U_0^2 \sum_{i=1}^{n_{lag}} z_i^1, \end{aligned} \tag{A.17}$$

where Cd_{lin} is the slope of the curve for the static drag coefficient at an angle of attack equal to the steady state one, and Cl_0 is the static lift coefficient evaluated at the same angle of attack:

$$Cd_{lin} - Cl_0 = \left.\frac{\partial Cd}{\partial \alpha}\right|_{\alpha_{0,sts}} - 2\pi(\alpha_{0,sts} - \alpha_{lift,0}). \tag{A.18}$$

A.2.4 Pitching moment

As also noted in the lift case, since the velocity and acceleration components are all null in the steady state used to linearised, the non circulatory contributions to the pitching moment in linearised form is simply

$$\begin{aligned} M_{nc}^{lin} = \ &- \pi\rho b_{hc}^3 U_0 (0.5 - \varepsilon_{ea}) \cdot \dot{\alpha} \ - \ \pi\rho b_{hc}^4 (1/8 + \varepsilon_{ea}) \cdot \ddot{\alpha} \\ &- \pi\rho b_{hc}^3 \varepsilon_{ea} \cdot \ddot{y} \ + \ \pi\rho b_{hc}^3 \varepsilon_{ea} \alpha_{0,sts} \cdot \ddot{x}. \end{aligned} \tag{A.19}$$

The circulatory pitching moment, then, receives a contribution from the steady state that only depends on the static moment of the airfoil at the steady state angle and on the airfoil velocity component in the stream wise direction $\dot{x}$:

$$M_{circ,Cm_0}^{lin} = \ 2\rho b_{hc}^2 Cm_0 U_0^2 \ - \ 4\rho b_{hc}^2 Cm_0 U_0 \cdot \dot{x}. \tag{A.20}$$

A third pitching moment contribution also arises from the lift and drag forces whenever the hinge point of the section is not located at the quarter chord point. This contribution is thus given by the product of the linearised circulatory lift (A.12) and drag (A.15) times, respectively, the cos and sin of the steady state torsion angle, times the distance of the actual elastic axis from the hinge point:

$$M_{circ,forces}^{lin} = L_{circ}^{lin} \cos(\alpha_{0,sts})(0.5 + \varepsilon_{ea}) b_{hc} + D_{aed}^{lin} \sin(\alpha_{0,sts})(0.5 + \varepsilon_{ea}) b_{hc}. \tag{A.21}$$

All the expressions are now available in a linearised form, which results in a set of equations that describes the aeroelastic system in the proximity of the steady state used in the process. This linearised system of equations can be then analysed using an eigenvalue approach and thus determine if that steady state represents a point of stable equilibrium for the specified

system.

Appendix B

Undeformable airfoil. Sensitivity to structural parameters

The undeformable airfoil section is employed in a rapid sensitivity analysis of the flutter limits to the values used to define the structural proprieties of the airfoil section. The characteristics of the structure are defined by means of dimensionless parameters, as presented in section 3.1, and their effects are investigated by changing only one parameter per time, while all the others are kept constant.

The airfoil section used as reference in the following investigation is the one defined in the validation case, section 3.1, and the set of structural proprieties are specified in Table 3.1, at page 28.

The flutter speeds are computed over a range of heave-torsion frequency ratios, and plotted as dimensionless reduced speed, normalized with respect to the torsional natural frequency and the half chord length.

The sensitivity of the computed flutter limits is investigated by applying variations to: the position of the section centre of gravity and elastic axis, the mass density ratio, the radius of gyration and the structural damping. The obtained plots are reported and discussed in the following paragraphs.

Elastic axis and centre of gravity position Figure B.1 shows how the flutter speed versus the frequency ratio varies with the elastic axis position ε_{ea} and with the distance between elastic axis and centre of gravity x_α. By moving the elastic axis aft (from full to dashed and dotted lines), the flutter speed is decreased, at least until the frequency ratio reaches up to the 'dip point'. Increasing the dimensionless moment of static unbalance (from blue to red lines) also reduces the flutter limit, in the range of low frequencies ratios. Furthermore, the static unbalance parameter also modifies the trend of the whole stability curves. Besides, it may be observed that in the range

of low frequency ratios, similar flutter limits are reported for sections with the centre of gravity positioned in the same point $\varepsilon_{cg} = \varepsilon_{ea} + x_\alpha$. In fact, as also observed in Theodorsen's empirical equation, Eq.(2.36) in section 2.4, the position of the elastic axes is not affecting the flutter speed in the low frequency range.

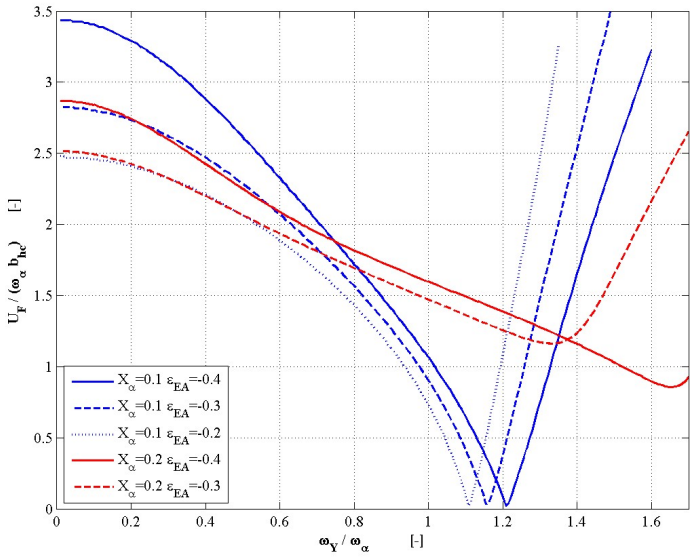

Figure B.1: Flutter limit for the test section. Sensitivity to elastic axis position ε_{ea} and its distance from the centre of gravity x_α. For low frequencies ratios the flutter limit only depend on the centre of gravity position $\varepsilon_{cg} = \varepsilon_{ea} + x_\alpha$.

Mass density ratio The density ratio parameter (Fig.B.2) affects the flutter limit in the same way for the whole investigated range of frequency ratios: the heavier the section is, the higher the flutter speed, as far as the frequencies are kept constant, and hence also the stiffness values are increased. The same trend is confirmed in Theodorsen and Garrick [22].

Radius of gyration The effects of the dimensionless radius of gyration parameter are shown in Figure B.3. Lower radii of gyration (increased rotational inertia) yield to lower flutter limit in the low frequencies range. The effect is reversed after a point that in the investigated cases corresponds to a frequency ratio between 0.8 and 1.

Structural damping The structure is now modified by adding linear damping (Fig.B.4). The same structural damping is applied to all the three degrees of freedom, values of logarithmic damping δ of half point percent

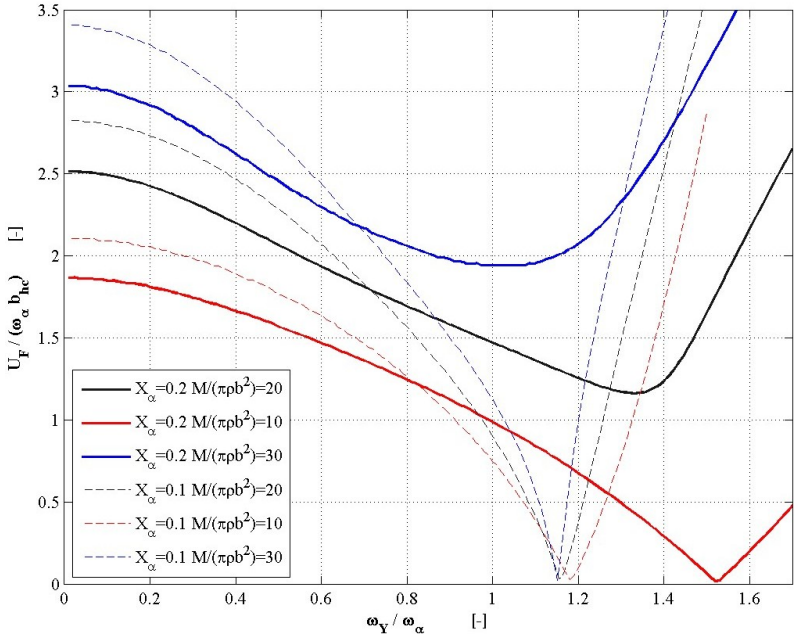

Figure B.2: Flutter limit for the test section. Sensitivity to the mass ratio. Heavier section have higher flutter speed (if constant natural frequencies are assumed).

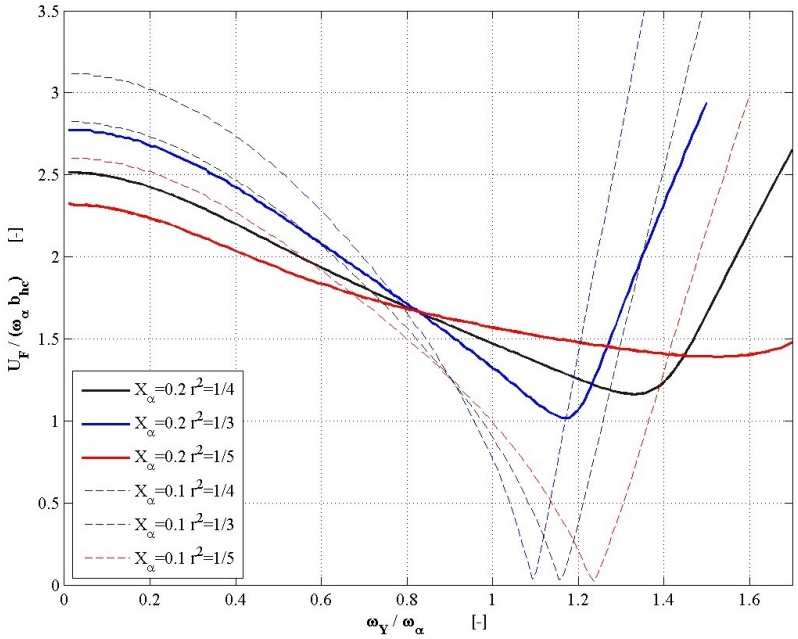

Figure B.3: Flutter limit for the test section. Sensitivity to the dimensionless radius of gyration. Higher second moments of area (small r parameters) reduce the flutter limits, in the low frequency range and for fixed natural frequencies.

and nearly two points percent are investigated. The damping ratios ξ are 0.08% and 0.3%, according to the relation [16]:

$$\delta = \frac{2\pi\xi}{\sqrt{1-\xi^2}} \approx 2\pi\xi \tag{B.1}$$

The structural damping is scarcely affecting the flutter speed at low frequencies, but at higher ratios, it considerably increases the flutter limits and it smooths the curves dip (Fig.B.4).

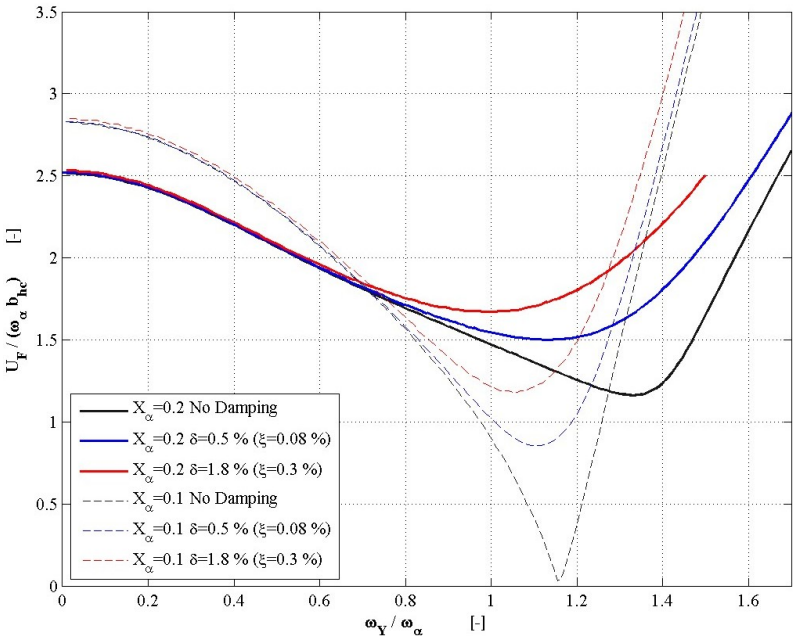

Figure B.4: Flutter limit for the test section. Sensitivity to structural damping. Damping is scarcely affecting at low frequency ratios, while it increases the flutter speed for higher frequencies.

The range of small frequency ratios is the one of more of interest for wind turbine applications, a summary of how the structural parameters may affect the stability limits for this range of frequency is hence presented in the main body of the text, section 3.1.2.

Appendix C

Pressure measurement point

The aim of the control algorithms is to reduce fluctuations in the lift force. In the ΔP control case the objective is sought by limiting the variation of the pressure difference between the two sides of the airfoil in a specified point along the chord; it is thus implicitly assumed that the pressure difference in the sensor point can be directly related to the total lift force.

This relation is here analysed by assuming steady state conditions, the equations for the pressure difference (5.14) and the lift force (5.8) hence reduce to linear terms in α and β, and in dimensionless form, they result in the static coefficients,

$$C_L = \frac{Lift}{0.5\rho U_0^2(2b_{hc})} = 2\pi \cdot \alpha - H_{dydx} \cdot \beta, \tag{C.1}$$

$$C_P = \frac{\Delta P}{0.5\rho U_0^2} = -4\frac{\varepsilon - 1}{\sqrt{1-\varepsilon^2}} \cdot \alpha + 2\pi \left(\partial f_{dydx} - \frac{H_{dydx}}{\sqrt{1-\varepsilon^2}} \right) \cdot \beta, \tag{C.2}$$

where the H_{dydx} and ∂f_{dydx} terms are integral functions of the deflection shape, as defined in [9].

Both the coefficients are functions of the angle of attack α and the flap deflection β, but the pressure coefficient C_P is also depending on the position along the chord. The dependence is given not only by the explicit terms in ε, but also by the integral term ∂f_{dydx}, which is a non linear function of ε. The distribution of the pressure coefficient along the chord is plotted in Figure C.1 for few pitch and flap angles.

The criterion used in the choice of the pressure tap position is based on the ratio between the steady lift and pressure coefficients, along the chord (Figure C.2). The steady ratio is generally a function of α, β and ε, thereby, for measurements points located in an arbitrary position along the chord, in order to relate pressure difference sensed in steady conditions to the steady lift force, the value of the two state variables α and β should be also known.

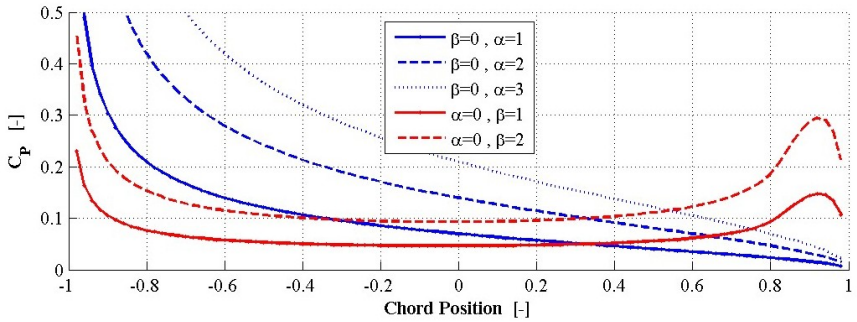

Figure C.1: Pressure Coefficient distribution along the airfoil chord, chordwise dimensionless coordinates ε. Steady conditions, arbitrary values of α and β. The pressure coefficient is higher close to the leading edge.

In fact, the steady condition ratio is:

$$\frac{C_L}{C_P} = \frac{2\pi \cdot \alpha - H_{dydx} \cdot \beta}{-4\frac{\varepsilon - 1}{\sqrt{1-\varepsilon^2}} \cdot \alpha + 2\pi \left(\partial f_{dydx} - \frac{H_{dydx}}{\sqrt{1-\varepsilon^2}} \right) \cdot \beta}. \tag{C.3}$$

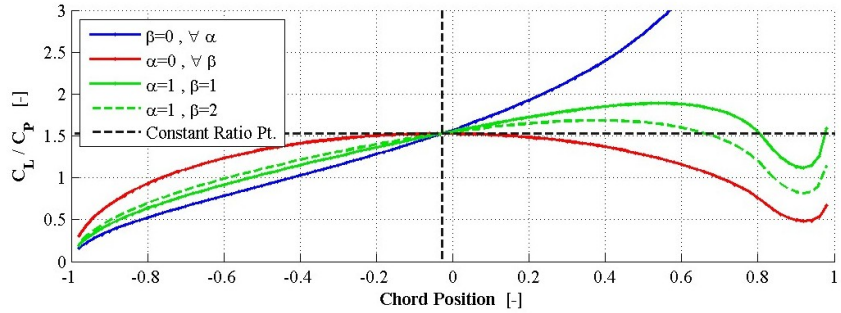

Figure C.2: Lift-pressure coefficients ratio along the airfoil chord, dimensionless chordwise coordinates ε. Steady conditions, arbitrary values of α and β. The ratio varies along the chord and generally depending also from α and β. At the point ε_{cnst} (black dashed line) the ratio C_L/C_P is constant $\forall\ \alpha, \beta$.

On the other hand, from the distribution of the C_L/C_P ratio along the chord (Figure C.2), it can be observed that exists one point ε_{cnst} where the lift-pressure ratio is constant for any angle of attack and flap deflection. This proprerty allows, in steady condition, to directly compute the lift force from measurement of pressure difference in the specific point ε_{cnst}, without requiring the angle of attack α or the flap deflection β.

The point ε_{cnst} is found by imposing the condition that the lift-pressure ratio should not be function of α and β, in the specific point, hence, the partial derivatives of the C_L/C_P function (C.3), with respect to α and β,

are zero for any arbitrary value of the angle variables, resulting in the system:

$$\begin{cases} \frac{\partial C_L/C_P}{\partial \alpha} & = 0 \\ \frac{\partial C_L/C_P}{\partial \beta} & = 0 \end{cases} \quad \text{for } \forall\ \alpha, \beta \tag{C.4}$$

The solution of the system is found in the points of dimensionless coordinates

$$\varepsilon = \pm \frac{\partial f_{dydx}}{\sqrt{\partial f_{dydx}^2 + H_{dydx^2}}}, \tag{C.5}$$

where the integral term ∂f_{dydx} is still a function of the chord wise coordinate ε. Due to the complexity of this function, equation (C.5) is then solved by graphical means at the intersection between the line $\upsilon = 0$ and the line the line $\upsilon_{(\varepsilon)}$:

$$\varepsilon_{cnst} = \varepsilon^* \quad : \quad \upsilon_{(\varepsilon^*)} = \pm \frac{\partial f_{dydx,(\varepsilon^*)}}{\sqrt{\partial f_{dydx,(\varepsilon^*)}^2 + H_{dydx^2}}} - \varepsilon^* = 0. \tag{C.6}$$

The result corresponds to the coordinate ε_{cnst} where, in steady conditions, the ratio between the pressure and lift coefficients C_L/C_P is constant for every angle of attack and flap deflection, the same point ε_{cnst} is used in one of the pressure difference control algorithm. With computations based on the actual deflection shape, the point is located at coordinate

$$\varepsilon_{cnst} = -0.0289. \tag{C.7}$$